Measurement of Heavy Quarkonia Production Cross Section at CMS

Thesis by

Shuang GUO

School of Physics, Peking University

Peking University

Beijing, China

Thesis submitted for the degree of

doctor of philosophy

Prof. Dr. Sijin QIAN (Supervisor)

Prof. Dr. Lorenzo FOA

Dr. Fabrizio PALLA

May 2011

Measurement of Heavy Quarkonia Production Cross Section in CMS

Shuang GUO **(Particle and Nuclear Physics)**

Supervised by **Prof. Dr. Sijin QIAN (Supervisor)**

Prof. Dr. Lorenzo FOA

Dr. Fabrizio PALLA

Abstract

One of the questions puzzled physicists is the contradiction between the Color Octet Mechanism (COM) theory and the experimental results on the cross section and the polarization of heavy flavor quarkonium in hadron collider. Before LHC, there are several measurements provided by other experiments, e.g. CDF and D0 on Tevatron. After LHC's switching on, re-measurement in CMS may help to understand this puzzle, since it can collect larger event samples of heavy flavor quarkonium at higher transverse momentum and with wider coverage of pseudo-rapidity than other detectors before, even in the early stage of LHC's run. As well as the J/ψ has a much larger production cross section than most of the reaction channels, this measurement is one of the earliest physics results in CMS.

In this thesis, the measurements on one of the heavy quarkonium, i.e. J/ψ , in dimuon decay channel are described. Totally, $314nb^{-1}$ data collected by CMS until September 2010 will be used in this analysis. After skimming, selection and trigger, known peaks of mother particles are good enough to fit in the dimuon invariant mass spectrum. Reconstruction efficiencies of single muon and J/ψ will be calculated in both Monte-Carlo and data-driven methodology (the so-called "Tag and Probe" method). Comparing to Υ meson, there are two components in J/ψ collected in CMS, the prompt J/ψ produced "directly" and nonprompt one decayed from B-hadrons, which could be separated by fitting the J/ψ's life time.

The cross section is measured as a function of transverse momentum (p_T) and rapidity (y) and be compared with the the Monte Carlo generator output (theoretical prediction). Finally, based on the $314nb^{-1}$ data in CMS, the J/ψ cross section in the region of $4.5 < p_T^{J/\psi} < 30\ GeV/c$ and $|y^{J/\psi}| < 2.4$ is measured to be,

$$251.4 \pm 3.6(stat) \pm 29.9(syst) \pm 27.6(lumi)\ \text{nb}$$

in which the systematic uncertainties are estimated to be 12% approximately.

Keywords: CMS, heavy flavor quarkonia, J/ψ, hadronic-production cross section, NRQCD

Acknowledgments

First of all, I would like to say thanks to my motherland. She gave me the opportunities to study in Peking University and to do scientific research abroad under a joint PhD student program organized and supported by the China Scholarship Council. I was educated and trained well in these five years and will give my contribution back to the whole society and all Chinese population from now on.

Secondly, I would like to give the thankfulness to my supervisor, Prof. QIAN Sijin, one of the most hard working professors in high energy physics field in China. It is him, who picked me at the graduate student admission interview. Without him, I could not become one of the Peking University students. He is a very good teacher to lead students to the advanced knowledge and modern methods of study, e.g. the one of self-directed, what to do and what not to do, etc. Prof. Qian is also very nice to students everyday life. One thing touched me the deepest is that he always generous on students' time spent with parents and family. In addition, Prof. Qian helped me getting the opportunity to study at INFN-Pisa (Istituto Nazionale di Fisica Nucleare, Sezione di Pisa) in Italy, where I finished most content of this thesis.

I sincerely express my thanks and gratitudes to Prof. Lorenzo Foa and Prof. Fabrizio Palla, who invited me to and supervised me at INFN Pisa. Prof. Foa is a very patient director, especially the invitation letter that brought him so much botheration. Prof. Palla is a quite erudite master on high energy physics. What really surprised me was that Prof. Palla pointed out one bug in my code as soon as he saw the plots in my presentation, even without seeing my code itself. He gave me a lot of fruitful suggestions on the $J/\psi \to \mu^+\mu^-$ analysis, including some crucial ones. Furthermore, I am grateful for all colleagues and friends at INFN, Luca Martini, Francesco Fiori, Jacopo Bernardini, Aafke Kraan, Franco Ligabue, who cooperated and helped a lot on my study and staying in Pisa. I learned so much from them and enjoyed the productive working experience with them.

All professors and students in High Energy Physics group of Peking University are seriously appreciated for their teaching, guiding, helping to and sharing with me. Prof. MAO Yajun, Prof. BAN Yong and associated Prof. WANG Siguang are good teachers in their lessons. They instructed me into the world of particle physics. At the weekly group meeting, they also provided many useful and professional suggestions and ideas on all my work. ZHU Bo, LIU Kun, HU Zhen and WANG Xianjing are wonderful colleagues and friends in both work and life. They offered me so much happiness in the past five years and will be the most important fellows in rest of my life.

Many thanks to professors at B-physics group and Quarkonia Task Force meeting at CERN. Every presentation and report I gave at the biweekly meetings was commented attentively, which encouraged me to going forward.

Last but the most important, I thank my fiancee and parents for their support behind me. Without them, nothing could be achieved, not only the PhD degree but also everything in my life. Thank you! I love you!

Contents

Chapter 1

Introduction

J/ψ meson, the first heavy quarkonia discovered in the world[1][2][3], has been studied extensively since a few decays ago. The similar studies are also held to other heavy flavor quarkonium, e.g. $\psi(2S)$[4][5], Υ[6], etc.

Theoretical physicists developed Quantum Chromo-Dynamics (QCD)[7][8][9] and built the Color-Singlet model (CSM)[10][11] to describe the production mechanism of heavy quarkonium in hadron collider. Unfortunately, both of the Collider Detector at Fermilab (CDF, one detector on Tevatron accelerator at FNAL) and D0 (another detector on Tevatron) experiments gave a quite different result on measurement of the J/ψ production cross section that cannot match the CSM prediction[12][13]. Thereafter, another theoretical model, namely Color-Octet Mechanism (COM), was proposed[10][14]. Based on the cross section result from CDF, eight matrix elements were fitted and the COM result matches the heavy flavor quarkonium cross section in hadron collision. However, the prediction of COM does not agree with the measurement on the polarization of J/ψ or Υ in either of CDF or D0[15]. The tentative explanation by physicists is that the systematic and the statistic errors are so large that the real polarization could be merged into these uncertainties, also the QCD theory is not so "relativistic" in CDF's measurement transverse momentum ($p_T < 20$ GeV$/c$) region since the statistic is poor beyond this extent. Later, the k_T factorization correction[10], that considering the kinematical activity of partons in proton, gives the similar tendency to the experimental polarization results. Recently, another explanation is proposed that the polarization could be measured in not only the helicity (HX) frame but also in the Collins-Soper (CS) frame. In the CS frame, various experimental results, including CDF and other experiments, are somehow reasonable and matched well with each other [16].

Facing the poor statistic and the low p_T in CDF, Compact Muon Solenoid (CMS) could provide sufficient heavy quarkonium events and the polarization could be analyzed in the p_T range as high as 100 GeV/c, thanks to the high luminosity at Large Hadron Collider (LHC) and the wide rapidity range in CMS.

CMS has a powerful muon detection system, which may produce narrow resonances in dimuon invariant mass spectrum. This is the reason why we choose dimuon channel in J/ψ decay. Although there could be over 1000 tracks detected by CMS tracker system, muon chambers are able to isolate muons with good quality.

In this thesis, the LHC and CMS will be introduced in Chapter 2.

In Chapter 3, some theoretical models on particle physics, i.e. QCD and heavy flavor quarkonia production will be discussed. Generally, Standard Model (SM) is the basic theory in particle physics, in which the strong and the electroweak interactions are combined. The QCD describes the strong interactions of colored quarks and gluons based on the SU(3) symmetry group. Different models, e.g. CEM, CSM and COM are used to explain the production mechanism of heavy flavor quarkonia production in hadron collision.

Chapter 4 explains the basic muon reconstruction in CMS detector by fitting the track collected in tracking sub-detector and muon chambers. J/ψ events are reconstructed by combining two muons together and passing a vertex filter. Muons are selected carefully to avoid low efficiency at certain region, where the statistical uncertainty is large. Trigger menu is updated from time to time. For this study, the $HLT\_DoubleMu0$ is loaded and the background is suppressed strongly.

In Chapter 5, geometrical acceptance and efficiency are calculated from Monte

Carlo simulation and experimental data. These two values may bias due to the unknown kinematical distribution at generator level and both of them are reweighted to the data spectrum. This variation is considered to be a systematic uncertainty.

The J/ψ yields in each bin is counted by fitting the invariant mass peak in Chapter 6. Also the lifetime of the mother particle is measured to separate the prompt and nonprompt components.

Cross sections are calculated in Chapter 7, for the inclusive J/ψ, prompt J/ψ and non-prompt J/ψ.

Chapter 8 gives a brief conclusion and forecast on further study about the cross section and polarization of heavy quarkonia.

Chapter 2

LHC and CMS

Large Hadron Collider (LHC), located at the European Organization for Nuclear Research (CERN) near the city of Geneva bestrides the border of France and Switzerland about $100m$ underground, has started to operate since November 2009, which brought a new world of physics under its high energy. At LHC, there are six experiments, i.e. ALICE, ATLAS, CMS, LHCb, TOTEM and LHCf. The CMS (Compact Muon Solenoid) and ATLAS are two general-purpose detectors, built for a wide range of physics research, including Higgs boson, superasymmetry (SUSY), extra dimensions, b-physics, etc. Although it is similar from structure to physics goals of these two detectors, they have their own special characters. For instance, the Electromagnetic Calorimeter (ECAL) system in CMS has finer energy resolution while the advantage of ATLAS tracking system leads to a better performance in muon reconstruction. The detailed information of LHC and CMS are in sections below.

2.1 CERN

CERN, established in 1954, is the largest particle physics laboratory in world. In history, CERN is the acronym of, in French, for *Conceil Europeén pour la Recherche Nucléaire* (European Council for Nuclear Research). Later, this name changed to be a new one, but CERN remained to be the abbreviation of the new name by following the suggestion of Heisenberg. At the beginning of CERN's establishment, scientists were working on atomic nucleus, while soon after that people went to the study of interaction between particles, which is beyond the nuclear physics. In decades, some important physical discoveries, e.g. the neutral currents, W and Z bosons, CP-violation, were reported from CERN, including Nobel Prizes. Up to now, CERN is a leading laboratory in particle physics and LHC is providing us a most power tool on new physics.

CERN is also the place where World Wide Web (WWW) was born. Tim Berners-Lee invented the WWW in 1990 [17].

2.2 LHC

LHC, the newly built accelerator at CERN, was approved by CERN Council in December 1994 to study the known and unkown particles and to test the validity of theory. It was switched on at 10 : 28, 10 September 2008, and the first beam was injected in, with the scrap signal and beam halo catched by CMS and ATLAS. Unfortunately, on 19 September 2008 during this commissioning run, not long from its switching on, LHC suffered one equipment mishap and had to be shut down for 14 months to fix all the damaged components. On 20 November 2009, the beams were successfully re-circulated and soon the energy rose from 450 GeV to 3.5 TeV, a half of its design energy. The geographical schema of LHC and experimental detectors are shown in Fig. 2.1.

2.2.1 Beam at LHC

The LHC beam is formed by proton bunches, it could be heavy ions in some periods. In LHC technical design report[19], lead ion is the heaviest stable to be used. A batch of about 10^{11} protons are compacted into a bunch. Bunches are pushed intermittently (25 ns between two bunches approximately) into the accelerator located in the tunnel of the former LEP (*Large Electron Positron collider*).

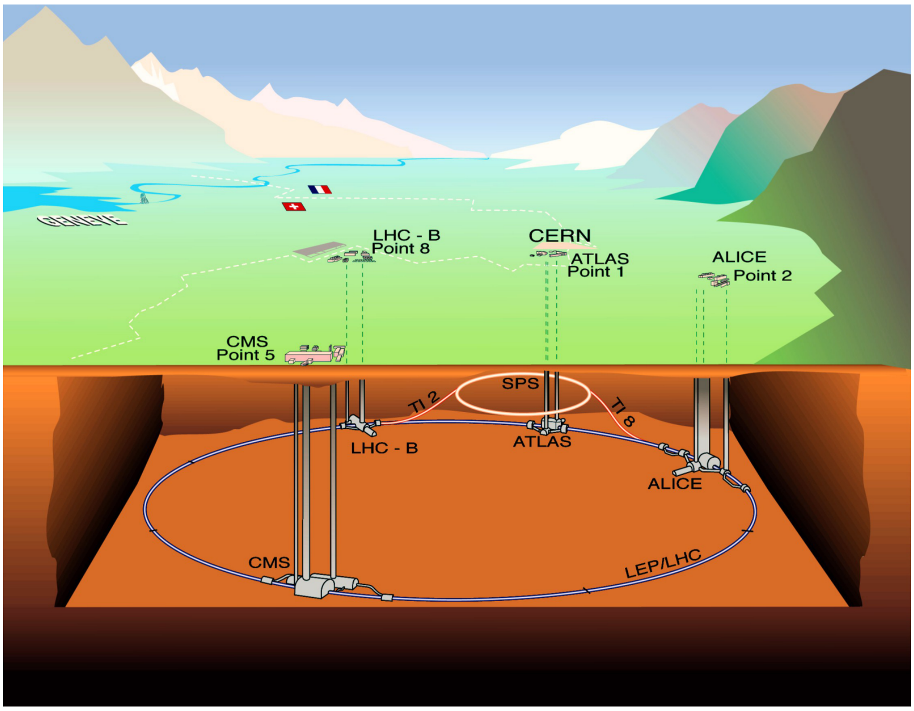

Figure 2.1: LHC and experimental detectors[18].

In contrast to electrons, protons and lead ions, heavy particles with specific charge less than 1 ($\gamma = q/m < 1$), are not so difficult to accelerate, since their synchrotron radiation proportional to γ^4 is much weaker than electrons when running around the storage ring. Rather than antiproton, protons could accumulate higher intensity.

Beams are injected into pre-accelerators and then led to two 27 km-long LHC storage rings parallel but in opposite direction separately. Firstly, the source produces protons from duoplasmatron and then the protons are accelerated to the energy of 50 MeV in a linear accelerator (LINAC). Secondly, protons are injected into Proton Synchrotron Booster (PSB) and the energy is boosted to 1.4 GeV. Thirdly, Proton Synchrotron (PS) accelerates the protons to 25 GeV. Later, in the Super Proton Synchrotron (SPS) the proton's energy approaches 450 GeV. Finally, proton goes into LHC ring. After acceleration, the energy reaches the designed level and beams will be guided to some certain points of LHC and will collide with each other in detectors[18], shown in Fig. 2.2.

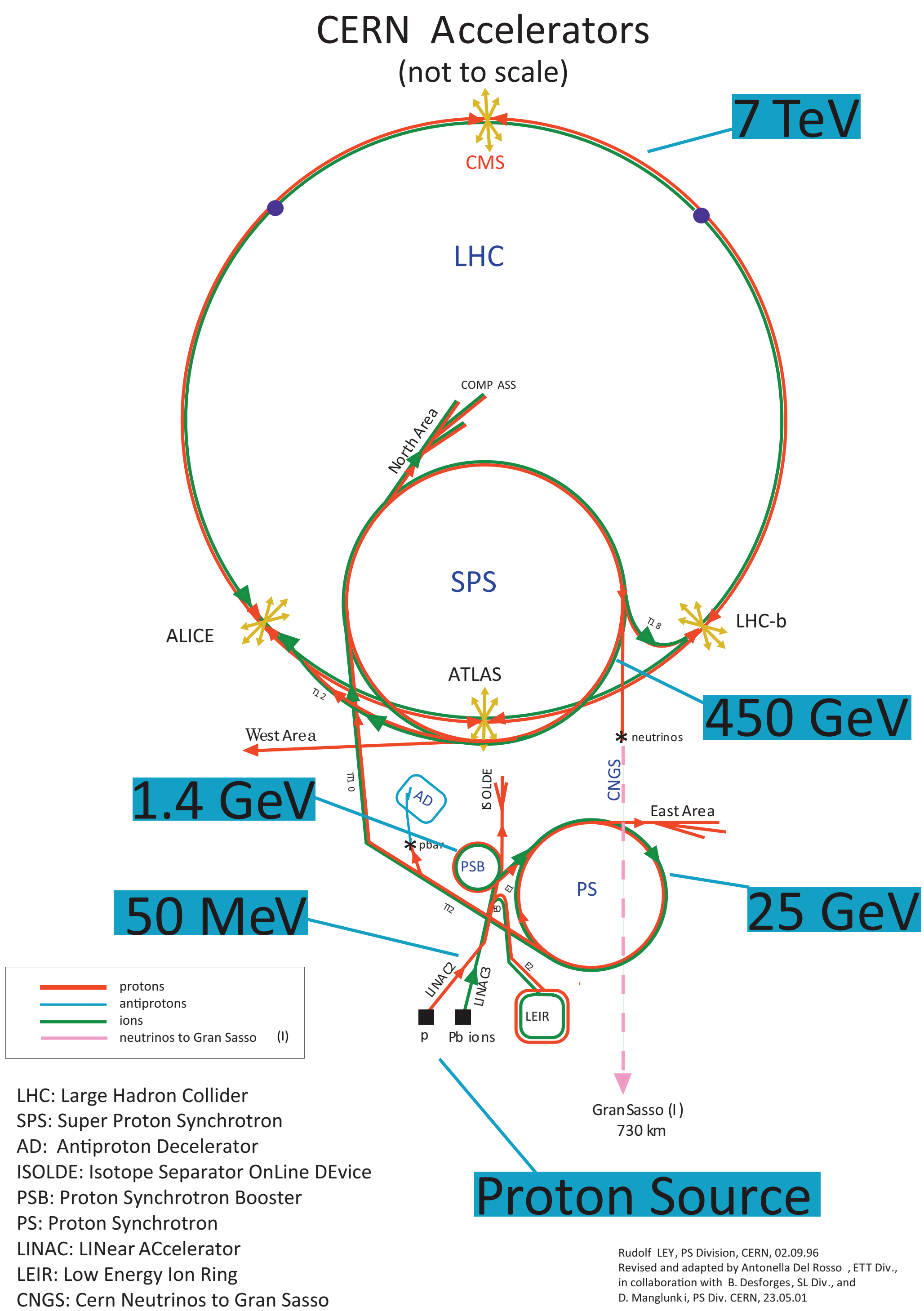

Figure 2.2: LHC schematic diagram[18].

LHC consists of over 8,000 superconductive magnets. Inside the magnets, there are two beam pipes. All magnets are linked to each other to form the 27-kilometer-ring. Along the ring, there are 2 accelerating points to boost beam protons to 7 TeV. Such high energy indicates that these particles run inside beam pipes at speed close to light. 7 TeV is the highest energy produced by human beings in history. In design, the beam energy is 7 TeV but the energy is increasing step by step at the beginning of the LHC's run. In the first three years (2010-2012), the energy will be kept at 3.5 TeV. To maintain the particle's states and detector working condition, the whole LHC and detectors are running under extreme environment, e.g. inside beam pipe is ultrahigh vacuum, all the materials are working under strong radiations, superconducting magnets need the operational temperature as low as $-271\,^{\circ}$C cooled by liquid helium, etc.

There are totally 1232 15m-long dipole-magnets for bending the beam and 392 quadrupole magnets with 5-7m length for focussing the beam. Along the 27-kilometer machine, Two beams collide at only 4 interaction points, where 4 large detectors are built, i.e. ALICE, ATLAS, CMS and LHCb, in which ATLAS and CMS are multi-purpose detectors. They have the similar structures, e.g. 4π solid angle covered around the interaction point with precise tracking and calorimeter systems, and have overlapped physics topic ranges. Profiting from higher level of combined confidence and more importantly cross check on the finding at one another, there could be different solutions to one issue. In addition, other detectors focus on, heavy ions physics in ALICE and b-physics in LHCb.

2.2.2 Luminosity at LHC

Besides the energy of LHC, its luminosity breaks another world record of accelerator technology, that it will reach as high as $L = 10^{34} cm^{-2} s^{-1}$ for proton and $L = 10^{27} cm^{-2} s^{-1}$ for lead ions.

In high energy physics experiment, the integrated luminosity ($\int Ldt$) is also a frequently used quantity. To CMS, it indicts the number of reactions in detector which could be measured in a given time. Practically, there is one luminosity group specially working this.

The task of luminosity group is to provide real-time monitoring of the LHC online luminosity and to determine overall offline normalization for physics analysis[20]. In CMS, the forward hadronic calorimeter (HF) helps to measure the current baseline online luminosity. The HF covers the range of pseudorapidity (η) from 3 to 5 ($3 < |\eta| < 5$) at the endcap of CMS[22]. Besides, Pixel Luminosity Telescope (PLT), by using a set of purpose-built particle tracking telescopes on single-crystal diamond pixel detectors that will be installed at later stage of CMS, will count the number of particles interacting with some detector planes, according to which the relative bunch-by-bunch luminosity can be measured. In addition, a TOTEM detector will be installed experiment at the far forward regions of CMS during its shut down period and this detector will measure the whole p-p collision cross section. This is another way for LHC luminosity determination.

Also, luminosity group provides the instantaneous and integrated luminosity for offline analysis. Fig. 2.3 shows the recent results on luminosity monitoring.

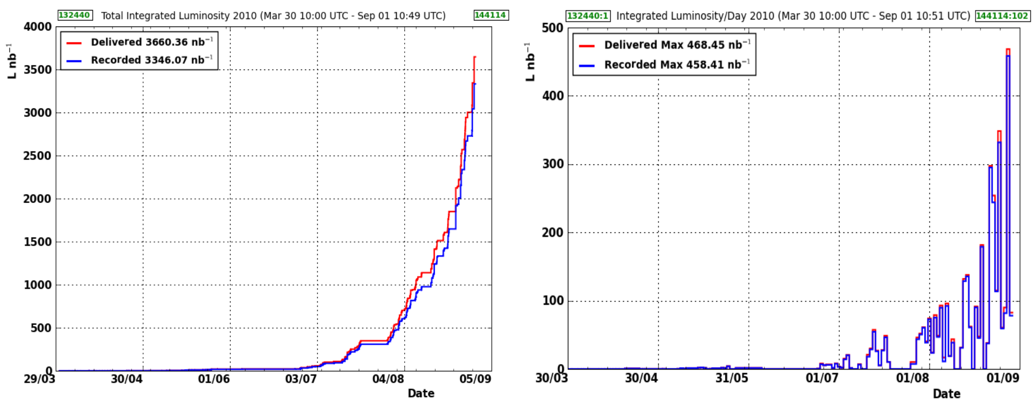

Figure 2.3: Total integrated luminosity delivered and recorded by CMS during the stable beams at 7 TeV center-of-mass energy (left) and that per day (right) till September 2010, which is the data quantity in this analysis. [21].

2.2.3 Potential new physics at LHC

Currently, high energy issues are studied with either accelerators or cosmic rays, including verifying the Standard Model (SM), looking for new physics beyond the SM, searching for Higgs boson, studying supersymmetry (SUSY), hunting dark matter, etc. With respect to Tevatron, which is an accelerator similar as LHC but with 7 times lower energy and by proton-antiproton collision, proton-proton mechanism leads to lower reaction cross section in the same energy scale. The high center-of-mass energy and luminosity at LHC will be a compensation for it. In addition, gluon fusion plays the dominant role in Higgs production, by which the cross section at LHC is close to proton-antiproton in the same energy. Thus, shown in Fig. 2.4, LHC has got a larger cross section in some reaction process (e.g. Higgs boson production), but a similar total cross section , which means higher signal in some certain processes at LHC and the similar background level between the two.

Higgs boson hunting

As explained above and in Section 2.2.1, LHC has the advantage on Higgs boson search over the previous accelerators. In theory, Higgs boson could be produced via gluon fusion, vector boson fusion and associative production process at LHC, in which the gluon fusion is the dominating mechanism. Here in the Fig. 2.5, the production cross section and main decay models are shown.

At the LEP, Higgs boson is excluded in the mass range lower than 114 GeV/c^2 at 95% confidence level and Tevatron also excluded Higgs between 158 GeV/c^2 and 175 GeV/c^2 at the 95% confidence level with combined results from CDF and D0. In the framework of SM, its mass is limited below 1 TeV/c^2. At LHC, these ranges available are categorized into three regions, i.e. low mass region, intermediate mass one (130GeV/$c^2 \leq M_H \leq 2M_Z$) and that of high mass. At low mass region, $H \rightarrow \gamma\gamma$ is the main decay channel. Two high energy photons will give a clear mass peak while the background photons are coming from $\mathrm{q}\bar{\mathrm{q}} \rightarrow \gamma\gamma$ and $Z \rightarrow e^+e^-$ or fake

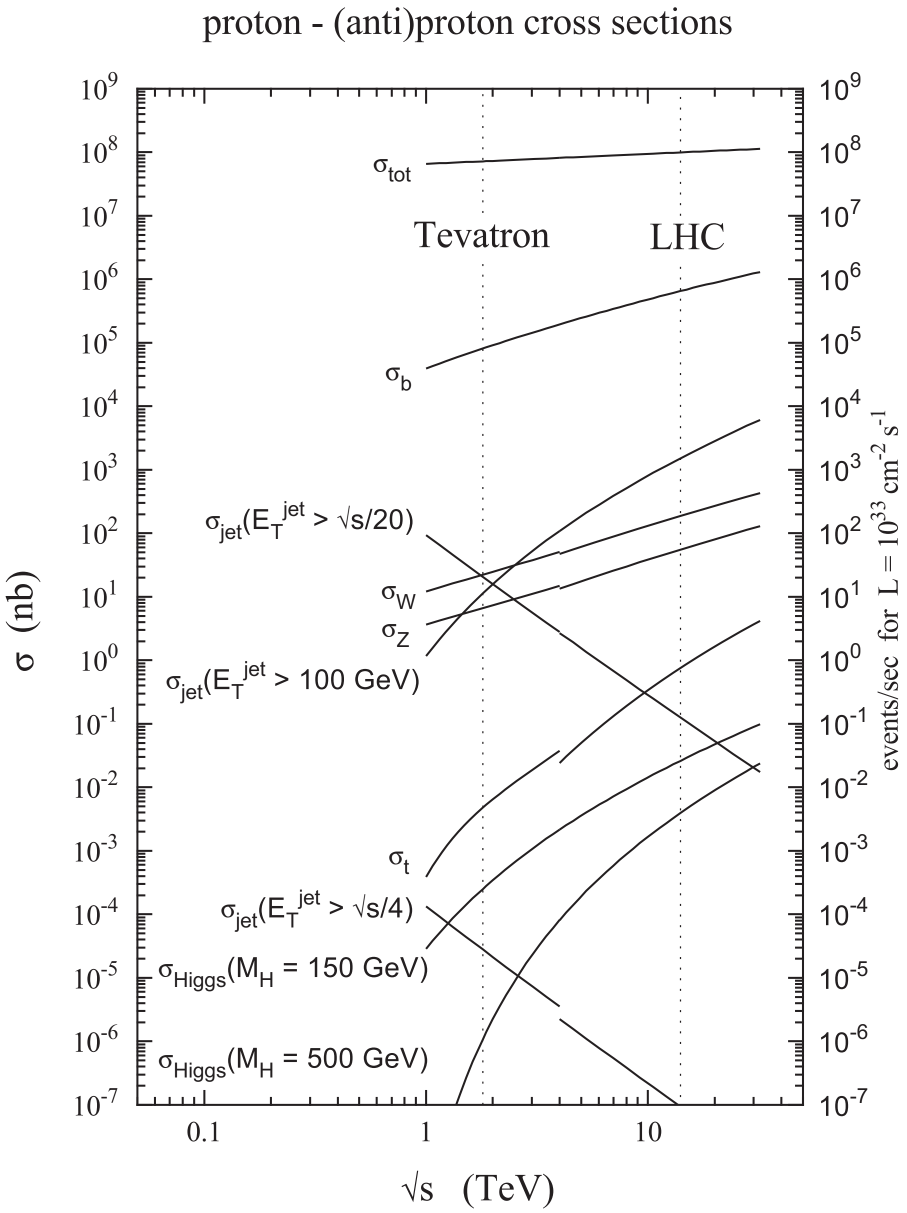

Figure 2.4: Expected cross sections and event rates of various physics channels under SM framework at Tevatron and LHC[23]. Natural units are used here.

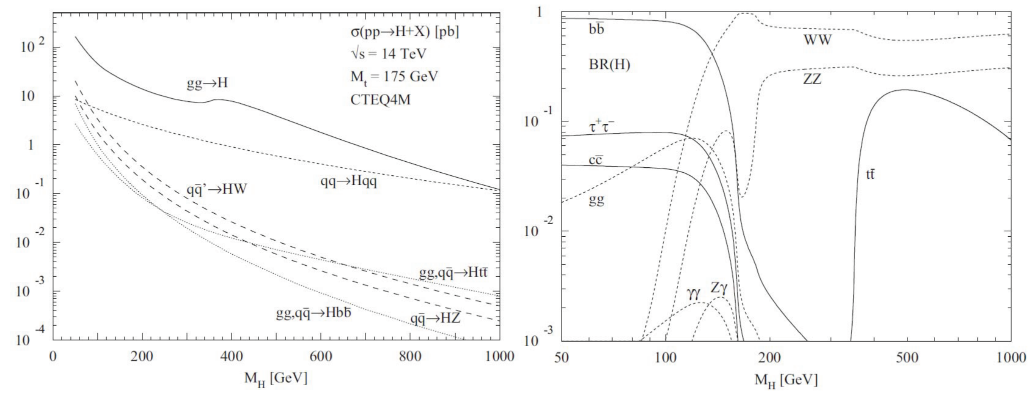

Figure 2.5: Higgs production cross sections under each mechanics (left) and relative event rates of main possible decay channels (right) as a function of higgs mass at LHC ($\sqrt{s} = 14$ TeV)[25].

photons from jets. In theoretical calculation, there is a 1% signal to background ratio and one much smaller decay width in this channel than that of $H \to \mathrm{b\bar{b}}$. For the intermediate mass region, the good channels are $H \to WW^{(*)} \to 2\ell 2\nu$ and $H \to ZZ^* \to 4\ell$ with one on-shell vector boson. The "golden" channel is the vector boson decay that $H \to ZZ \to 4\ell$ and $H \to WW \to 4\ell$ in high mass region. Because of large branch ratios, other channels, e.g. $H \to WW \to \ell\nu_\ell jj$ and $H \to ZZ \to \ell\bar{\ell}\nu_{\ell'}\bar{\nu}_{\ell'}$, could also be potential ones for the discovery of Higgs boson[26].

Supersymmetry (SUSY)

SUSY is an extension of the SM on theory. In SUSY, one elementary particle with one spin has its superpartner with spin differing by half of a unit. The superpartners of SM particles have not been discovered yet, which means SUSY must be a broke symmetry, i.e. the superpartners must have different masses to their SM sister particles. Higgs also extends to five Higgs in the Minimal Supersymmetric Standard Model (MSSM). If the superpartners with large mass at TeV scale exists and decays to the corresponding SM particles, R-parity violates. The neutrino like

SUSY particles cannot produce signals in detectors. Thus the SUSY group will measure the large missing transverse momentum and energy firstly.

Standard Model physics

Standard Model physics has a wide range of topics[23][24], listed below. Higgs boson study is also one part of the SM, but it is so important and worth to set it as a separate part.

- Standard processes:
  - σ_{total} and σ_{el} minimum bias event;
  - Jets and direct photons;
  - W/Z production cross section, WZ and $W\gamma$ pair production;
  - Drell-Yan production of lepton pairs;
- b-physics:
  - Production cross section of particles decayed from b-quark;
  - Polarization measurement;
  - CP violation;
- Top physics:
  - Top-quark search;
  - Mass determination and branch ratios measurement;
- Neutrino physics:
  - Direct observation of the σ_τ;
  - σ_e and σ_μ studies;

There are still a lot of questions in SM that puzzling scientists, e.g. the heavy quarkonia production cross section and its polarization have not been understood well yet. This thesis will focus on this topic.

2.2.4 Summary

LHC is a powerful big machine accelerating protons (or heavy ions in some periods) to close-to-light-speed, corresponding to very high energy and large cross section in physics process. Its instantaneous luminosity is also at the top of all existing accelerators and huge mount of events will be collected in detectors after collisions. The design parameters of LHC is shown in Table. 2.1. More details are referenced in the LHC Design Report[19].

Table 2.1: The Large Hadron Collider design parameters.

Circumference C	26659	m
Energy E	7	TeV
Dipole field B	8.4	T
Bunch spacing s	25	ns
Bunch population N	1.15×10^{11}	
Bunch radius $\sigma_x = \sigma_y$	16	μm
Bunch length σ_s	75	mm
Number of bunches n_b	2808	
Collision rate r_C	40.08	MHz
DC beam current I_b	0.58	A
Beam-beam parameter ξ	0.0034	
Luminosity L	10^{34}	$cm^{-2}s^{-1}$
Distance to nearest quadrupole ℓ_Q	± 23	m
Operating temperature T	1.9	K

2.3 CMS detector

Two beams with opposite directions will collide in the geometrical center of detectors. In CMS, secondary particles after beam collision and their decay productions hit sub-detector; information from the component sensor is used to reconstruct daughter and mother particles. From the inside outwards in an order of the shell like structure, there are beam pipe, pixel and silicon strip tracker, preshower, electromagnetic calorimeter (ECAL), hadron calorimeter (HCAL), solenoid magnet and muon chambers, shown in Fig. 2.6. Also within the CMS, a bunch of protons collide in every 25 ns, so a trigger system serves for acquiring only potentially interesting events.

Here are some numbers about CMS, with the weight up to 12500 tons, overall

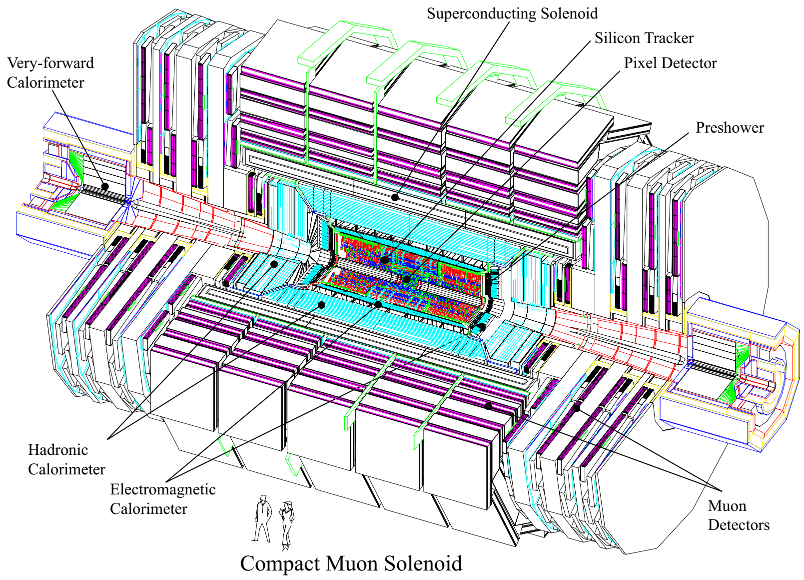

Figure 2.6: The structure of Compact Muon Solenoid (CMS).

diameter of $15m$, overall length of $21.5m$ and magnetic field as high as 3.8 Tesla.

In general, all charged particles could produce signals in the inner tracking system, electrons and photons produce signal light in ECAL. Hadrons with long life time (mesons like $\pi^{\pm}K^{\pm}\rho^{\pm}$ and baryons like proton and neutron) will deposit parts of energies in HCAL. Because of the large magnetic field and stopping power of previous sub-detectors with absorbing materials, few particles but muon could sail through so many planes ahead to the muon chambers. The detailed information about some CMS subsystems used in this thesis will be listed in the sections below.

2.3.1 CMS coordinate

Usually, a cylindrical coordinate is used to describe the positions and directions in CMS. But sometimes Cartesian coordinate system clarifies some longitudinal dimensional information. Fig. 2.7 shows these two coordinates. The common z-axis in both systems is at the center of CMS along the beam line towards the anti-clockwise direction. x-axis is pointing to the inside of LHC ring and y-axis is vertical upward[1]. The origin is the geometrical center of CMS.

In cylindrical coordinate, the polar angle θ is measured from the z-axis. In the xy-plane, the azimuthal angle ϕ in radius is defined starting at x-axis and radial coordinate (r) is the distance from the origin. The xy-plane in Cartesian coordinate is identical to the $r\phi$-plane in cylindrical one.

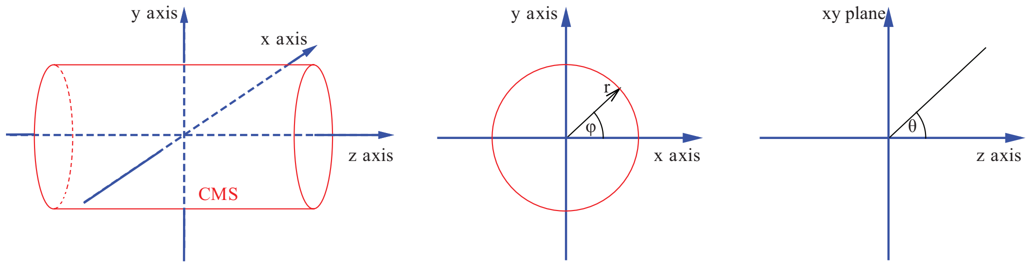

Figure 2.7: The coordinate system in CMS.

In particles physics analysis, one particle flies along the θ direction with momentum of $\vec{p}$. Its pseudorapidity is defined as,

$$\eta = -\,ln\,tan(\frac{\theta}{2}) = \frac{1}{2}ln(\frac{|\vec{p}|+p_z}{|\vec{p}|-p_z}), \tag{2.1}$$

where p_z is the z component of the particles momentum along the beam line. Thus a cone with $\Delta R = \sqrt{(\Delta\eta)^2+(\Delta\phi)^2}$ can be defined. Also, there is a rapidity value (y) for the particle, defined as

$$y = arctanh\frac{|\vec{p}|c}{E} = \frac{1}{2}ln(\frac{E+p_zc}{E-p_zc}). \tag{2.2}$$

In the limit that the particle travels in the speed close to the light, or its mass is nearly zero, these two values are close to each other numerically. But the pseudorapidity depends only on the spatial polar angle instead of the energy or the momentum. In the whole $J/\psi \to \mu\mu$ analysis, muons will be described in pseudorapidity (η) and J/ψ in rapidity (y).

[1]Here y in Romanic font stands for the y-axis, while later y in Italic font for pseudorapidity.

2.3.2 Inner tracking system

Outside the beam pipe, the closest sub-detector to the interaction point is the inner tracking sub-detector. It is designed for the efficient measurement on the trajectories of charged particles and to give a precise secondary vertex reconstruction. Its structure is shown in Fig. 2.8. Usually, CMS tracker is divided into two parts, the silicon pixel tracker which is inside (or named as CMS pixel detector) and silicon strip tracker outside.

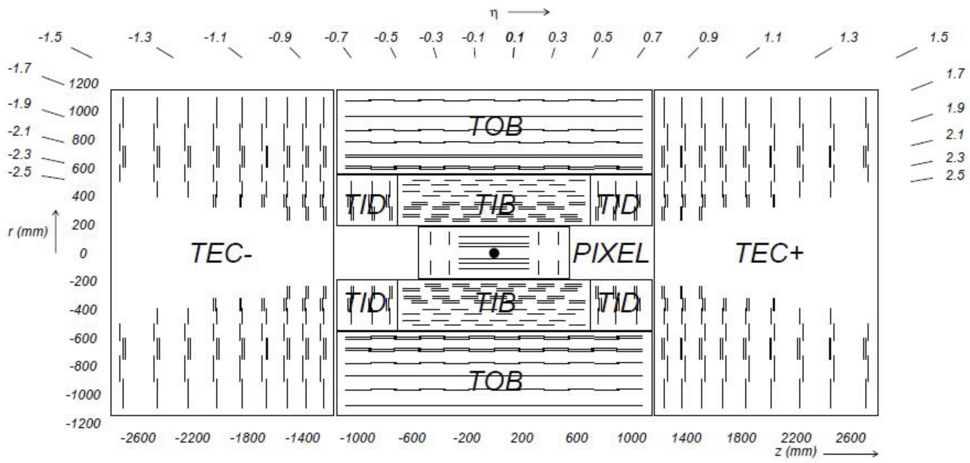

Figure 2.8: The tracker schematic structure in CMS[28].

As explained before, LHC will accelerate protons in high luminosity and in every $25ns$ and lots of secondary particles after collision will fly into the 4π solid angle. Being so close to the collision means the number of these secondary particles passing through the tracker is huge, around 10 million per cm^2 per second. Tracker will provide fast and precise (accurate to $10\mu m$) signals on every layers and the electronics will process these signals immediately. In addition, pixels and strips should withstand the strong radiation for 10-year-run of CMS.

Pixels are in the very central part of the whole CMS. Three cylindrical layers (pixel barrel, short for PXB) at $4.4cm$, $7.3cm$ and $10.2cm$ in radius and two propeller like disks at each endcap (pixel forward, PXF) at $|z| = 32.5cm$ and $46.5cm$ covering $|\eta| < 2.5$ region, totaly $53cm$ long about the size of a shoe box but with 65 million pixels, are used to provide the track segment of charged particles, as shown in Fig. 2.9. Once combining the pixels signals in each layer, a 3-D trajectory segment will be reconstructed. The resolution for the $\rho - \phi$ measurement is about $10\mu m$ and for z dimension is $20\mu m$.

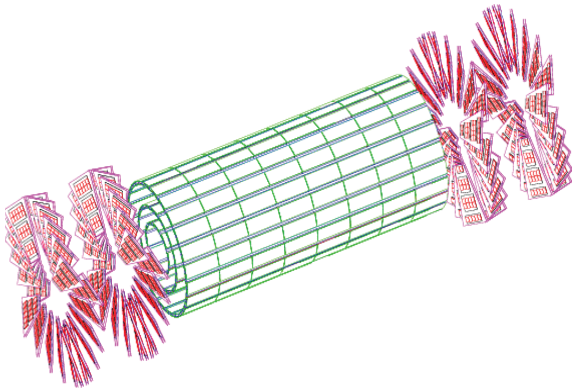

Figure 2.9: The silicon pixel tracker schematic view[28][29].

Outside the pixel, there are 10 layers of silicon strip tracker detector, as shown in Fig. 2.8. Firstly, four inner barrel (TIB) layers with two inner endcaps (TID±) consist of 3 small discs at each side form a can-like cylinder. Surrounding this can with the aligned edge, there is an outer barrel (TOB) by 6 layers. Finally, two 9-layer-endcaps (TEC±) close off the tracker. The barrel parts, i.e. TIB and TOB, cover the regions of $20cm < r < 116cm$ and $|z| < 118cm$. The radius of TID extends to $r = 55cm$. TEC is located at $124cm < |z| < 282cm$ and its radial range is up to $113.5cm$.

At end of this section, a short example on the tracker performance is given. In Fig. 2.10, the strips provide a good resolution on transverse momentum and transverse impact parameter in muon reconstruction under different momentum scales.

Table 2.2: The resolutions of silicon pixel and strip tracking subsystems.

Subsystem	Acronym	Direction	Resolution
Barrel Pixel	PXB	$r\varphi \times z$	$9 \times 21 \mu m^2$
Forward Pixel	PXF±	$r\varphi \times r$	$15 \times 25 \mu m^2$
Tracker Inner Barrel	TIB	$r\varphi$	$23 - 35 \mu m$
Tracker Outer Barrel	TOB	$r\varphi$	$35 - 53 \mu m$
Tracker Inner Discs	TID±	φ	$91 - 100 \mu rad$
Tracker Endcaps	TEC±	φ	$45 - 100 \mu rad$

2.3.3 Muon system

Muon detection is one of the most important tasks in CMS, that is why the "muon" is embedded in the detector name of CMS (compact muon solenoid). Muons are charged heavy point like particles, without interaction strongly with the metal materials so that they could penetrate layers of inner tracker and calorimeter to the outside of the magnetic yoke where the muon chambers are installed. Like other subdetectors, muon system is formed by the barrel part (MB, $|\eta| < 1.2$) and endcaps (ME, $0.9 < |\eta| < 2.4$), numbered and shown in Fig. 2.11. There are three kinds of chambers, drift tube (DT) chambers for the barrel part, cathode strip chambers (CSC) for the ME up to $|\eta| < 2.4$ and resistive plate chambers (RPC) for both barrel and endcap[37].

Drift tube chambers

As explained in previous section, the yoke comprises of five wheels. Each wheel is composed of 4 layers and divided into 12 pieces of $30\,^{\circ}$-sector (labeled as sector $1 \sim 12$ from $\phi = 0$), shown in Fig. 2.12. The DT chambers, that 4 layers (namely stations, labeled MB1 $\sim$ MB4) at the $r = 4.0, 4.9, 5.9 \text{and} 7.0 m$, are organized along this structure of YB. Chambers at section 3 and 4 in YB-1 and YB+1 are $40 cm$

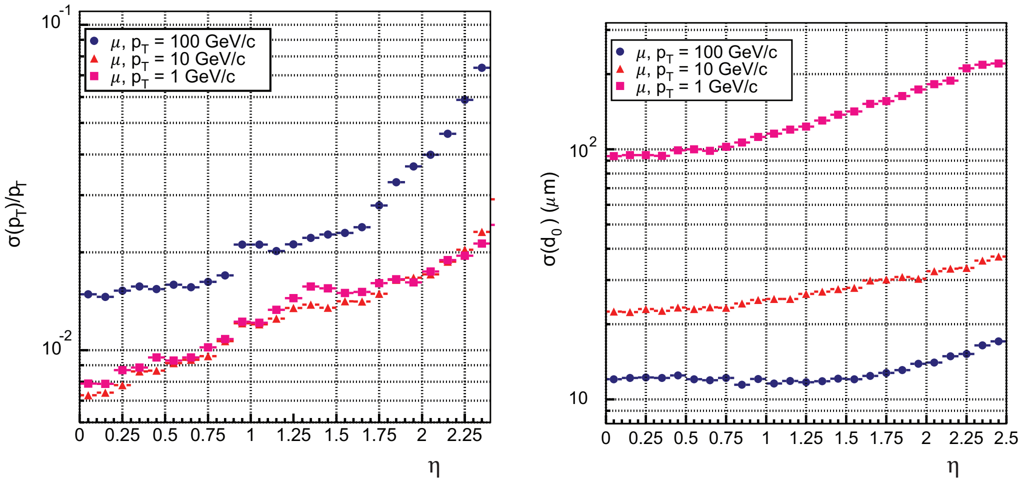

Figure 2.10: Transverse momentum resolution (left) and transverse impact parameter resolution (right) vs. pseudorapidity for muons[30].

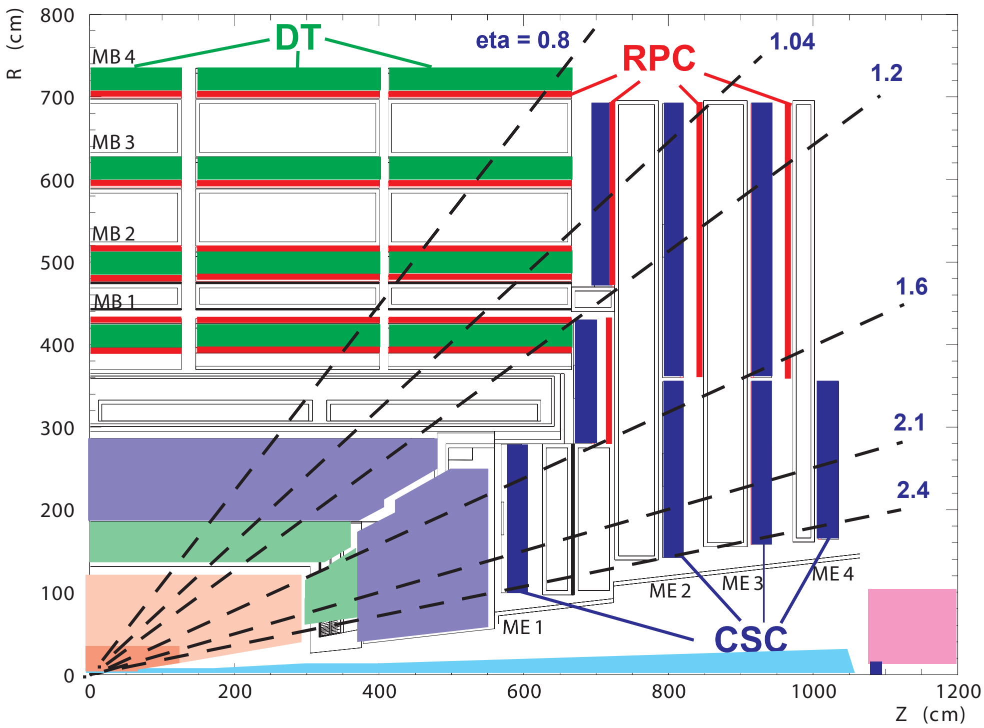

Figure 2.11: A schematic view on the muon chambers layout. The RPC system is limited to $|\eta| < 1.6$ and the CSC on ME4 just covers the non-RPC part.

shorter along the z direction than other chambers for the chimneys space of the magnetic cryogenic lines. In the two inner stations MB1 and MB2, DT chambers are held between two RPCs forming a sandwiched structure. MB3 and MB4 are formed by DT chambers with one inside layer of RPCs, that could be one, two or four, depending on in which sector and station it is. So one high p_T muon will travel through 6 RPCs and 4 DT chambers ideally. The DT chambers are overlapped in different layers to avoiding the gap effect.

One $2m\times2.5m$ DT chamber, comprised of three groups of four, totally 12 aluminium layers. The 3 innermost stations, i.e. MB1$-$MB3, measure the (r,ϕ,z) while the MB4 only measures (r,ϕ) without z, since MB4 does not contain the z-measuring planes. The maximum size of one drift is 2.0cm, the single point resolution is 200μm and ϕ resolution is 1 $mrad$.

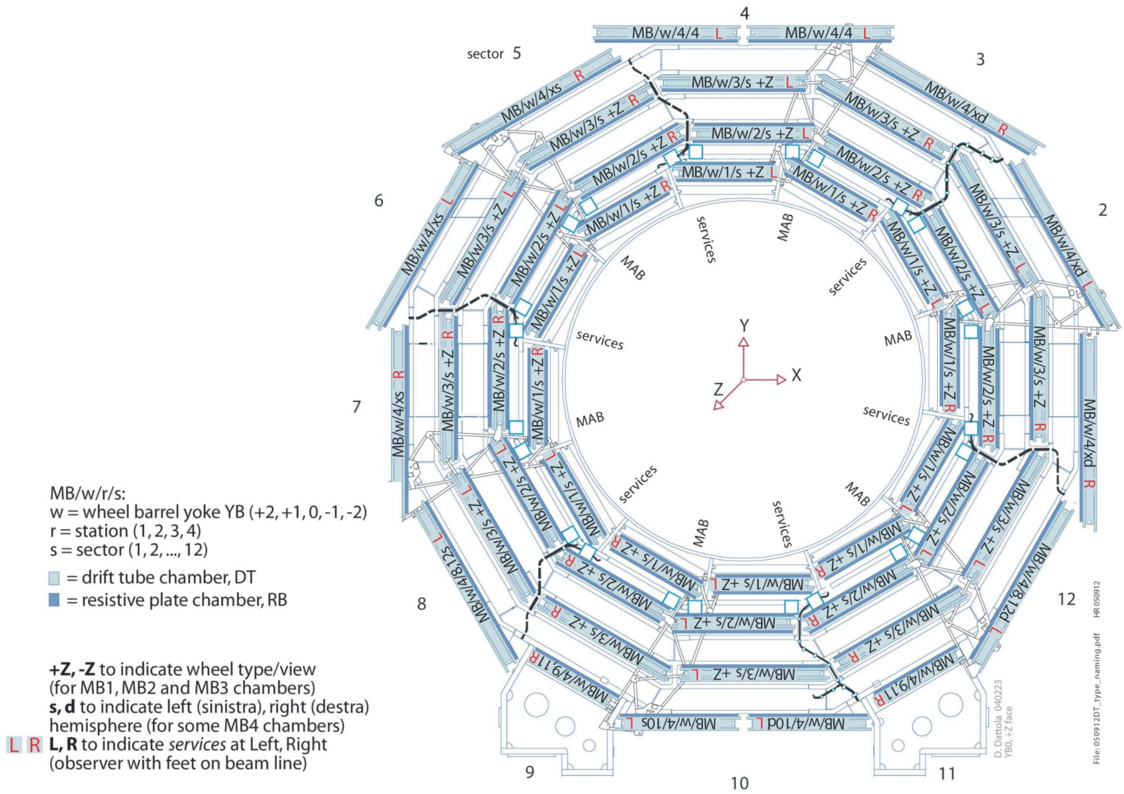

Figure 2.12: A sector plan of the YB+2, with four layers and twelve 30°-sectors.

Resistive plate chambers

RPCs are laying in both barrel and endcaps, providing very fast response (10 kHz/cm^2 operation rate) but not so good position resolution as DT or CSC. One RPC is formed by two layers of double-gap bakelite chamber with a $2mm$ gap holding the readout between these two layers. Totally there are 480 RPCs in barrel and 540 in endcap.

Cathode strip chambers

At each endcap of muon system, four layers (stations) of CSC are laying on the yoke discs labeled ME1 to ME4 from inside outwards, totally 468 CSCs in the 2 endcaps. Each station is divided into 2 (3 for ME1) concentric rings around the beam line, shown in Fig. 2.13. Except the third ring (ME1/3) of the first disc, CSCs are overlapped in ϕ to hide the gaps. ME2/1, ME3/1 and ME4/1 have 18 chambers and other ME rings have 36. The gas ionization and subsequent electron avalanche by one charged passing particle will fire the anode wire and a group of cathode strips. Wires and strips are perpendicular with each other and they could provide three dimension measurement on (r, ϕ, z). RPCs stick to CSCs behind at the first three layers.

Performance

Muon chambers will measure the hits with momentum and time information to reconstruct muon segments, namely stand alone muons. Adding the inner track information in, a matched "tracker track"-"standalone muon" pair forms one global muon. The momentum resolution as a function of muon momentum is shown in Fig. 2.14. For the muon segment labeled "Muon system only", multiple scattering affects the momentum resolution the most when muon momentum is less than 200 GeV/c and the chamber spatial resolution dominates whilst $p_\mu > 200$GeV/c. Combined with inner tracker track, which gives a much better resolution that the multiple

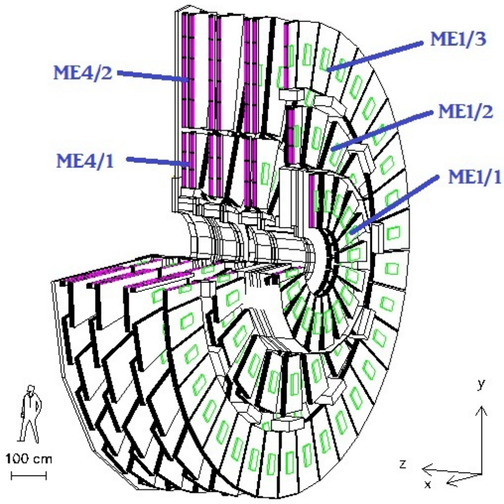

Figure 2.13: A layout of muon endcap.

scattering and energy loss can be ignored.

2.3.4 CMS trigger and data acquisition

LHC bunches are colliding in CMS at 40 MHz which is a very high rate corresponding to about 10^9 interactions per second in its designed luminosity $10^{34}\ cm^{-2}s^{-1}$. This is too high frequency for the signal process unit and storage media to handle and store data. The trigger and data acquisition system are proposed into dispose the prompt data from CMS subdetectors and reject most of the rubbish events at a factor of 10^6. This system consists of four parts, that detector electronics, the Level-1 (L1) Trigger , the readout network and the online High-Level-Trigger (HLT) event filter[38]. The CMS Trigger has two levels, i.e. the L1 and HLT. L1 trigger is a hardware based data filter by the information from calorimeter, muon system and some correlation of information between the two, while HLT is a software one in processors by further combinations and other topological calculations on the digital list of objects extended from L1 trigger. At different periods of LHC luminosity, different HLT trigger menus will be added to the data acquisition system.

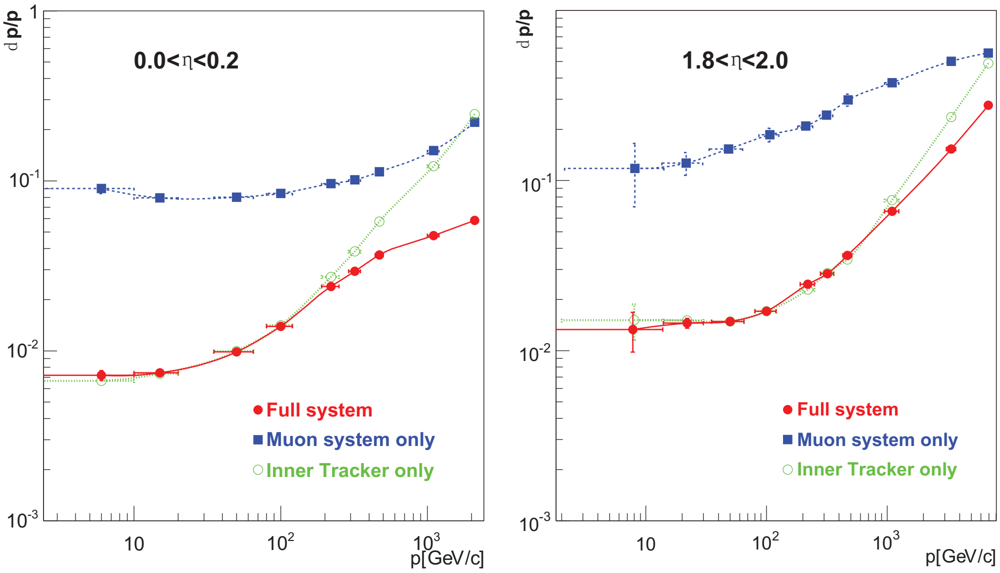

Figure 2.14: The momentum resolution of muon reconstruction in muon system, inner track and full system in barrel (left) and endcap (right) regions[38].

Level-1 trigger

L1 trigger is organized into three major parts, i.e. the L1 calorimeter trigger, the L1 muon trigger, and the L1 global trigger, shown in Fig. 2.15.

The LHC collision rate is 40 MHz while the L1 pipeline data storage time is $3.2\mu s$. Considering the signal propagation delay, which is included in the pipeline responsive time, the L1 trigger process time must be finished in less than one microsecond. For sub-L1-systems, the calorimeter trigger preserves the tower energy sums from the ECAL, HCAL and HF individual cells (or towers) and reconstructed candidates of electrons, photons, taus and jets. Thresholds will be added on these particle candidates. In design, for instance, the transverse missing energy trigger requires the events with MET (transverse missing energy) greater than 100 GeV, but at the very first low luminosity this trigger is not enabled. The muon subtrigger focuses on μ preselecting. Information from DT, CSC and PRC is used to drop events with low quality muons. The global muon trigger (NOT the global trigger) converts muon tracks from different chambers into the same η, ϕ and p_T scale, then

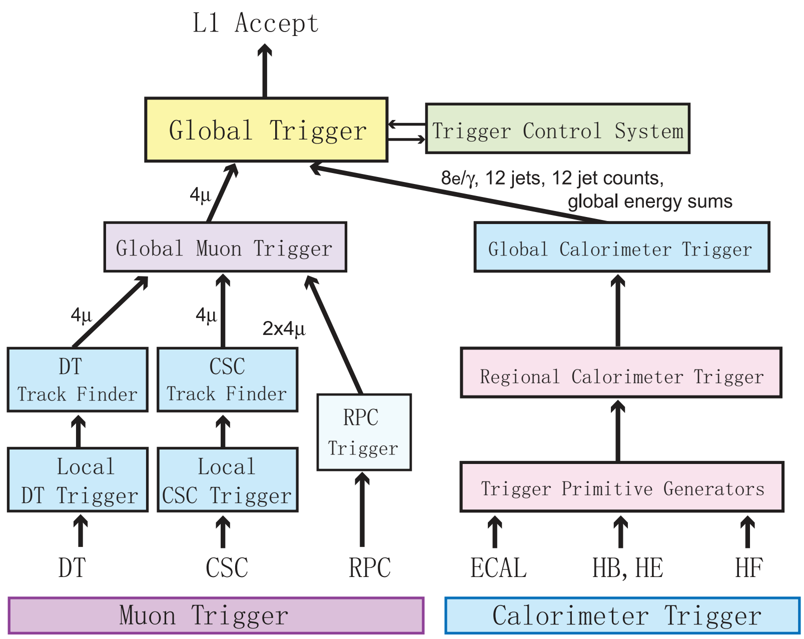

Figure 2.15: The organization of Level-1 Trigger system by calorimeter subtrigger system, muon one and the global one.

to correlate the tracks. Also another important task for global muon trigger is to identify whether the muon is isolated or not via vetoing the event with an $\eta - \phi$ grid of unquiet calorimeter towers. The global L1-subtrigger holds a time match on these information from both calorimeter and muon chambers, and decides to accept or reject each bunch crossing based on the logical combination only if both previous subtriggers said "yes" in proposing. Eventually, the L1 output data rate is limited to 100 kHz.

High level trigger

The data from L1 trigger will be sent to further event filtering and offline computing systems. The maximum data rate for the current system to handle is 100 GB/s and each event is about 1.5 MB for pp interaction. After L1 trigger process, the event rate is limited to about 100 kHz. Then the Data Acquisition system (DAQ), shown in Fig. 2.16, will further reduce the data further to 100 Hz to meet the peripheral computing and storage systems requirement.

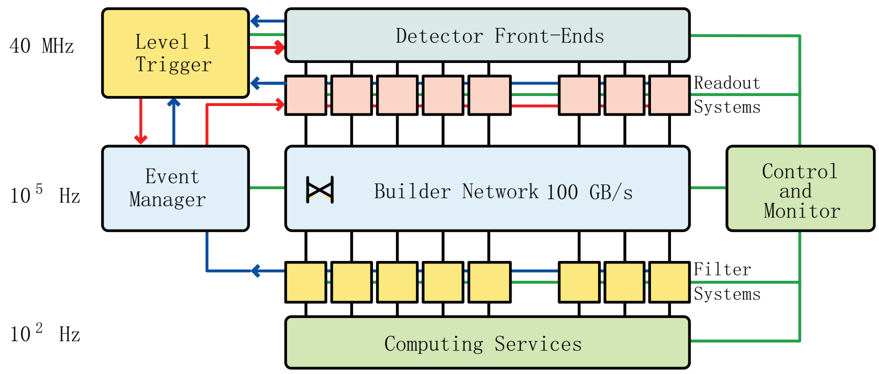

Figure 2.16: The architecture of the DAQ system.

HLT is a software based event filter system running on a computer farm, which is similar as the offline data analysis. All information used in L1 will be combined further and other topological calculations are also help to identify the quality of events. Other extra information, e.g. the tracker and the full granularity of the calorimeters, will also be brought into the HLT analysis. Finally, the HLT reconstruction and event filtering will provide an easy access data on storage media. HLT menu changed a lot since the startup of the LHC and often changes in the increasing instantaneous luminosity.

2.4 CMS software

The CMS software (CMSSW) is mainly about the data transferring, computing and analyzing.

2.4.1 CMSSW framework

After the data arrives at personal user interface, CMSSW will be run on these data to get physics plots and numbers.

The whole CMSSW framework is based on an Event Data Model (EDM) for the analysis is not only for the real data but also for the simulated Monte-Carlo data. The core program is C++ and in linux system python script program calls these C++ modules. The data, no matter RAW, RECO, AOD or FEVT[2], is stored as a single entity in memory in a C++ type-safe container named *Event*. One event is from one collision in detector. Information, such as tracks, energy reconstructed from calorimeter and so on, is stored as different C++ class.

In software, one event is picked into memory from *POOLSource* and plug-in modules are executed on it. One could manage data to process, modules to execute, sequence of the modules, parameters to set and files to output in one python configure file. More detail could be checked in CMS workbook[45].

Recently, a new analysis-oriented data format is invented, namely Physics Analysis Toolkit (PAT), developed by Physics Objects Groups. It contains most of the information for analysis but limit the size of data file. Compared with reco::Candidate class, pat::Candidate carries more information on object resolution, correction factors to the jet energy, parameterized reconstruction, etc. The arithmetic and structure of data in C++ classes are more easily to access. From RECO to PAT, analyzers could decide what information to preserve and what to throw away by reseting the parameters in configure file, which reduces the data file size. For instance, pat::Muon is used in this thesis. There are these extra information to reco::Muon, that tracks from a TeV refit, isolation in predefined core, match on generator level and trigger level, etc.

2.4.2 Monte Carlo generators in CMSSW

For Monte Carlo data, CMSSW offers interface of some MC event generators, e.g. the traditional Pythia6[63], Herwig6 and some new ones like Pythia8, Herwig++, Sherpa. In this study, MC events are generated in Pythia6, one of the most general-purpose event generators, by calling an EvtGen class.

Generators describe the physics process in particle collisions, such as hard interactions, soft ones, initial and final state parton showers from theories. People

[2]Full EVenT data, the event combined RAW with RECO data.

try to cover more details and give a more accurate result, usually based on theoretical calculation. Matrix elements in generator code are set carefully, corresponding to the event interaction at parton level. For instance, in quarkonia generation, MSEL(61)=1 means all channels for quarkonia generation is switched on. Other important matrix elements from NRQCD in the prompt J/ψ and Υ generations are shown in Table 2.3. More information about this are reference[55].

Table 2.3: NRQCD matrix elements of J/ψ and Υ and corresponding parameters in Pythia [55].

Pythia setting	Value	Matrix element
PARP(141)	1.16	$\langle O(J/\psi)[^3S_1^{(1)}]\rangle$
PARP(142)	0.0119	$\langle O(J/\psi)[^3S_1^{(8)}]\rangle$
PARP(143)	0.01	$\langle O(J/\psi)[^1S_0^{(8)}]\rangle$
PARP(144)	0.01	$\langle O(J/\psi)[^3P_0^{(8)}]\rangle/m_c^2$
PARP(145)	0.05	$\langle O(\chi_{c0})[^3P_0^{(1)}]\rangle/m_c^2$
PARP(146)	9.28	$\langle O(\Upsilon)[^3S_1^{(1)}]\rangle$
PARP(147)	0.15	$\langle O(\Upsilon)[^3S_1^{(8)}]\rangle$
PARP(148)	0.02	$\langle O(\Upsilon)[^1S_0^{(8)}]\rangle$
PARP(149)	0.02	$\langle O(\Upsilon)[^3P_0^{(8)}]\rangle/m_b^2$
PARP(150)	0.085	$\langle O(\chi_{b0})[^3P_0^{(1)}]\rangle/m_b^2$

In addition, simple particle guns are also interfaced in CMSSW. This tool offers only single particles from any vertex position with fixed or a region of transverse momentum, energy, flying angle, etc. Extra programme can be used to control the decay and attain the daughters. In CMSSW, there are already many examples of Pythia6 and Particlegun configuration codes in directory of $Configuration/Generator$ and $Configuration/GenProduction$ (configuration fragments at generator level).

Chapter 3

Theoretical motivation and background

This section reviews the standard model (SM) of particle physics briefly. In the framework of SM, QCD theory plays an important role in the prediction of heavy quarkonium production in hadron collision. Some theoretical models are established from QCD, e.g. the color evaporation model (CEM), the color singlet model (CSM), the color octet mechanism (COM), etc. Different predictions by these models are also compared with experimental results from CDF, D0 and CMS.

3.1 Standard model

Standard model is a combined theory, including the quantum electrodynamics (QED) and quantum chromodynamics (QCD). It is the most accepted theoretical model nowadays in particle physics, since the results from theoretical predictions and explanations have been verified by high energy experiments well.

The elementary forces

Standard model explains three elementary interactions, i.e. the strong, electromagnetic and the weak forces[1], by exchanging vector bosons (with spin=1) associated. The summery of these three interactions is listed in Table. 3.1. In addition, the fourth interaction, gravity, is described by Einstein's general theory of relativity, which has not been included in standard model yet, and will not be touched in this thesis.

Table 3.1: The summary of three elementary interactions described by standard model[46].

Interaction	Couples to	Range	Mediator(s)	Mass	J^P
strong	color charge	$10^{-13}cm$	8 gluons (g)	0	1^-
electromagn.	electric charge	Infinity	photon (γ)	0	1^-
weak	weak charge	$10^{-16}cm$	$W^{\pm}, Z^0$	$\approx 10^2\text{GeV}/c^2$	1

Because photons have zero mass, the range of electromagnetic force is infinite. The exchanged bosons ($W^{\pm}, Z^0$) in weak interaction are so heavy that the range is limited at only 10^{-16} cm. The electromagnetic and weak forces are unified into a single interaction, namely electroweak interaction. Strong interaction is more complex, by exchanging color carried by quarks and gluons. Strong force increases while the distance between quarks becomes larger. But in experiment, single quark has never been observed, therefore observable particles should be always presumed as color neutral (freed due to color confinement). This limits the range of strong interaction.

[1] The electromagnetic and weak forces were unified as electro-weak interaction since 1970's.

The fundamental particles

The elementary forces interact the known fundamental fermion (with spin=$\frac{1}{2}$), i.e. quarks and leptons. They are grouped into three generations (or families), summarized in Table. 3.2. Further generation of quarks or leptons with a massless neutrino is excluded in the measurement of Z^0 resonance width.

Table 3.2: Three generations of fundamental particles[46].

Fermions	Family			E.charge	Color	Weak isospin		Spin
	1	2	3			left-hd.	right-hd.	
Leptons	ν_e	ν_μ	ν_τ	0	—	1/2	—	1/2
	e	μ	τ	-1			0	
Quarks	u	c	t	+2/3	r,b,g	1/2	0	1/2
	d	s	b	-1/3			0	

The mass of fermion differs a lot from each other. Generally, the mass increases from lower generation to higher. In history, neutrino is assumed to be massless until experiments set higher mass limits decades ago. Every fundamental fermion is associated with an anti-fermion, who has the same invariant mass value but opposite electric charge, color and the third component of weak isospin.

Standard model

The basic particle world is made up of fermions and anti-fermions coupled to mediator bosons. In the framework of SM, QED explains the electroweak interaction and QCD describes the strong interaction. For the strong interaction, the underlying symmetry is known as $SU(3)_C$ in group theory and the gauge group of the electroweak interaction is $SU(2)_L \times U(1)_Y$. Usually, the standard model is formulized to $SU(3)_C \times SU(2)_L \times U(1)_Y$.

3.2 Quantum chromodynamics

$SU(3)_C$ symmetry group models the behavior of strong interaction carried by quarks and gluons. This gauge theory is named quantum chromodynamics (QCD). To obey the Pauli exclusion principle, an additional freedom (or one property, more exactly speeking) named color is proposed to quarks and gluons, i.e. the charge of strong interaction. For instance, the particle $\Delta^{++} = |u^{\uparrow}u^{\uparrow}u^{\uparrow} >$ is found to have $J^P = 3/2^+$, i.e. the partons inside have identical flavors and wave functions. Each quark carries one different color, which could be red(r), green(g), blue(b), anti-red($\bar{r}$), anti-green($\bar{g}$) and anti-blue($\bar{b}$). Sum of the three colors or three anti-colors lead to white (color-neutral). So does the combination of one color and its anti-color. The gluon, a more complex point-like particle, carries both of color and anti-color. $SU(3)_C$ symmetry group theory allows 3×3 multiple color states, a single and an octet one.

There are two properties in QCD, asymptotic freedom and color confinement. The asymptotic freedom means quarks and gluons will have arbitrarily weak interactions in very short distances in very high energy scale, i.e. they act as free particles. The asymptotic freedom determines the renormalized QCD coupling is small in high energy collisions, which could be described by perturbation theory. The color confinement refers that interactions between quarks will increase with distance between each other sharply. Thus, color confinement forbids the existence of any free quarks since so much energy to separate two quarks could produce a new pair of quark-antiquark out of the vacuum.

A typical QCD cross section could formulized perturbatively to be,

$$\sigma = A_1\alpha_s + A_2\alpha_s^2 + \cdots \tag{3.1}$$

where the α_s is the fundamental coupling constant of QCD, measured by experiment. It is a “constant” but varies with four momentum transfer (Q) in the QCD process. Fig. 3.1 presents the different values of α_s. The coupling is weak at high energy scale and corresponds to the relatively free quarks, which could be described by the perturbative QCD (pQCD).

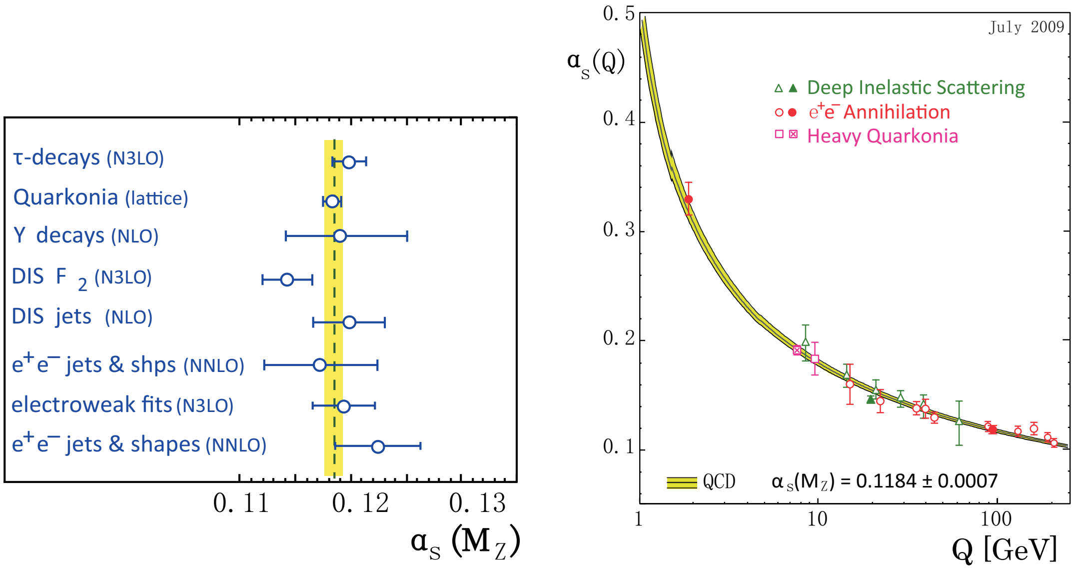

Figure 3.1: Summary of the $\alpha_s(M_Z)$ from various processes (left), where the respective energy scale is chosen to be the world average M_Z, and the α_s as a function of the energy scale (right). [8]

On the contrast, coupling is growing strong at low energy scale, where the calculation is based on factorisation theorem instead of perturbative theory. First, an universal wave function, known as the Parton Distribution Function (PDF), is proposed to describe the momentum distribution of the valence quark and gluons. Those partons' evolution is a function of the four-momentum transfer (Q) and the parton momentum fraction (x), measured by fitting processes at many independent experiments. The PDF of type i parton is marked as $f_i(x, Q^2)$, so the $f_i(x, Q^2)dx$ is the probability that one parton exists with a fraction of momentum from x to $x + dx$.

Considering both of the high energy perturbation and the wave function at relatively low energy scale, the QCD hadronic cross section of parton could be written as,

$$d\sigma_{QCD} = \sum_i \int dx f_i(x, Q^2) \otimes \sigma_{pertu} \tag{3.2}$$

where, the σ_{pertu} is the cross section from pQCD calculation. For the historical reason as well as that of convention, the perturbative cross section is named as the hard part and the other PDF part is the soft one.

3.3 Heavy quarkonia production in hadron collision

In practice, the QCD cross section is calculated to leading order (LO), or to next-to-leading-order (NLO), or to next-to-next-to-leading-order (NNLO). This section introduces the heavy quarkonium family and their potential production mechanism. Till now, none of these theoretical model gave very good prediction to both of the production cross section and the polarization simultaneously. Recently, three elements in color octet mechanism is recalculated by physicists at Peking University and their theoretical prediction is closer to the experimental measurement[48].

3.3.1 Heavy quarkonia family

At the beginning of this section, heavy quarkonium family is introduced. J/ψ, Υ and their excitation states are the most frequently studied heavy quarkonium. Table. 3.3 lists the charmonium family ($c\bar{c}$) and Fig. 3.2 shows the members. As well, the bottomonium's ($b\bar{b}$) is summarized in Table. 3.4 and Fig. 3.3.

A third heavy quark is found and named *top* at CDF and D0 in 1994. Due to its very large mass and very short lifetime(about 20 times shorter than the hadronic process), no toponium ($t\bar{t}$) is expected.

The quarkonia category

The quarkonia could come from several channels. In the case of J/ψ's production, c$\bar{\text{c}}$ bind state may come from collision (*direct* J/ψ, one kind of *prompt* J/ψ), or from the radiative decay of high energy excitation states (*prompt* J/ψ), or

Table 3.3: The charmonium family[47].

Meson	$n\,^{2S+1}L_J$	J^{PC}	$Mass$(GeV/c^2)	$\Gamma_{\mu\mu}$(KeV)
η_c	$1\,^1S_0$	0^{-+}	2.980	—
J/ψ	$1\,^3S_0$	1^{--}	3.097	5.40
χ_{c0}	$1\,^3P_0$	0^{++}	3.415	—
χ_{c1}	$1\,^3P_1$	1^{++}	3.511	—
χ_{c2}	$1\,^3P_2$	2^{++}	3.556	—
h_c	$1\,^1P_0$	1^{+-}	3.523	—
$\eta_c(2S)$	$2\,^1S_0$	0^{-+}	3.594	—
$\psi(2S)$	$2\,^3S_1$	1^{--}	3.686	2.12

Table 3.4: The members of bottomonium family[47].

Meson	$n\,^{2S+1}L_J$	J^{PC}	$Mass$(GeV/c^2)	$\Gamma_{\mu\mu}$(KeV)
$\Upsilon(1S)$	$1\,^3S_1$	1^{--}	9.460	1.26
$\chi_{b0}(1P)$	$1\,^3P_0$	0^{++}	9.860	—
$\chi_{b1}(1P)$	$1\,^3P_1$	1^{++}	9.893	—
$\chi_{b2}(1P)$	$1\,^3P_2$	2^{++}	9.913	—
$\Upsilon(2S)$	$2\,^3S_1$	1^{--}	10.023	0.32
$\chi_{b0}(2P)$	$2\,^3P_0$	0^{++}	10.232	—
$\chi_{b1}(2P)$	$2\,^3P_1$	1^{++}	10.255	—
$\chi_{b2}(2P)$	$2\,^3P_2$	2^{++}	10.269	—
$\Upsilon(3S)$	$3\,^3S_1$	1^{--}	10.355	0.48

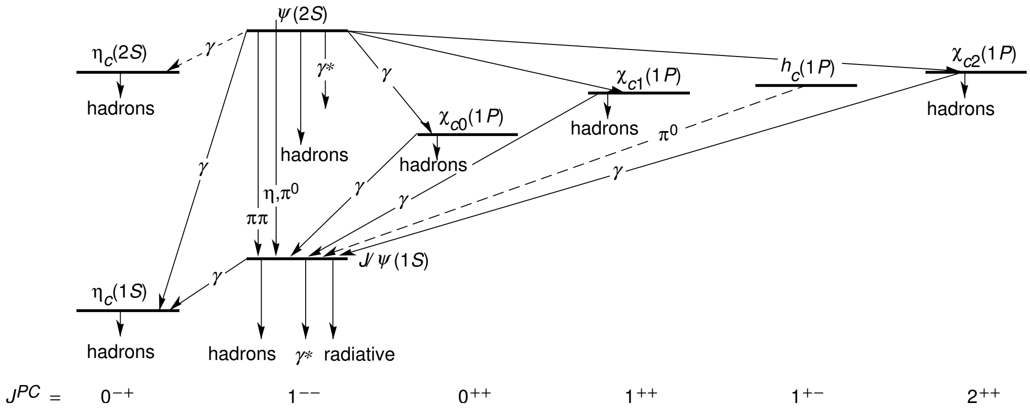

Figure 3.2: The charmonium family[47].

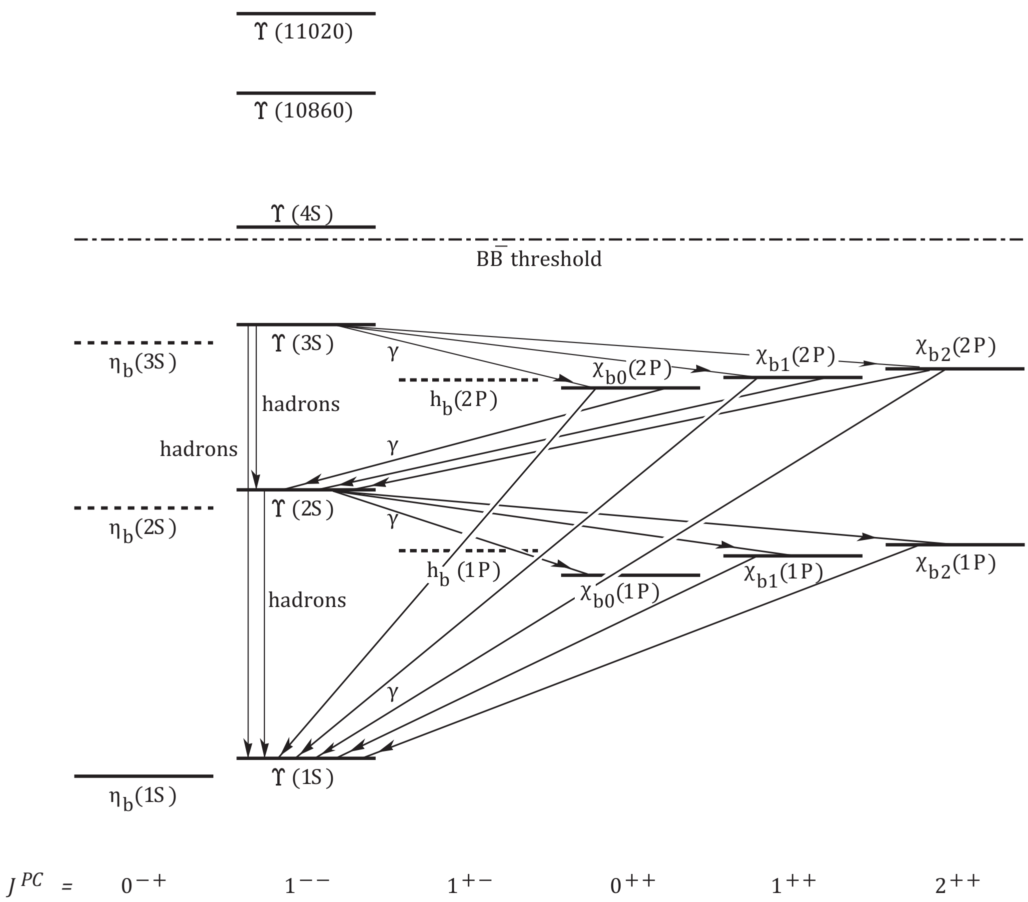

Figure 3.3: The bottomonium family[47].

from the b-hadron's decay (*nonprompt* J/ψ), summarized in Table 3.5. The first two are labeled to *prompt* ones is due to their emergences at the primary vertex of the reaction, while the third one is not since b-hadron has a relatively long lifetime ($\sim 1.5ps$) and the c-quark appears at the secondary vertex with a relatively large distance ($\sim cm$) from the primary one. This provides the opportunity to distinguish the prompt and nonprompt components. The $\psi(2S)$ and $\Upsilon(nS)$ have got the similar categories, shown in Table. 3.6. All prompt $\psi(2S)$ are direct and all $\Upsilon(nS)$ are prompt ones.

Table 3.5: The category of J/ψ production.

1^{st} step	2^{nd} step	3^{rd} step	Type
	$c\bar{c} \to J/\psi$	—	directly prod. (prompt)
$pp \to c\bar{c} + X$	$c\bar{c} \to \chi_c$	$\chi_c \to J/\psi + \gamma$	Prompt prod. by decay of χ_c
	$c\bar{c} \to \psi(2S)$	$\psi(2S) \to J/\psi + X$	Prompt prod. by decay of $\psi(2S)$
$pp \to \bar{b}c + X$	$c\bar{c} \to J/\psi$	—	Nonprompt
$\bar{b}c \to c\bar{c} + \ell^- + \bar{\nu}_\ell$	$c\bar{c} \to \chi_c$	$\chi_c \to J/\psi + \gamma$	prod.
$\cdots$			

Another principle in high energy scale is that $p\bar{p}$ and pp collisions should have the similar results for the consistent kinematics, since the valence quark gives small contribution in the evolution.

3.3.2 Some early theoretical models

In history, Charmonium and Bottomonium are studied carefully since their discovered. They are really good source to test the QCD process, e.g. the pro-

Table 3.6: The category of $\psi(2S)$ and $\Upsilon(nS)$ productions.

1^{st} step	2^{nd} step	3^{rd} step	Type
$pp \to c\bar{c} + X$	$c\bar{c} \to \psi(2S)$	—	Direct/Prompt
$pp \to \bar{b}c + X$ $\bar{b}c \to c\bar{c} + \ell^- + \bar{\nu}_\ell$ $\cdots$	$c\bar{c} \to \psi(2S)$	—	Nonprompt prod.
$pp \to b\bar{b} + X$	$b\bar{b} \to \Upsilon(nS)$	—	Direct prod.
	$b\bar{b} \to \chi_b$	$\chi_b \to \Upsilon(nS) + \gamma$	Prompt from χ_b
	$b\bar{b} \to \Upsilon(mS)$	$\Upsilon(mS) \to \Upsilon(nS) + X$	Prompt from $\Upsilon(mS)$

duction of heavy quarkonia in hadron collision contains both of the pQCD and non-perturbative process.

3.3.2.1 Color singlet model

The most natural model inheriting the QCD is the color-singlet model (CSM). Applying QCD to heavy quarkonia production in high energy collision, where the hard part is calculated by pQCD and the soft part is described by PDF, the cross section is given by convolution of these two parts[10],

$$d\sigma = \int dp \Phi(\vec{p}) \mathcal{M}(p) \delta(2p^0) \approx \mathcal{M}|_{p=0} \otimes \Phi|_{\vec{x}=0} \tag{3.3}$$

where, the $\mathcal{M}(p)$ is the perturbative amplitude with relative momentum p computed with the usually Feynman rules shown in Fig. 3.4 and $\mathcal{M}|_{p=0}$ is the S-wave, the $\Phi(\vec{p})$ is the usual wave-function in coordinate space and $\Phi|_{\vec{x}=0}$ means its value at the origin for the S-wave. If the perturbative part $\mathcal{M}(p)$ is treated at the leading order in α_s, the result is the Leading Order CSM (LO CMS). The approximate simplification is based on the S-wave, i.e. the $^3S_1$ state.

This model postulates the quarkonia production is formed in two steps. One step is that two *on shell* heavy quarks (Q and $\bar{Q}$) are produced from gluon fusion. The relative momentum scale is about $M^2 + P_T^2$, in which the heavy quark has got a large mass and high energy collision provides a large transverse momentum transfer, and this part is surely calculated by pQCD with Feynman diagram. The possible processes that the $^3S_1$ states produced with a gluon, are shown in Fig. 3.4.

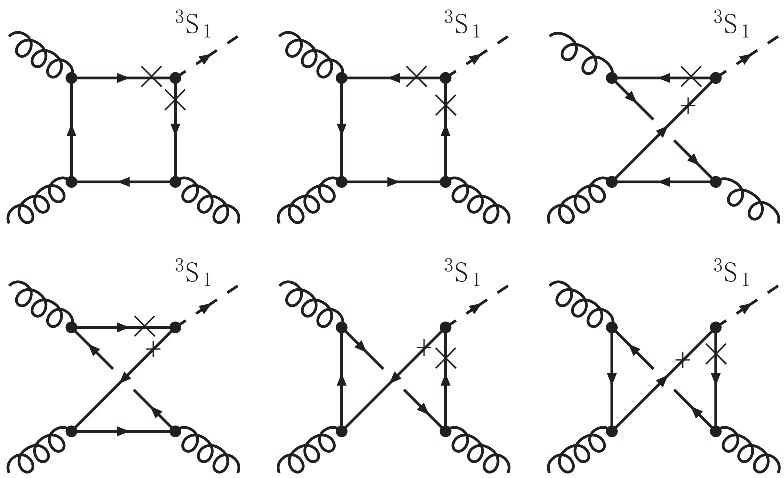

Figure 3.4: The 6 diagrams for $gg \to {}^3S_1 + g$ at LO within the CSM[10]. Spiral line stands for gluons.

The second step is that a heavy quark binds with the other one to constitute a meson ($Q\bar{Q}$). Inside of the meson, two heavy quarks should not be with a large velocity but be treated as particles at rest, namely the static approximation. The quantum numbers of these two quarks are supposed not to vary, especially the color and the spin, during the binding process and the physical states should not be of color. Because the binding process is at the level of color-single state, this model is labeled to the *Color Single Model* (*CSM*).

However, experimental results from CDF disagreed with the prediction of this LO CSM for the production cross section of prompt charmonium. The measurement from CDF is above the LO CSM curve in a large variation, about an order of magnitude. Thus, the gluon fragmentation process is proposed, that LO CSM is overpowered at large transverse momentum including the high older of α_s for both of S-wave and P-wave. Later, quark fragmentation is also considered to contribute the production of quarkonia. For instance, the direct ψ ($^3S_1$ states), for both of J/ψ and $\psi(2S)$, could be from c-quark fragmentation at large p_T ($p_T > 5\text{GeV}/c$). Two examples of the fragmentation are shown in Fig. 3.5. Another process may happen is the initiation of a sea quark during the fragmentation, which could take huge advantage at large p_T.

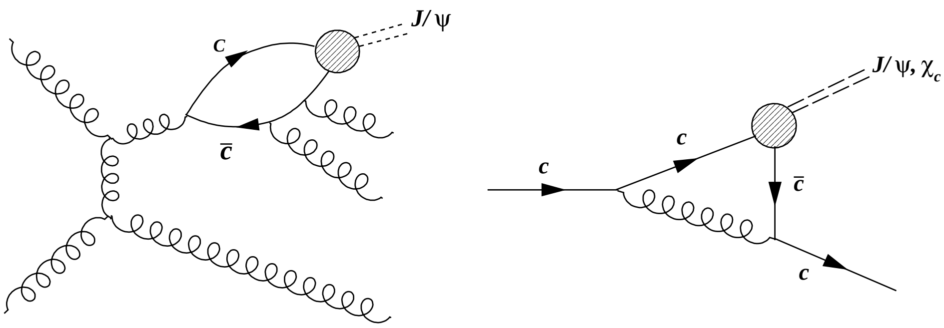

Figure 3.5: Two examples of the gluon fragmentation (left) and the quark one (right).

3.3.2.2 Color evaporation model

This model is old (since 1977), but revived in 1990s since it could partially explain CDF's result instead of CSM. Different from the CSM, this model treats all color states and spins of the asymptotic quark-antiquark pair all together and the cross section of all possible $Q\bar{Q}$, here $c\bar{c}$ as an example, perturbatively. Regardless the color, $c\bar{c}$ dynamics are determined by short distance, $\Delta x \sim m_\psi^{-1}$. Soft gluon emission is assumed during the binding process to equivalence the quantum numbers.

Then the charmonium could be produced from the invariant mass of $2m_c$ to the open flavor threshold $2m_D$ ($|D >\sim |cu > + |cd > + |cs >$). The cross section of the charmonium state could be calculated as,

$$\sigma_{onium} = \frac{1}{9} \int_{2m_c}^{2m_D} dm \frac{d\sigma_{c\bar{c}}}{dm} \tag{3.4}$$

Here $\frac{1}{9}$ stands for the statistical probability of having a color singlet state in the $3 \times \bar{3}$ charm pair asymptotically. The charmonia comes from $c\bar{c}$ entangled with each other and is assumed to a non-perturbative process in Color Evaporation Model (CEM), since the perturbative one has a very different time scale. Therefore, the cross section of a certain state, for instance a J/ψ meson, is given by,

$$\sigma_{J/\psi} = \rho_{J/\psi} \sigma_{onium} \tag{3.5}$$

where the fraction number $\rho_{J/\psi}$ is a constant, also for other states. But it depends on so many elementary factors, e.g. the central mass energy, J/ψ transverse momentum, gluon density, etc. Even the model itself cannot give the certain process, which may also effects this $\rho_{J/\psi}$. This model is used to predict the ratio of quarkonia cross sections, e.g. one should have $\sigma_{\eta_c} : \sigma_{J/\psi} = 1 : 3$ and $\sigma_{\chi_{c0}} : \sigma_{\chi_{c1}} : \sigma_{\chi_{c2}} = 1 : 3 : 5$. But the bias is found, which is between the experimental result and CEM prediction on the cross section ratio of χ_{c1} over χ_{c2}. Moreover, CEM cannot explain the different cross sections of photo-production and hadron-production.

The weakness of CEM pushed the search for more precious models. But CEM is the first model which gives the correct cross section shape in history, shown in Fig. 3.6.

3.3.3 Color octet mechanism

Facing the disagreement between theoretical predictions and experimental results, the contributions from Fock-state is considered in the P-wave charmonia production. This process goes with two gluons, one of which will fragmentate to a pair of light quark to form the hadron. This assumption turns out to be a complete the-

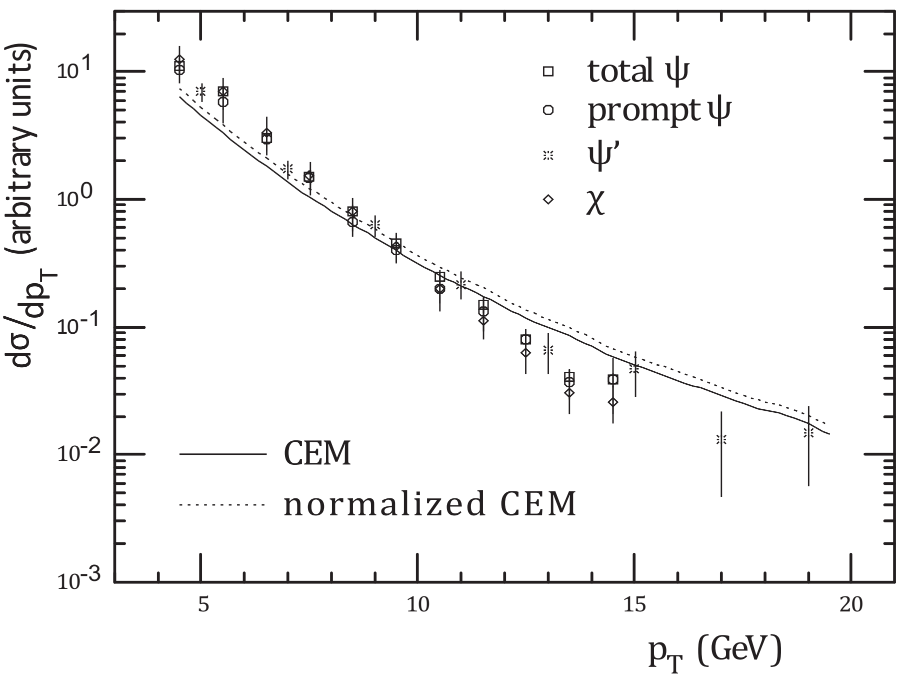

Figure 3.6: Data from CDF and prediction by CEM in an arbitrary normalization[49]. Natural units are used here.

ory, known as the non-relativistic QCD ($NRQCD$) factorization formalism. Study on this topic is still on going and it is the most sophisticated tool in the prediction of heavy quarkonia production.

This effective theory treats quarkonium production as a non-relativistic process approximately, based on a systematic expansion in both α_s and v, where v is the quark velocity in the quarkonia rest frame. For charmonia, $v_c^2 \approx 0.23$ and for bottomonia $v_b^2 \approx 0.08$. Quarkonia production is explained to two steps, that $\mathrm{Q\bar{Q}}$ pair at perturbative level first and evolution into a quarkonia state via emission of soft gluons at non-perturbative level, which means the color (as well as angular momentum, etc) could change during the process and this differs from CSM assumption. Examples are shown in Fig. 3.7. This is reasonable, that $\mathrm{Q\bar{Q}}$ pair is produced at the distance scale of $\frac{1}{m_Q}$ (m_Q is the quark's mass), whereas the typical QCD scale for bound-state is very large relatively.

The cross section of an inclusive quarkonia state could factorized to be,

$$d\sigma(H+X)=\sum_{n} d\hat{\sigma}(\mathrm{Q\bar{Q}}[n]+X)\cdot <\mathcal{O}_n^H> \tag{3.6}$$

Where the $d\hat{\sigma}$ is the cross section to produce a $\mathrm{Q\bar{Q}}$ pair in certain color and angular momentum state marked by n, and $<\mathcal{O}_n^H>$ refers to one matrix element describing that $\mathrm{Q\bar{Q}}$ pair transfers into a heavy quarkonia H, $\sum$ here stands for all possible S, L, J and the color. In case of S-wave, the $\mathrm{Q\bar{Q}}$ is specialized to $\mathrm{c\bar{c}}$, the momentum states are standard $^{2S+1}L_J$ and color states could be color-singlet ($^{(1)}S$) or color-octet ($^{(8)}S$). This is the reason that this model is named *Color Octet Mechanism* (*COM*).

The S-wave quarkonia state could be decomposition to a Coulomb gauge,

$$\begin{aligned}|\psi> \;=\;& \mathcal{O}(v^0)|\mathrm{c\bar{c}}[^3S_1^{(1)}]> +\mathcal{O}(v)|\mathrm{c\bar{c}}[^3P_J^{(8)}]g> +\mathcal{O}(v^2)|\mathrm{c\bar{c}}[^1S_0^{(8)}]g> + \\ &+\mathcal{O}(v^2)|\mathrm{c\bar{c}}[^3S_1^{(1,8)}]gg> +\mathcal{O}(v^2)|\mathrm{c\bar{c}}[^3D_J^{(1,8)}]gg> +\cdots\end{aligned} \tag{3.7}$$

Similar to CSM, at large p_T region, the fragmentation also happens in COM, in which the short distance components is not depends on the quarkonia states category. In the J/ψ and $\psi(2S)$ production, one gluon could be fragmentate into a $^3P_J^{(8)}$ with the emission of soft gluons to balance the color during this process. This is confirmed in the $\psi(2S)$ prediction. Considering the $g\rightarrow {}^3S_1^{(8)}$, two chromo-electric transitions $|\mathrm{c\bar{c}}gg>$ to $|\mathrm{c\bar{c}}>$ contributes to the matrix element $<\mathcal{O}^{\psi}[^3S_1^{(8)}]>$, scaling at $\sim m_c^3v^7$.

The matrix element in Eq. (3.6), known as long-distance matrix element (LDME), cannot be predicted by NRQCD, but these values can still be estimated in order of magnitude, that proportional to the specific power of v, expressed in a general format,

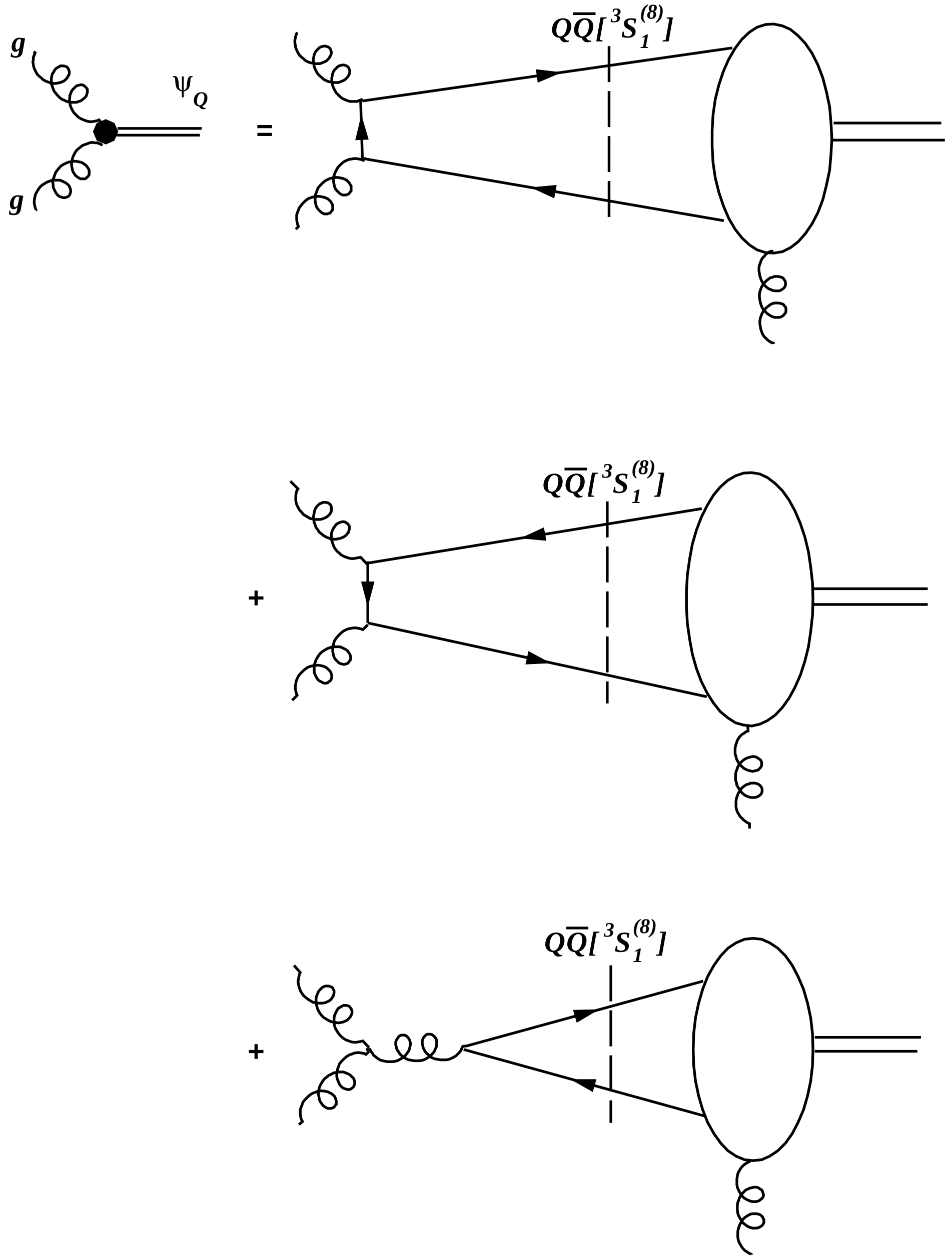

Figure 3.7: Examples of NLO pQCD in COM. In plot, the $gg \to \phi_q$ sub-processes are shown.

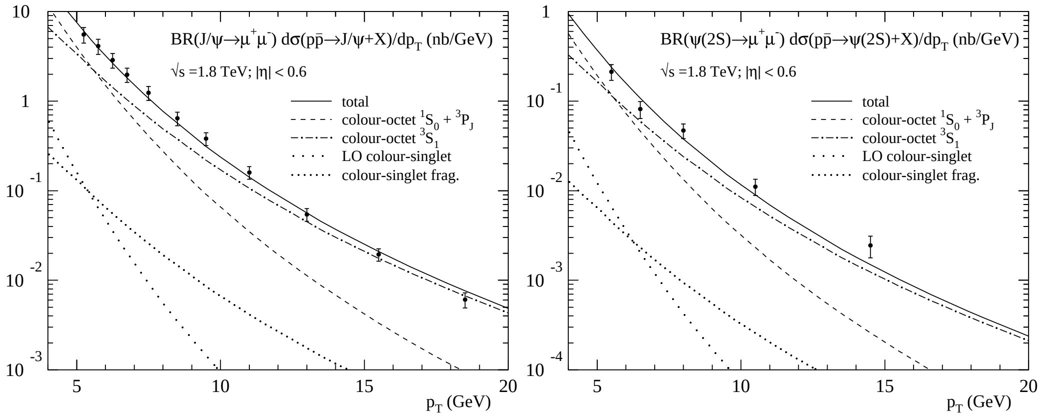

Figure 3.8: Differential cross sections for the prompt J/ψ (left) and $\psi(2S)$ (right) at Tevatron as a function of p_T. Data dots are from CDF collaboration measurement [50]. Solid curves are the NRQCD factorization fits. Natural units are used here.

$$\mathcal{O}^{c\bar{c}}[^{2S+1}L_J^{(1,8)}] \quad = \quad \chi^\dagger K \phi (a^\dagger_{c\bar{c}} a_{c\bar{c}}) \phi^\dagger K \chi \tag{3.8}$$

where χ and ϕ are Pauli spinors, and the matrix K is a product of color and spin (or their co-variant derivative ones). These factors could be attained from the NRQCD lagrangian. The color singlet LDME $< \mathcal{O}^\psi[^3S_1^{(8)}] >$ is a fixed one and the color octet LDME's, $< \mathcal{O}^\psi[^3P_J^{(8)}] >$, $< \mathcal{O}[^3S_1^{(1)}] >$ and $< \mathcal{O}^\psi[^3S_1^{(8)}] >$, are determined by fit the the measured cross section in experiment (e.g. CDF). Combining the fragmentation in the LDME, a "perfect" agreement is found between the COM and CDF data, shown in Figs. 3.8 and 3.9.

In the framework of NRQCD, There is an infinite number of LDME, since the number of Fock-state contribution is infinite that to produce a certain quarkonia. Detailed values of the LDMEs are listed in the reference[10]. Recently, some LDME of NNLO are recalculated and got a better agreement with experimental data at large transverse momentum, as shown in Fig. 3.10.

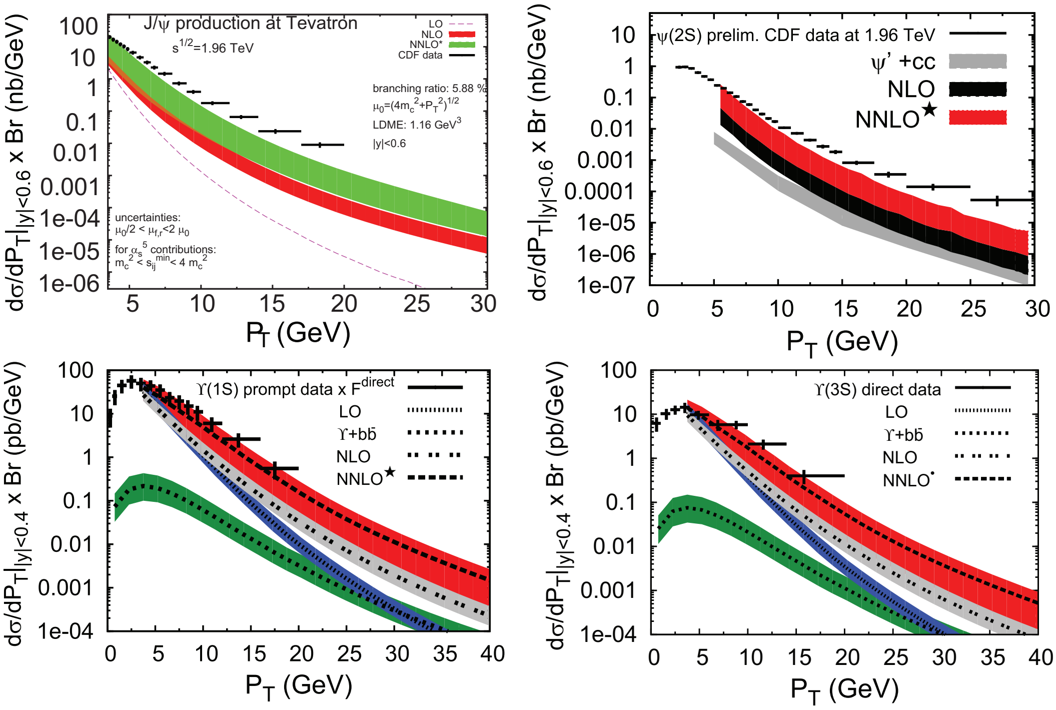

Figure 3.9: Differential cross sections for the prompt J/ψ (upper-left), $\psi(2S)$ (upper-right) , $\Upsilon(1S)$ and $\Upsilon(3S)$ at Tevatron as a function of p_T at CDF in the center mass energy of $\sqrt{s} = 1.8$ TeV, over-drawn with color octet model calculations up to NNLO[12][13]. Natural units are used here.

3.3.4 Polarization puzzle

Another inference of NRQCD is the quarkonia polarization state. First of all, the definition of one quarkonia's polarization angle θ is given by Fig. 3.11, defined as the angle between the μ^+ direction in the $\mathcal{Q}$ rest frame and the quarkonia momentum direction in the laboratory frame. This definition is known as Helicity frame (HX frame). Other angles and other frames will be mentioned later.

Each $J/\psi \to \mu^+\mu^-$ event gives one $cos\theta$ value and the normalized $cos\theta$ value distribution is affected by another polarization factor α,

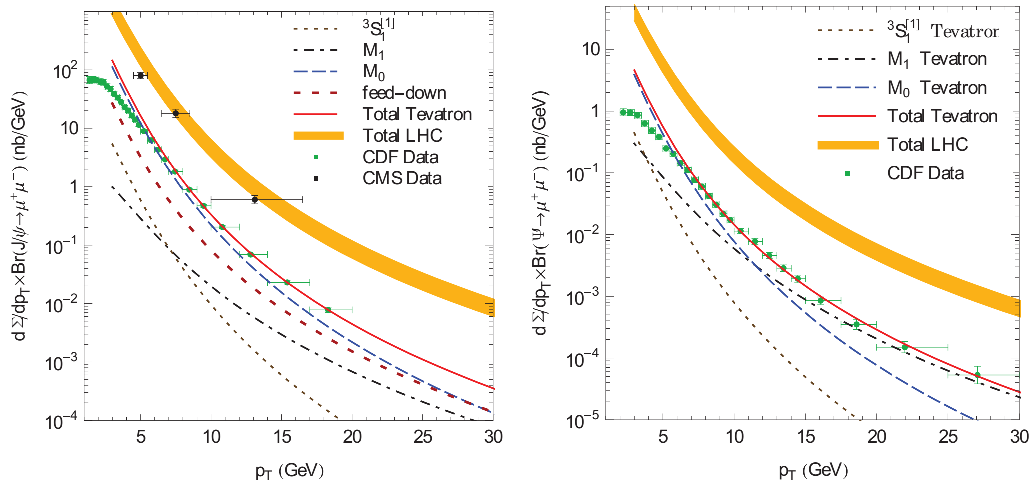

Figure 3.10: Predictions for differential cross sections for the prompt J/ψ (left) and $\psi(2S)$ (right) by the new fit NNLO LDME at Tevatron and LHC energy scale, superimposed with experimental results from CDF and CMS[51].

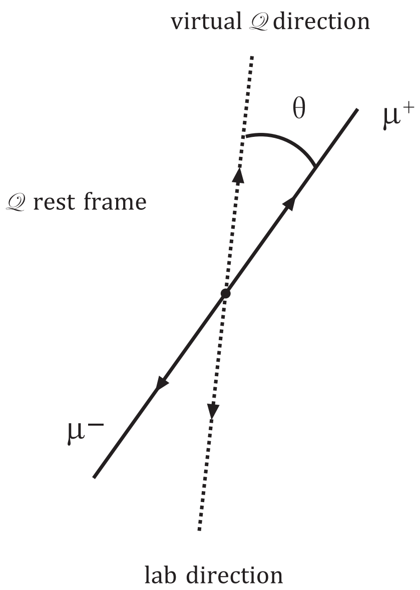

Figure 3.11: Definition of quarkonia $\mathcal{Q}$'s polarization angle θ.

$$\frac{dN}{d(cos\theta)} = \frac{3}{2(\alpha+3)}(1+\alpha cos^2\theta) \quad (3.9)$$

$$\alpha = \frac{\frac{1}{2}\sigma_T - \sigma_L}{\frac{1}{2}\sigma_T + \sigma_L} \quad (3.10)$$

Thus, $\alpha = +1$ refers to the meson being fully transverse polarized, $\alpha = -1$ for the meson being fully longitudinal polarized and $\alpha = 0$ indicates an unpolarized sample.

Non-prompt J/ψ polarization is measured to be $\alpha = -0.409$ in Helicity frame[60]. The polarization measurement on prompt heavy quarkonium gives an unexpected picture, shown in Fig. 3.12. The $\psi(2S)$ by gluon fragmentation through the color octet state should have 100% transverse polarization by the NRQCD prediction. Contrast to the prediction of NRQCD, that the parton's initial momentum is assumed to be as low as only several percent of colliding hadron, k_T factorization approach does not ignore this initial momenta.

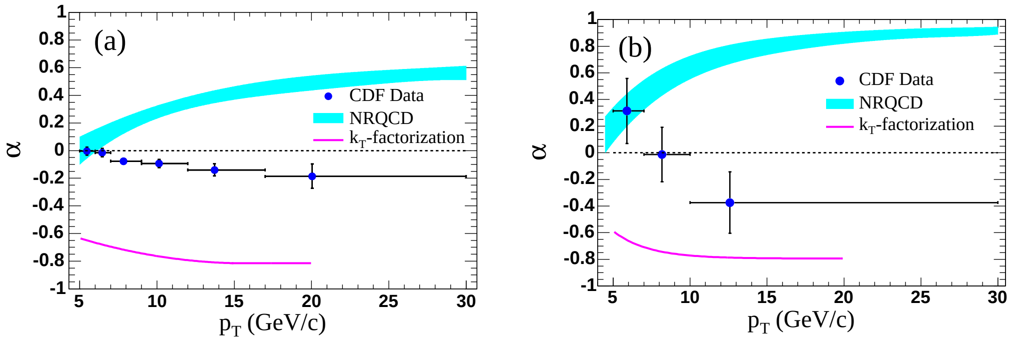

Figure 3.12: The measured polarizations of prompt J/ψ (left) and prompt $\psi(2S)$ (right), superimposed a band stands for the prediction from NRQCD and a line near the bottom infers to the k_T factorization. [15]

Another potential explanation to the paradox between NRQCD prediction and experimental results is redefinition on the polarization angle in a "vertical" frame, shown in Fig. 3.13. In the Helicity frame, the polar axis coincides with the heavy quarkonia momenta direction in the c.m. frame of the colliding hadrons, while the Collins-Soper (CS) frame requires the polar axis reflect the direction of the relative velocity of the colliding beams. Then the polarization angle implies both of the polar angle (θ) and the azimuthal angle (φ).

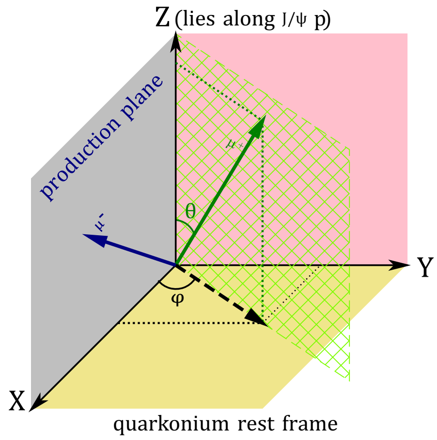

Figure 3.13: Definition of the polar (θ) and the azimuthal (φ) angles.

$$\frac{dN}{d(cos\theta)d\varphi} \propto 1 + \alpha_{\theta} cos^2\theta + \alpha_{\theta\varphi} sin2\theta cos\varphi + \alpha_{\phi} sin^2\theta cos2\varphi \tag{3.11}$$

Once the known result from Helicity frame transformed to the Collins-Soper frame, a consistent distribution tendency is achieved, covering different experiments in several energy scales, shown in Fig. 3.14. So the polar and azimuthal angle (θ and φ) in both HX frame and CS frame may lead to the right direction in the polarization measurement.

3.4 Summary

Under the SM framework, QED and QCD describe the particles and their interactions. The strong interaction with *color* could be modularized to perturbative QCD at large transfer energy scale and factorization at middle scale. Different

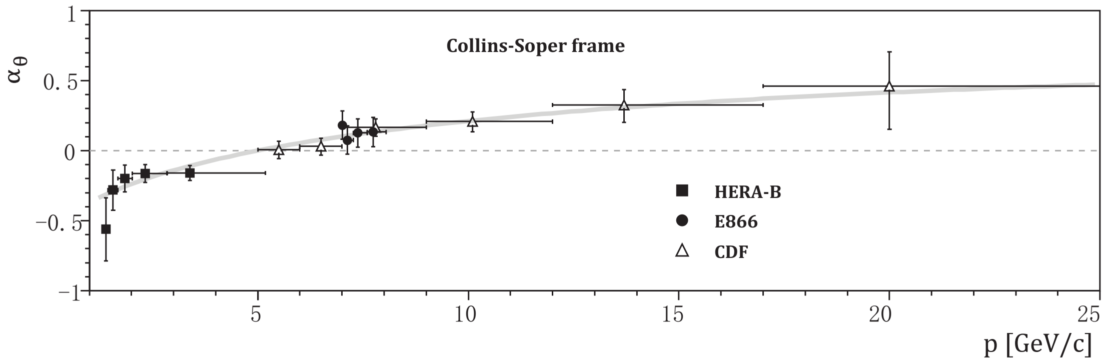

Figure 3.14: α_θ as a function of momenta, from different experiments (E866, HERA-B and CDF)[16].

models in the heavy quarkonia cross section prediction inherit the QCD theory and the COM is the one close to the experimental result most. But the polarization puzzle cannot be understood well and research on this topic is still on going.

The newly built LHC provides a good opportunity to test the cross section and polarization of heavy quarkonia, especially at large transverse momenta. This thesis focuses on the J/ψ production cross section in CMS detector at LHC.

Chapter 4

Muon and J/ψ reconstruction in CMS

In the $J/\psi \to \mu^+\mu^-$ decay, muon is the final particle produced. This section explains the reconstruction of muon and J/ψ online (HLT) and offline. For muon, the segments measurement, muon identification, muon isolation and muon trigger are discussed. The muon reconstruction system uses the information collected from muon chambers and silicon tracker. Also some calorimeter information is used for the muon isolation. Besides the good muon quality, the J/ψ reconstruction and identification also depend on the vertex resolution. In the event passed high lever trigger, two muons with opposite charges are combined to form a J/ψ candidate in the mass region from $2.6GeV/c^2$ to $3.5GeV/c^2$. The vertex fitted with $\chi^2 > 0.1\%$ is constrained.

4.1 Muon

Muon is reconstructed in CMS at different levels. From local muon reconstruction, standalone muon is fitted from muon segments and hits in muon chambers, while tracker muon is a sub-set of tracks matched to muon segments. Combined with inner tracker tracks and stand-alone muon tracks, global muon track is fitted further. Also calorimeter-based muon (CaloMuon) is a sub-set of inner tracks compatible with calorimeter hits.

4.1.1 Standalone and global muon reconstruction

The standalone/Level-2 muon is reconstructed at muon chambers and the silicon tracker is not used. This reconstruction is seeded from the innermost muon chambers. The 2D track segment is found in Layer-0, including its track position, momentum and direction associated. From inside outwards, hits from one layer to another in muon chambers are fitted to a 3D muon trajectory via Kalman-filter technique. However, in the CSC endcap chambers, because of the inhomogeneous magnetic field, the segment is reconstructed as a 3D hit. The χ^2 is chosen to reject the bad hits along the trajectory. The bad hits mainly come from the showering, delta rays and pair production. The filter searches next station of muon detector, if no hit is matched in this layer. RPC is also included for optimization of low quality muons, e.g. low momentum muons and the muons leaked from the gap between DT sectors and the wheels. The procedure is finished at the outermost layer of muon system. A backward Kalman filter will re-fit all the hits and every kinematic parameter of this trajectory uses the values measured at the innermost layer. After the suppression of the fake track, the muon system extrapolates one muon candidate track to the nominal interaction point.

Before the operating of LHC, the performance of CMS muon system is simulated by Monte Carlo and tested with cosmic ray and test beam, and the result is shown in Fig. 2.14 at Section 2.3.3.

Global muons contain the information from both of muon chambers and inner tracker. Trajectories from the standalone/Level-2 muon segments are extrapolated to the silicon tracker (strip and pixel detectors). The GEANE package is used for the estimation on the muon energy loss in the detector material and the multiple scattering. The region of interest in tracker is determined from the track parameters and the uncertainties by the extrapolated muon trajectory. Inside the region of interest, regional seeds formed by 2 hits in different tracker layers is the initial candidates for the muon trajectory. A Kalman-filter is applied to these regional seeds, which combines all compatible pixels and double-side silicon strip hits to get high efficiency, and the final muon candidates are selected by passing a χ^2 cut. Thus, global muons are reconstructed.

4.1.2 Muon reconstruction performance

The performance of muon reconstruction in idea detector, e.g. reconstruction efficiency and transverse momentum resolution, given by MC simulation and published on technical design report[38], are shown in Figs. 4.1 and 4.2.

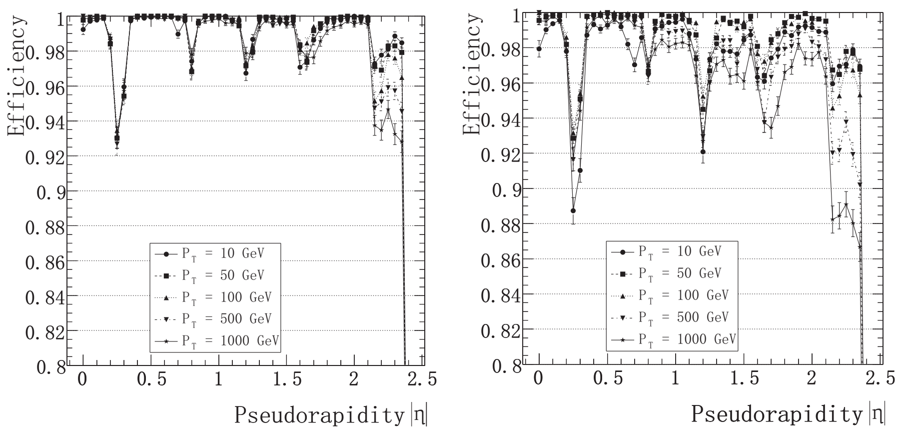

Figure 4.1: The standalone (left) and global (right) muon reconstruction efficiencies as a function of muon pseudorapidity for various transverse momentum from MC simulation.[38] Natural units are used here.

Generally, muon reconstruction efficiency, defined as the probability of muons at generator level that can be reconstructed successfully, is at 95% $\sim$ 99% level. The drop of the efficiency distribution around $|\eta| = 0.25$ and $|\eta| = 0.8$ is due to the non-existence of DT chambers between two DT wheels. At $|\eta| = 1.2$ is the transition region from DT to CSC systems and around $|\eta| = 1.7$ are the gaps in the CSC systems.

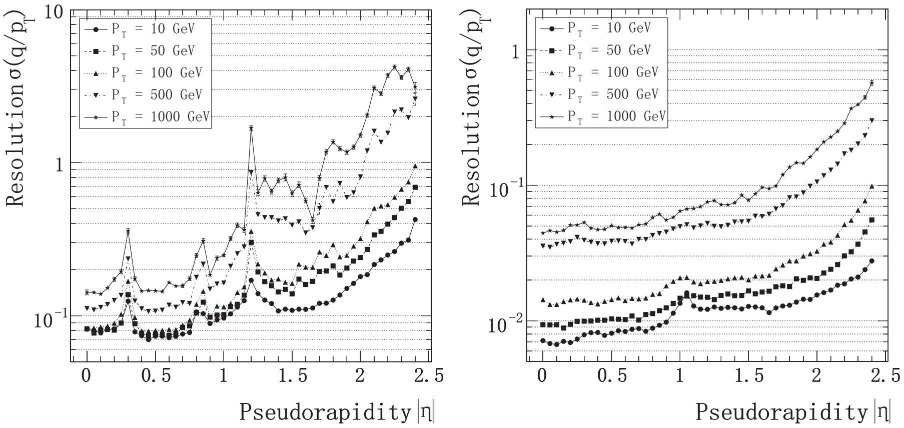

Figure 4.2: The standalone (left) and global (right) muon transverse momentum resolution as a function of muon pseudorapidity for various transverse momentum from MC simulation.[38] Natural units are used here.

The resolution on muon transverse momentum is achieved by a Gaussian fit to the spectrum of this value,

$$\frac{q^{rec}/p_T^{rec} - q^{gen}/p_T^{gen}}{q^{gen}/p_T^{gen}} \tag{4.1}$$

where q is the charge of the particle, here $q_{muon} = 1$; p_T^{gen} and p_T^{rec} are the transverse momentum at the generator and reconstruction levels respectively. The silicon tracker information, added in the global muon reconstruction, offers 10 times more precise resolution than the segments in muon chambers only.

4.1.2.1 Muon efficiency measurement

From the latest MC simulation and the real experiment data of $J/\psi \to \mu^+\mu^-$ sample, the muon reconstruction and trigger efficiency could be measured in two methods, i.e. the MC matching method and the data-driven one (namely Tag-and-Probe method, TnP for short). Here only the global and tracker muon are presented for the $J/\psi \to \mu^+\mu^-$ cross section measurement.

As explained before, the global muon could also be tracker muon, since they are from two different reconstruction algorithms. Global muon has a higher confidence level while the tracker muon could access lower (transverse) momentum, distributed in Figs. 4.3 and 4.4. To avoid the overlap between these two kinds of reconstructed muons, one muon reconstructed as a global muon will not count into tracker muon, i.e. these two reconstruction methods are exclusive.

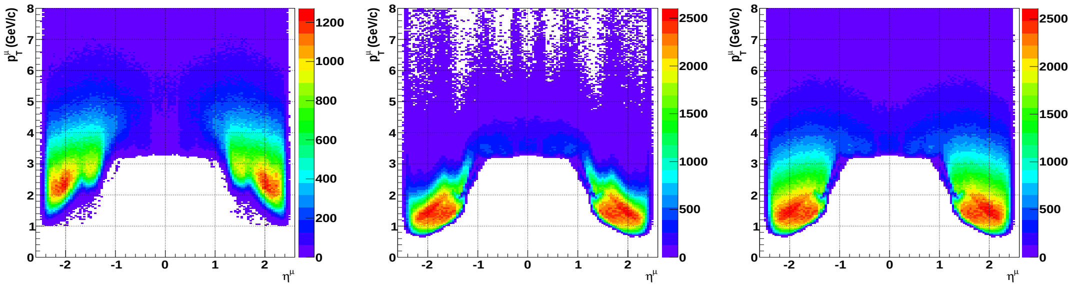

Figure 4.3: global muon (left), tracker muon (middle) and sum of the two (right) 2D distribution as a function of muon pseudorapidity and transverse momentum in $J/\psi \to \mu^+\mu^-$ sample from MC simulation.

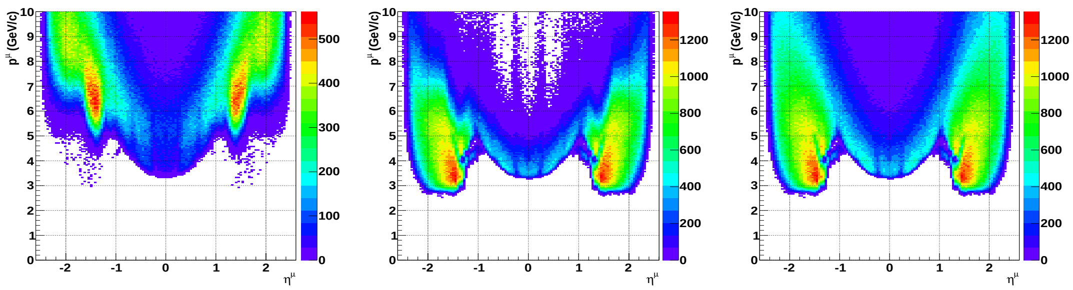

Figure 4.4: global muon (left), tracker muon (middle) and sum of the two (right) 2D distribution as a function of muon pseudorapidity and momentum in $J/\psi \to \mu^+\mu^-$ sample from MC simulation.

The MC match efficiency The number of reconstructed muon divided by the one of generated muon is the efficiency from Monte Carlo simulation. Furthermore, the muon quality based on the detector information is determined on, e.g. the number of hits in tracker (> 12), the distance of the muon track to the primary vertex and the beam line ($d_0 < 3cm, d_z < 30cm$), a χ^2 per degree of freedom < 4 for tracker track, etc. Global muon should also satisfy additional requirements, i.e. at least one pixel hit, a χ^2 per degree of freedom < 4 for global track and muon identifications of "*TrackerMuonArbitrated*"[1] and "*TMLastStationAngTight*"[2].

Here, the reconstructed muon, both of global and tracker muons, matching with the muons at generator level is defined as this muon is in a spatial angle near one generated muon ($\Delta R = \sqrt{(\Delta\eta)^2 + (\Delta\phi)^2} < 0.04$, ϕ in radian) and also its transverse momentum is not far from that of a generated muon ($\Delta p_T/p_T < 0.2$). The angular distance and relative transverse momentum difference of reconstructed muon and its partner at generator level are shown in Figs. 4.5, 4.6 and 4.7.

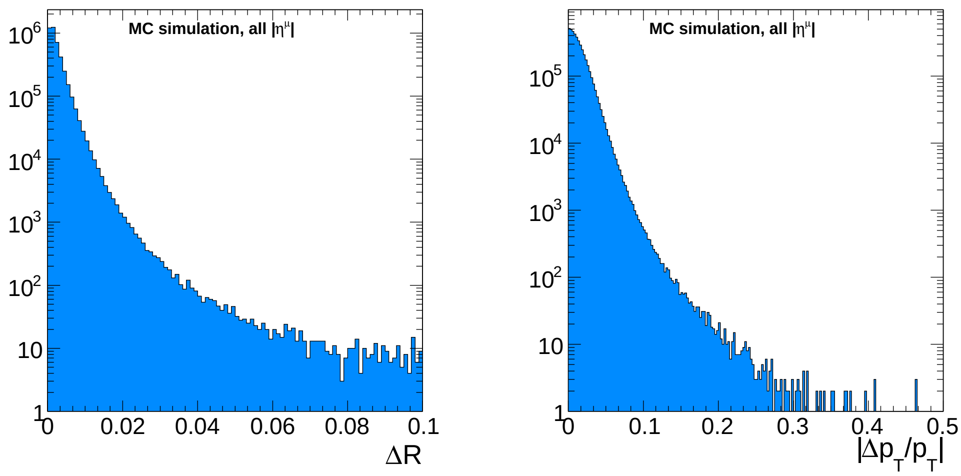

Figure 4.5: Distribution of spatial angle ΔR (left) and relative difference of transverse momentum (right) between reconstructed muon and its generated partner in all η^μ regions, ΔR cut added.

The MC matched muon efficiency is calculated as,

$$\varepsilon^\mu(p_T^\mu, \eta^\mu) = \frac{N^{match}(p_T^\mu, \eta^\mu)}{N^{gen}(p_T^\mu, \eta^\mu)} \tag{4.2}$$

[1] resolve ambiguity of sharing segments;

[2] penetration depth tight selector with additional angular cuts;

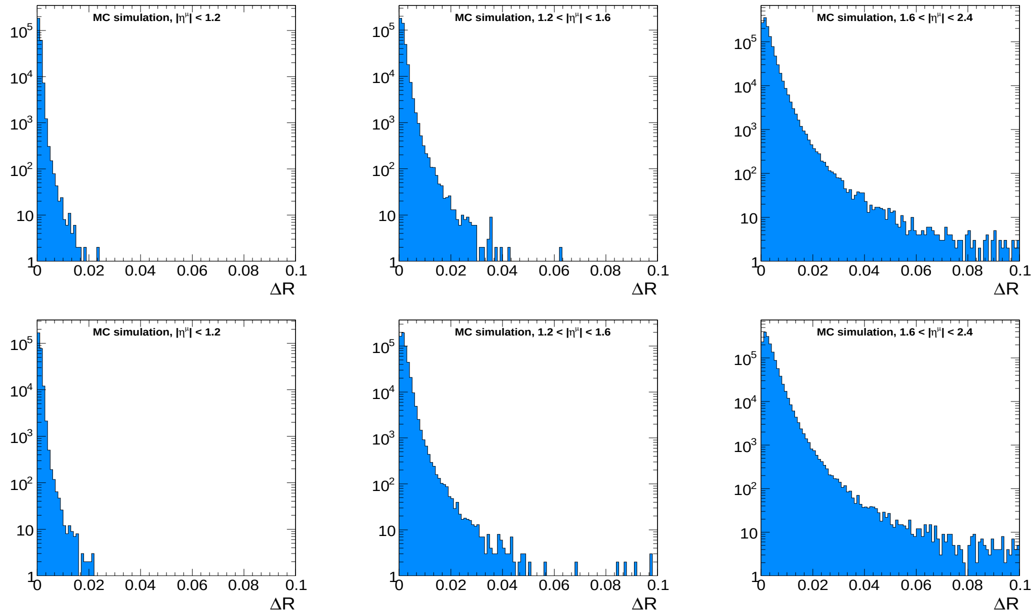

Figure 4.6: ΔR of global (upper) and tracker muon (bottom) in CMS barrel (left), transition (middle) and endcaps (right) regions.

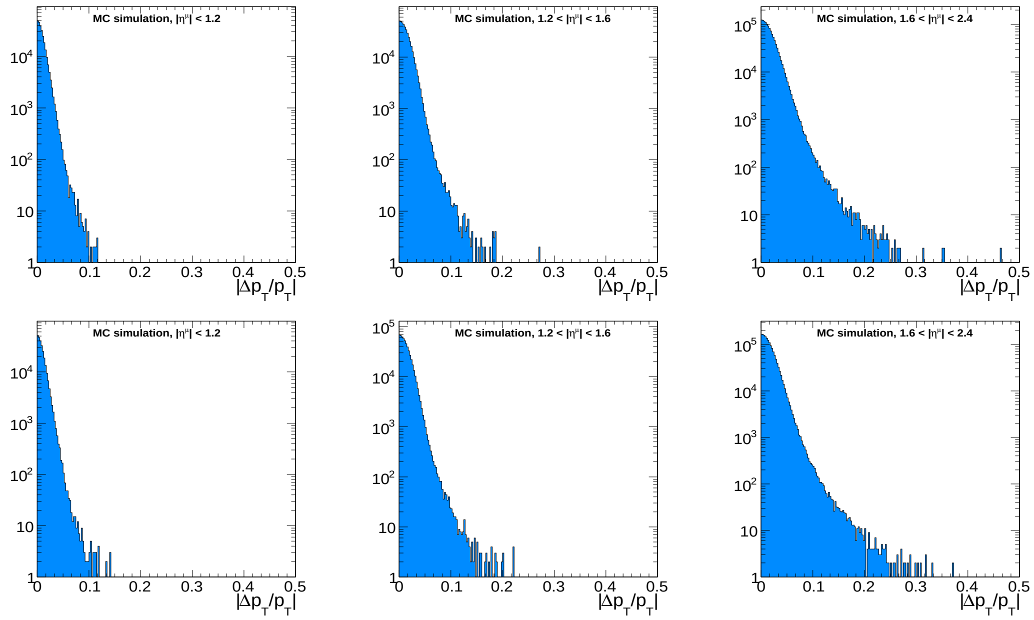

Figure 4.7: $\Delta p_T/p_T$ of global (upper) and tracker muon (bottom) in CMS barrel (left), transition (middle) and endcaps (right) regions, ΔR cut added.

where, N^{match} is the number of muons at generator level which match good quality partners at reconstructed level and N^{gen} is the number of generated muons in one bin. Similarly, the efficiency is defined as a function of p^{μ} and η^{μ} for both of global and tracker muons. The 2D efficiency maps are shown in Fig. 4.8.

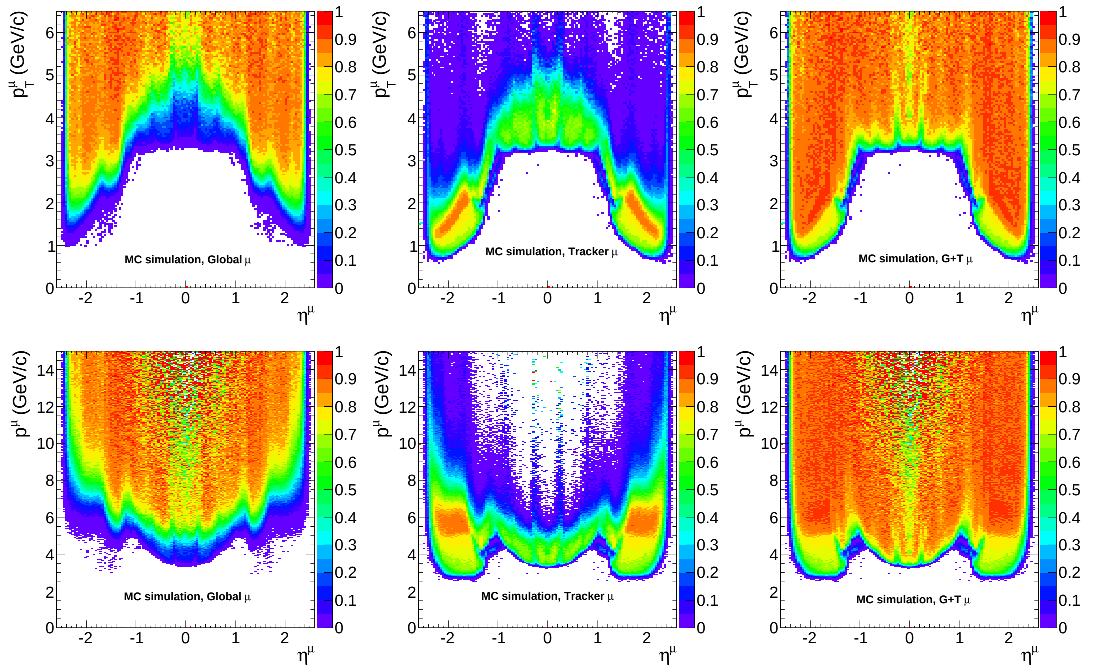

Figure 4.8: Reconstruction efficiency 2D distributions of single global (right), tracker (middle) muon and sum of the two (right), as a function of p_T^{muon} (upper) and p^{muon} (bottom) plus muon pseudorapidity by $J/\psi \to \mu^+\mu^-$ sample from MC simulation.

The muons are reconstructed well in CMS, especially for the high (transverse) momentum $p_T^{\mu} > 3.5GeV/c$ at barrel and $p^{\mu} > 5GeV/c$ at endcap. Also the one dimension single muon offline reconstruction efficiencies are shown in Fig. 4.9, as a function of transverse momentum. At high p_T, the efficiency drop is due that the *TMLastStationAngTight* selector is known to be inefficient at high p_T. Firstly, this selector requires the track and the segment match within three sigma and the sigma tends to be smaller with p_T increases. Secondly, above a certain p_T the selector requires two stations[3] instead of one, so it becomes less efficient. *TMLastStationAngTight* was not meant to be used at high p_T and other ways of selecting muons could achieve better efficiency and good purity (e.g. just taking global muons or muons passing some certain cuts). With the development of muon calibration, this could be improved.

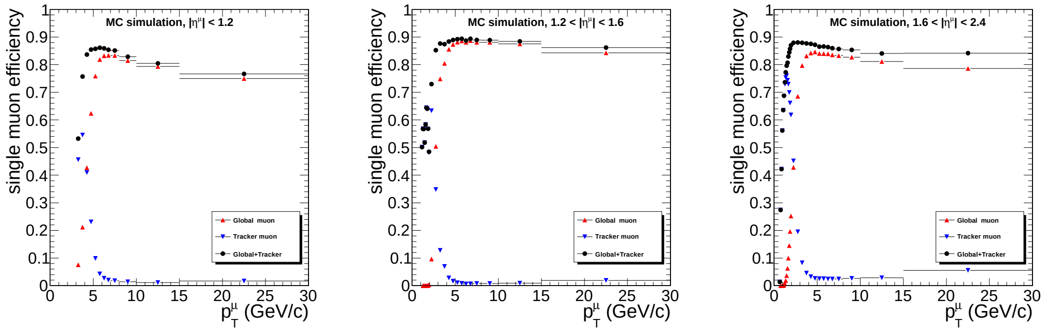

Figure 4.9: Reconstruction efficiency 1D distribution of single global, tracker muon and sum of the two as a function of p_T^μ in different pseudorapidity bins by $J/\psi \to \mu^+\mu^-$ sample from MC simulation.

Also the muon reconstruction efficiency as a function of muon pseudorapidity could be simulated, as shown in Fig. 4.10.

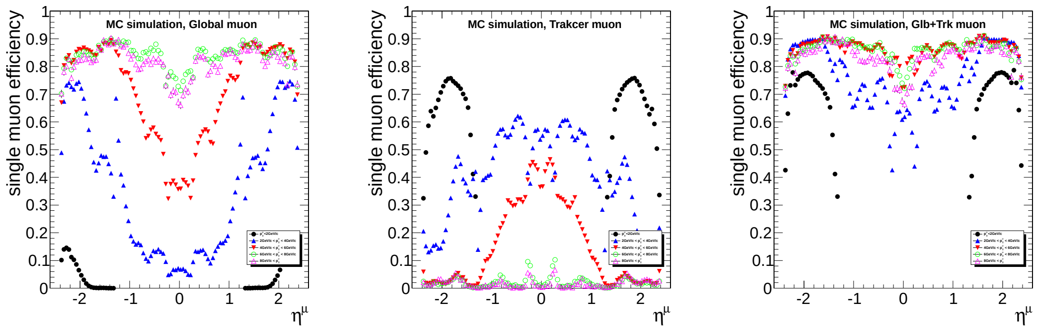

Figure 4.10: Reconstruction efficiency distribution of single global (left), tracker (middle) muon and sum of the two (right) as a function of η^μ by $J/\psi \to \mu^+\mu^-$ sample from MC simulation.

[3]One station is one layer of CSC muon chamber, see Section 2.3.3.

Another single muon identification efficiency (muon id efficiency) is defined as the probability of a muon track reconstructed as a global/tracker muon. This concept is one part of the Tag-and-Probe (TnP) methodology. Similar to the direct global/tracker muon over MC muon method, this muon id efficiency could be calculated as shown in Fig. 4.11.

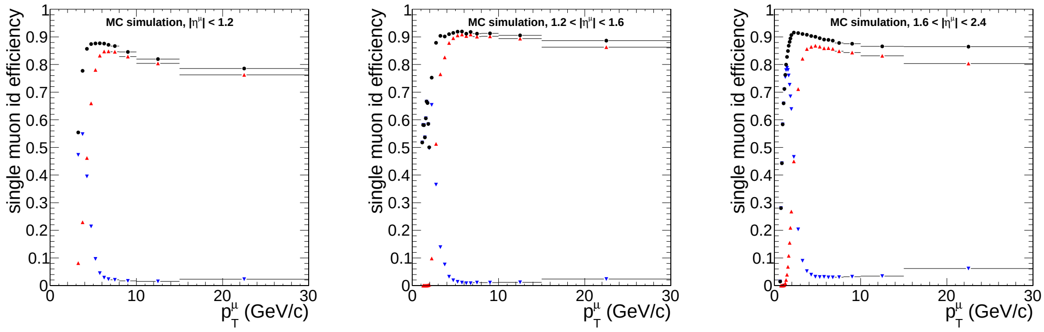

Figure 4.11: Muon identification efficiency distributions of single global, tracker muon and sum of the two as a function of p_T^{muon} in different pseudorapidity bins by $J/\psi \to \mu^+\mu^-$ sample from MC simulation.

Tag-and-Probe methodology The single muon efficiency, also the trigger efficiency, cannot be extracted from experimental data directly, because of lacking of the generator level information. But they could be measured by the Tag-and-Probe (TnP) methodology. TnP uses a known mass peak (e.g. the J/ψ, Υ, Z, etc.) to select the tag particle and to estimate the possibility of finding a probe particle; these two particles could form a reasonable mass spectrum. In this study, the known mass resonance is the J/ψ and the tag particle is one well reconstructed muon and passed the certain trigger. It assumes that each generated muon could leave a track in tracker system in the pseudorapidity region of $|\eta| < 2.4$. The probe candidate is a tracker track that we trust it as a muon trajectory and passing probe is the track satisfied all criteria that is really a reconstructed muon. The muon identity and trigger efficiency equals to the ratio of the passing probe over probe candidate approximately.

This process could be formulized as Following. First of all, the tag muon and probe particle will form a J/ψ candidate within mass range from 2.6 to 3.5 GeV/c^2 ($m = \sqrt{p_{tag}^2 + p_{probe}^2}$). All muons/tracks are categorized into three types, that tag muon (T), passing probe muon (P) and failing probe muon (F), as shown in Table 4.1. So the total probe is the sum of the passing probe muon and the failing probe muon. Thus, six different combinations of the tags and probes are TT/TP/TF/PP/PF/FF.

Table 4.1: The definition of muons in Tag-and-Probe method.

tag muon(T)	a muon passes tag selection criteria
passing probe muon(P)	a muon (not of tag quality) passes the selection cuts, whose efficiency is being measured
failing probe muon(F)	the rest of the probe muon candidates who fail to pass the selection criteria

Theoretically, the efficiencies of three different tag and probe muons are labeled as ρ_T, ρ_P and ρ_F. Then $\rho_T + \rho_P + \rho_T = 1$ (a muon track will be always one of the three categories.) and the muon reconstruction efficiency is $\epsilon_{event} = \rho_T + \rho_P$. Event by event, the muon efficiency is re-written as[56],

$$\epsilon_{event} = \frac{2N_{TT} + 2N_{TP} + 2N_{PP} + N_{TF} + N_{PF}}{2N_{TT} + 2N_{TP} + 2N_{PP} + 2N_{TF} + 2N_{PF} + 2N_{FF}} \tag{4.3}$$

Here the factor 2 before some combinations is because that there are two muons in one J/ψ event and they act the tag and probe muons alternatively. When the statistic is high and in a sufficiently large sample,

$$\lim_{N\to\infty} \epsilon_{event} = \frac{2\rho_T^2 + 2\rho_P^2 + 4\rho_T\rho_P + 2\rho_T\rho_F + 2\rho_P\rho_F}{2\rho_T^2 + 2\rho_P^2 + 2\rho_F^2 + 4\rho_T\rho_P + 4\rho_T\rho_F + 4\rho_P\rho_F} = \rho_T + \rho_P \tag{4.4}$$

There could be a lot of approximate ways to calculate the $\rho_T+\rho_P$ and one easy example to lead the same result is,

$$\lim_{N\to\infty}\epsilon_{event}=\lim_{N\to\infty}\frac{2N_{TT}+N_{TP}}{2N_{TT}+N_{TP}+N_{TF}}=\frac{2\rho_T^2+2\rho_T\rho_P}{2\rho_T^2+2\rho_T\rho_P+2\rho_T\rho_F}=\rho_T+\rho_P \quad (4.5)$$

here the numerator of the fraction indicates the events with one tag muon and a passing probe muon, while the denominator corresponds to the events with one tag muon and the other could be any muon. The number of events are extracted by fitting the mass spectrum .

4.1.2.2 Muon reconstruction resolution

As explained in Section 4.1.2, the relative difference between the muon at generator level and reconstruction level (L3 level) is the resolution, i.e.

$$\frac{q^{rec}/p_T^{rec}-q^{gen}/p_T^{gen}}{q^{gen}/p_T^{gen}}, \quad (4.6)$$

where q is the charge of the particle, here $q_{muon}=1$; p_T^{gen} and p_T^{rec} are respectively the transverse momentum at the generator and reconstruction levels. In a certain bin, resolution on muon transverse momentum of many events could form a Gaussian-like peak. The mean value and RMS (Root Mean Square, here it equals the variance $sigma$.) could be calculated by fitting, as shown in Fig. 4.12.

Thus, the muon transverse momentum resolution as a function of muon pseudorapidity in different transverse momentum is extracted from fitting the resolution peak in consecutive p_T^μ and η^μ bins, as shown in Fig. 5.2. The resolution smears not very much at the low pseudorapidity but does a lot at high η region. In the calibration study, the J/ψ peak from experimental data is fitted by different muon p_T discretion function and get similar result[59], that will be discussed in details in Section 5.1.

Similarly from MC simulation, the η^μ resolution is defined as $\eta^{gen}-\eta^{rec}$, also the ϕ^μ resolution, as shown in Fig. 4.14.

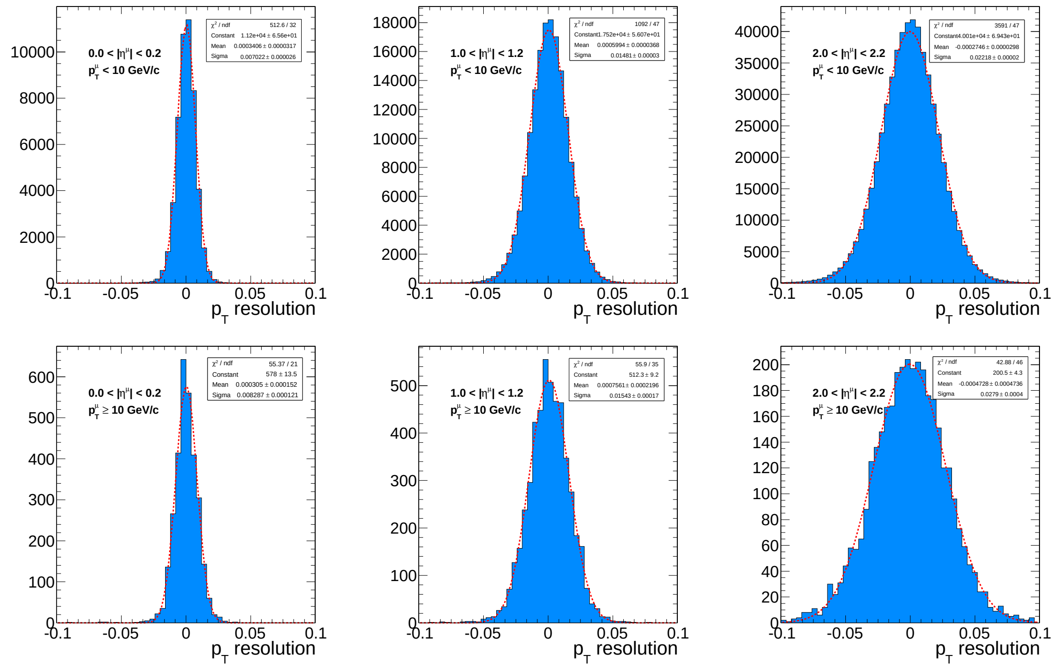

Figure 4.12: Muon transverse momentum resolution distributions in different p_T^μ and η^μ bins, fit by Gaussian functions.

4.2 J/ψ

J/ψ event collected in CMS depends on the single muon reconstruction and trigger performance. As discussed before, the single muon could be reconstructed well in CMS and tracker muon optimizes muon statistic a lot, particularly in low p_T^μ range. Trigger will be discussed in next chapter.

4.2.1 J/ψ reconstruction

The $J/\psi \to \mu\mu$ events are selected by requiring every two muons in one event with opposite charges and their invariant mass in between 2.797 and 3.397 GeV/c^2 ($mass^{J/\psi} \pm 6 \cdot \sigma$). Each muon pair should also pass a common vertex fit only if the fit χ^2 probability less than 0.1%. Based on different muon types (global muon or tracker muon), J/ψ is classified into three categories that the global-global, the global-trackerand the tracker-tracker muon pair. To reduce the effect of multiple

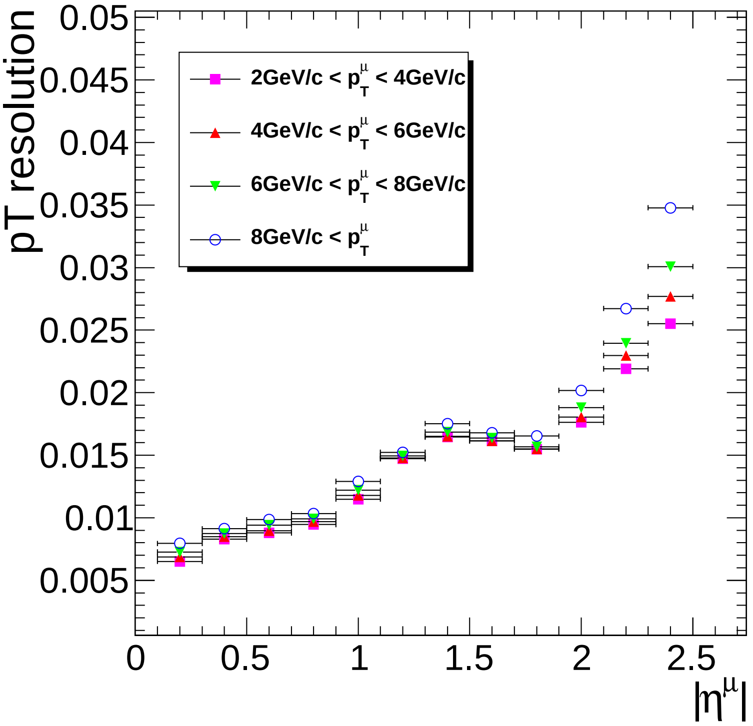

Figure 4.13: Muon transverse momentum resolution as a function of η^{μ} in different p_T^{μ}.

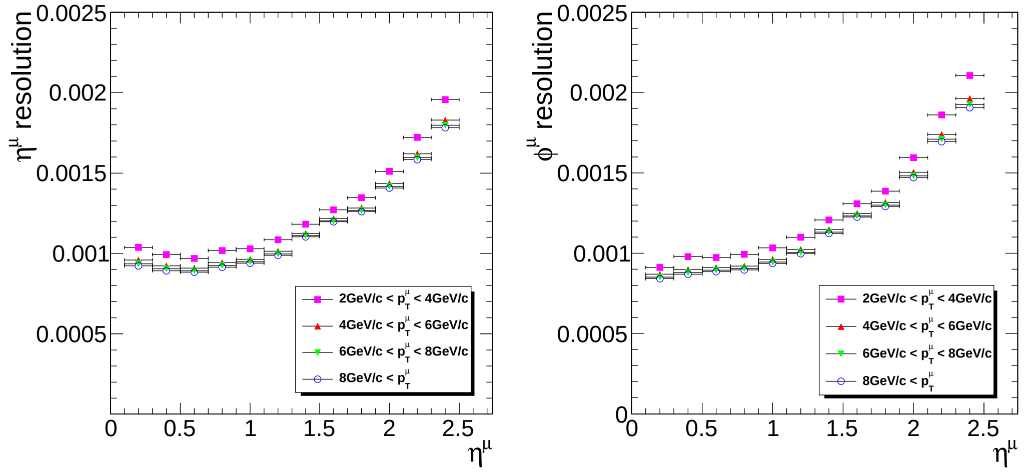

Figure 4.14: Muon pseudorapidity (left) and azimuthal angle in radians (right) resolution as a function of η^{μ} in different p_T^{μ}.

combination, only the pure muon pair (global muon has higher quality than the tracker one) is picked up and rest of them are dropped. If two or more muon pair candidates have the same type of combination, the one with the largest transverse momentum is selected. On average, there are 1.07 J/ψ combinations in each event at this early LHC running period.

The three different types of muon pair are distributed in Fig. 4.15, as functions of transverse momentum ($p_T^{J/\psi}$) and rapidity ($y^{J/\psi}$). Also the reconstruction efficiency is shown in Fig. 4.16. The tracker muon enlarges the statistic of reconstructed J/ψ and the $p_T^{J/\psi}$ could extend to 0. In this thesis, all reconstructed J/ψ are sum of these three combinations.

4.2.2 J/ψ mass peak

Two muons from J/ψ or other sources, e.g. QCD process, could be distinguished clearly in CMS, even at very early stage of LHC run, as shown in Fig. 4.17. J/ψ, $\psi(2S)$, $\Upsilon(nS)$ and Z peaks can be seen respectively.

Zoomed into the J/ψ mass region, the trigger and vertex filter will help to suppress QCD background strongly and a relatively clean J/ψ source will be selected, as shown in Fig. 4.18. Here prompt/nonprompt J/ψ and QCD dimuon events from MC simulation are included to show their ratios and distributions in mass spectrum. All quantities used are from MC Pythia production and CMSSW full simulation, e.g. the number of reconstructed events, pre-selection filter acceptance, cross section of each component source, etc. Since the J/ψ cross section from MC Pythia generator is not reliable, even in theory this cannot be understand very well, the MC simulated data shown in Fig. 4.18 may not match the experimental results.

In different transverse momentum and rapidity bins, the mean value and the resolution of the J/ψ resonance could be extracted by fitting the mass peak. Some examples are shown in Fig. 4.19. The mean values and resolutions are also summarized and ploted in Fig. 4.20. The mean value of the J/ψ peak is the average of Gaussian function and the resolution (r) is the combined RMS of these two compo-

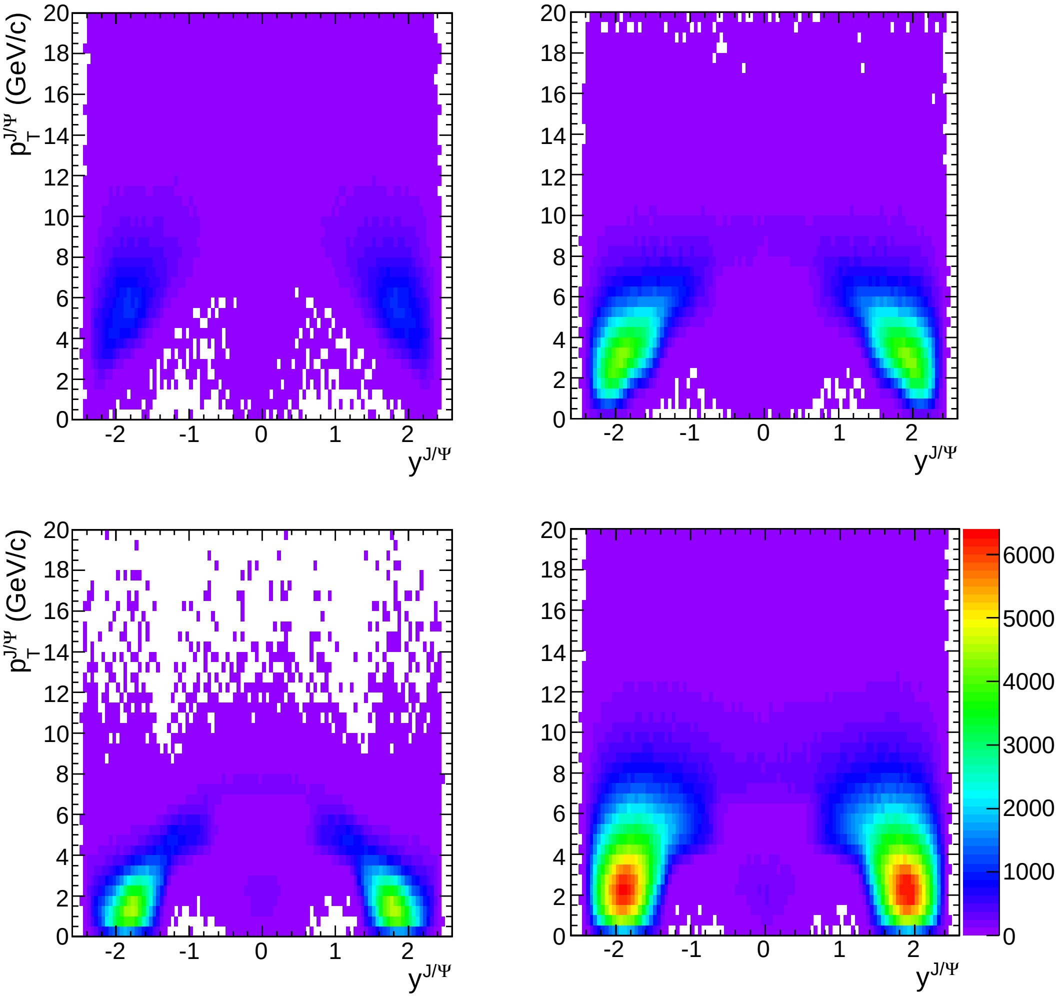

Figure 4.15: The distribution of global-global (left-upper), global-tracker (right-upper), tracker-tracker (left-bottom) and sum of the three (right-bottom) J/ψ reconstructed as a function of $p_T^{J/\psi}$-$y^{J/\psi}$ from MC simulated $J/\psi \to \mu\mu$ sample. The tracker muon broadens the reconstructed J/ψ from $6GeV/c$ ($3GeV/c$) at the barrel (endcap) part to nearly 0. The statistic at low $p_T^{J/\psi}$ in the endcap increases over five times, where the cross section could be measured in finer bins at these regions. For the barrel part, there are still not sufficient events at low $p_T^{J/\psi}$ and the cross section will measured from a certain $p_T^{J/\psi}$ but not from 0.

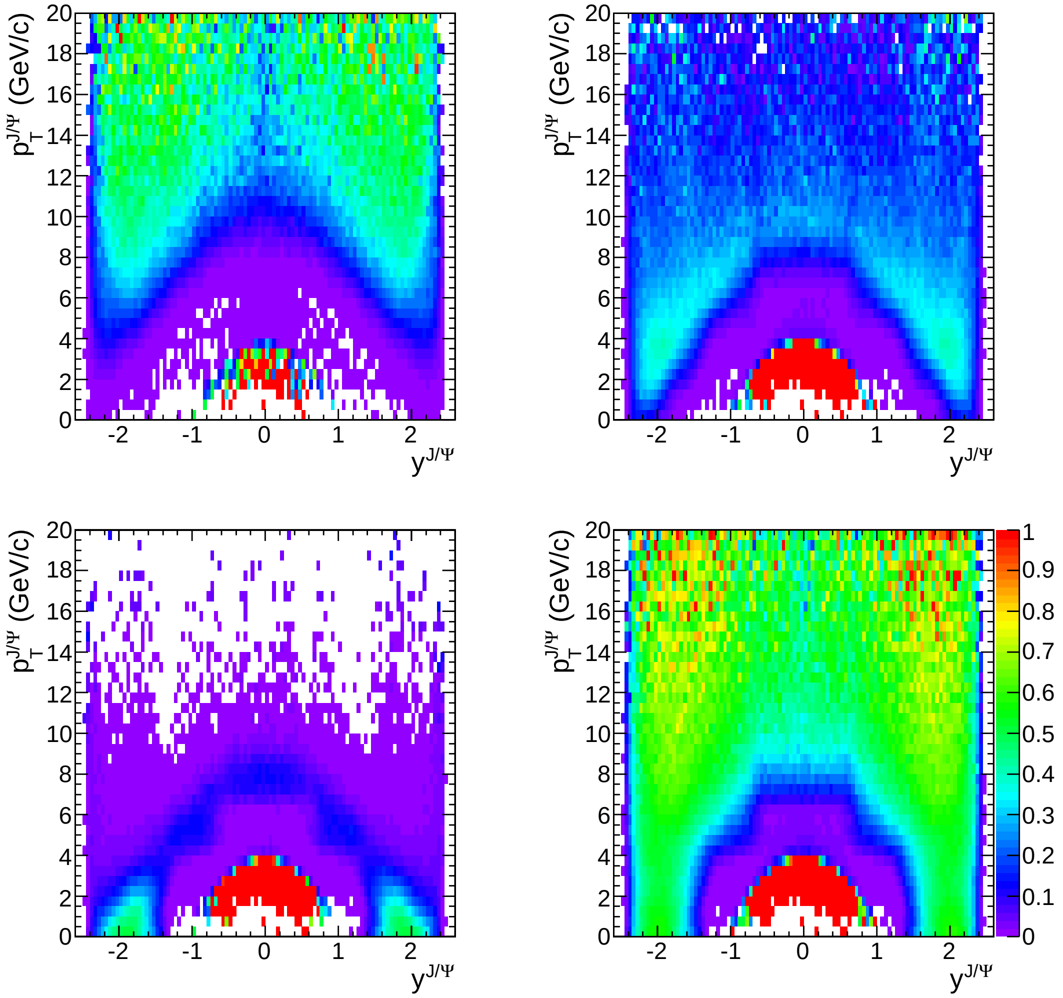

Figure 4.16: The reconstruction efficiency of global-global (left-upper), global-tracker (right-upper), tracker-tracker (left-bottom) and sum of the three (right-bottom) J/ψ reconstructed as a function of $p_T^{J/\psi}$-$y^{J/\psi}$ from MC simulated $J/\psi \to \mu\mu$ sample. The tracker muon raises the J/ψ efficiency from less than 10% to about 50% at the very low $p_T^{J/\psi}$ in the endcap. Due to the low statistic of the low $p_T^{J/\psi}$ area in the barrel part, the efficiency has got large uncertainty and is not reliable. In practice, efficiency of $J/\psi \to \mu\mu$ from experimental data is not so high as shown here, because of the limitation of trigger and muon geometry acceptance.

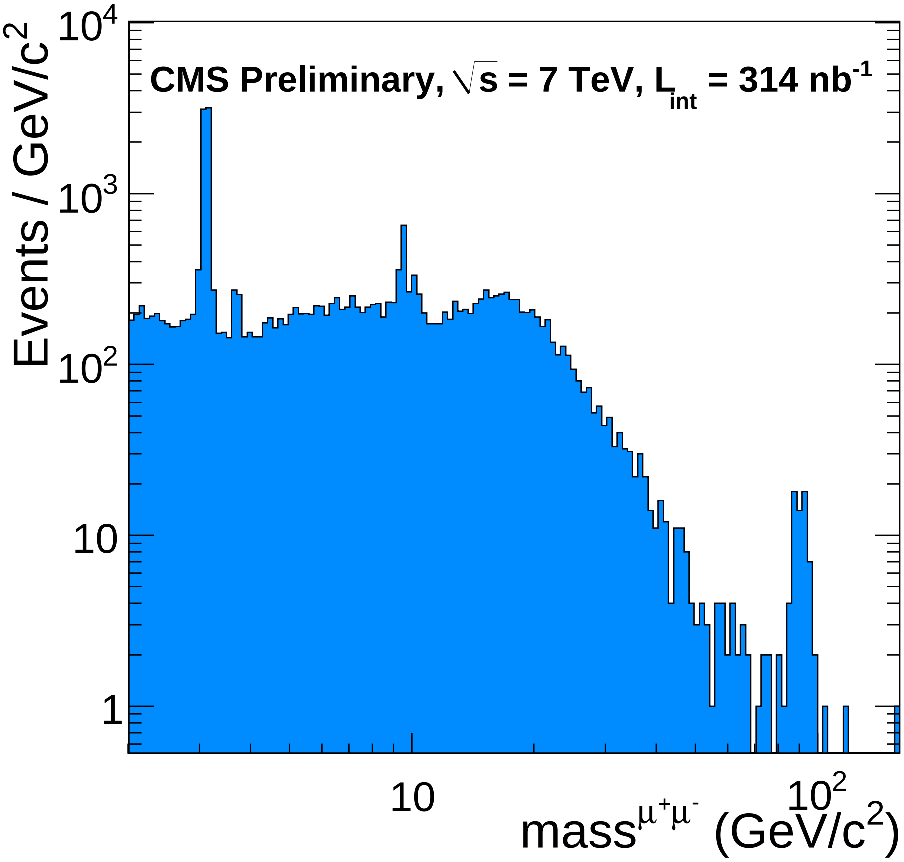

Figure 4.17: Di-global muon mass reconstructed in CMS, with HLT_DoubleMuOpen triggered and standard cuts.

nents, defined as

$$r = \sqrt{\epsilon \cdot \sigma_1^2 + (1-\sigma) \cdot \sigma_2^2} \tag{4.7}$$

$$e_r = \frac{1}{2r}\sqrt{(\sigma_1 \cdot \epsilon \cdot e_{\sigma_1})^2 + [\sigma_2 \cdot (1-\epsilon) \cdot e_{\sigma_2}]^2 + [\frac{1}{2}(\sigma_1^2 - \sigma_2^2)e_\epsilon]^2} \tag{4.8}$$

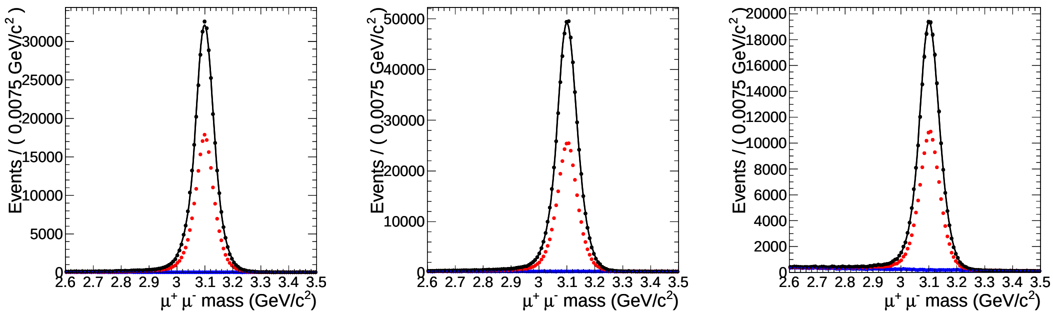

Figure 4.18: MC simulated J/ψ mass spectrum by GG(left)/GT(middle)/TT(right) muon pairs, including the prompt and nonprompt (the small Gaussian-like red dots in the middle of each plot) components and QCD background (the linear-like blue dots at the bottom of each plot), fitted by a Crystalball function plus a weighted Gaussian for signal and a exponential function for the QCD background.

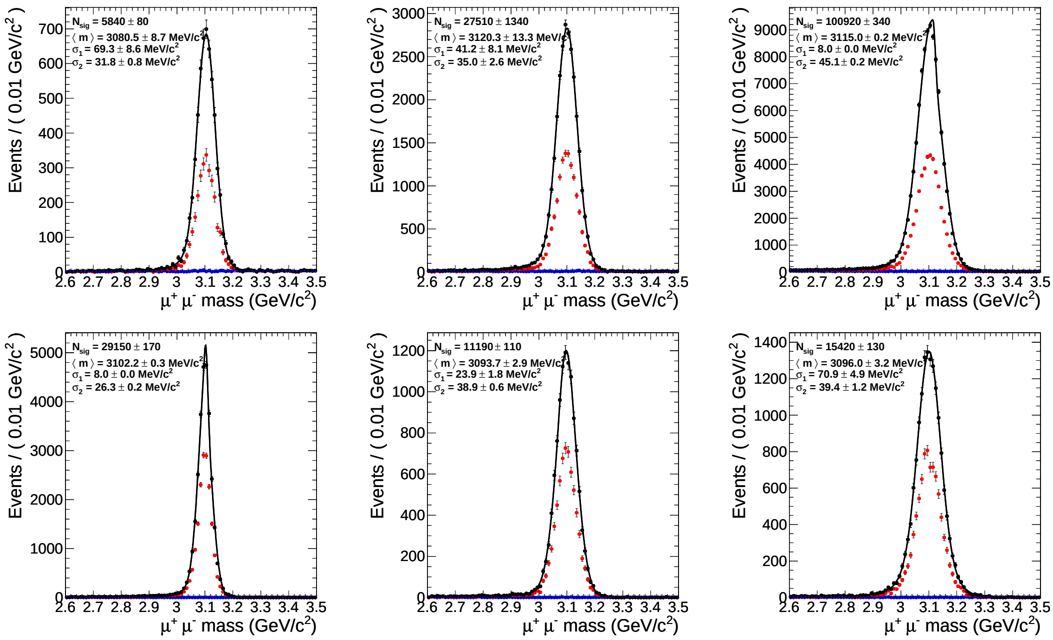

Figure 4.19: Invariant mass resonance fit of J/ψ in different transverse momentum and rapidity bins. $3.5 < p_T^{J/\psi} < 4.5$(upper), $12 < p_T^{J/\psi} < 15$(bottom) and $|y^{J/\psi}| < 1.2$(left), $1.2 < |y^{J/\psi}| < 1.6$(middle), $1.6 < |y^{J/\psi}| < 2.4$(right)

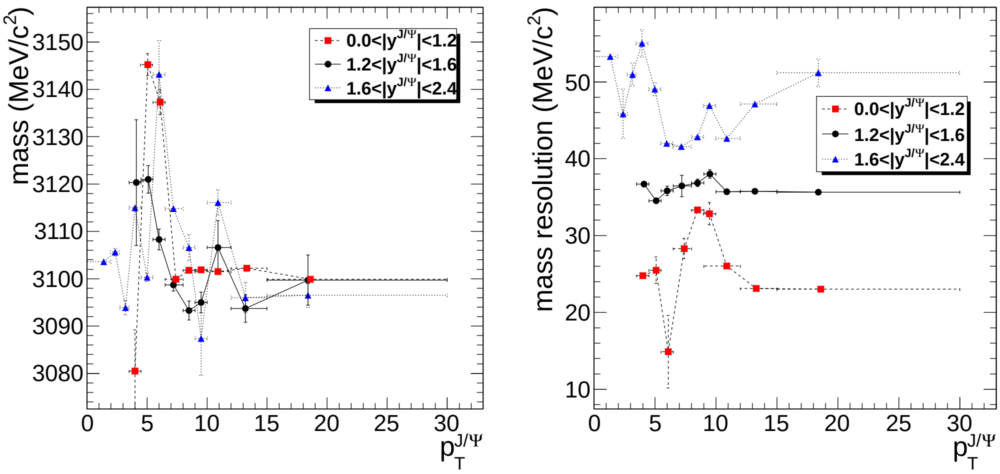

Figure 4.20: The mean value (left) and resolution (right) of invariant mass resonance as a function of $p_T^{J/\psi}$.

Chapter 5

Acceptance and efficiency

Acceptance (A) is the probability of the detectable J/ψ, reflecting the CMS geometrical coverage and the muon kinematical limitation. Since lacking of information at internal parts of the CMS detector, the acceptance is studied from MC simulation and experimental data kinematical fit. Efficiency (ϵ) is measured by the Tag-and-Probe method from data instead of the MC simulation. The MC transverse momentum and rapidity spectrum is reweighted to the data one to avoid the mean value migration.

5.1 J/ψ acceptance

Not all J/ψ generated from proton-proton collision could be detected, e.g. some muons decayed from J/ψ cannot be reconstructed due to the detectorgeometrical coverage (CMS muon system covers as far as $|\eta| = 2.4$) and the minimum transverse momentum measured[1] in the tracker and muon system. In this study, these parts below the minimum sensitivity will not be considered, including some ranges above the limitations of η and p_T, where the muon identical efficiency is increasing from a low one (10%). In Tag-and-Probe method, those parts with low efficiency have

[1]Muons collected in the barrel part could reach as low as around $p_T = 3GeV/c$ and $2GeV/c$ in the endcap, that is constrained mainly by track curvature in the magnetic field.

large uncertainty, so the parts with low muon efficiency are also removed in this analysis.

5.1.1 Central value of Acceptance

This section explains the calculation of J/ψ acceptance central value. Later in next section, some factors that may bias the acceptance will be studied.

5.1.1.1 Acceptance criteria

As mentioned in Section 4.1, the single muon identity efficiency is simulated in CMSSW. The sum of global and tracker muon efficiencies as a function of (transverse) momentum and pseudorapidity are shown in Fig. 5.1. To remove the part with low efficiency, muon at generator level will be selected only if it could pass a certain criteria, as shown in Table. 5.1.

From now on, the "accepted muon" means the single muon that passed this criteria. And the J/ψ acceptance, single and double muon reconstruction efficiency

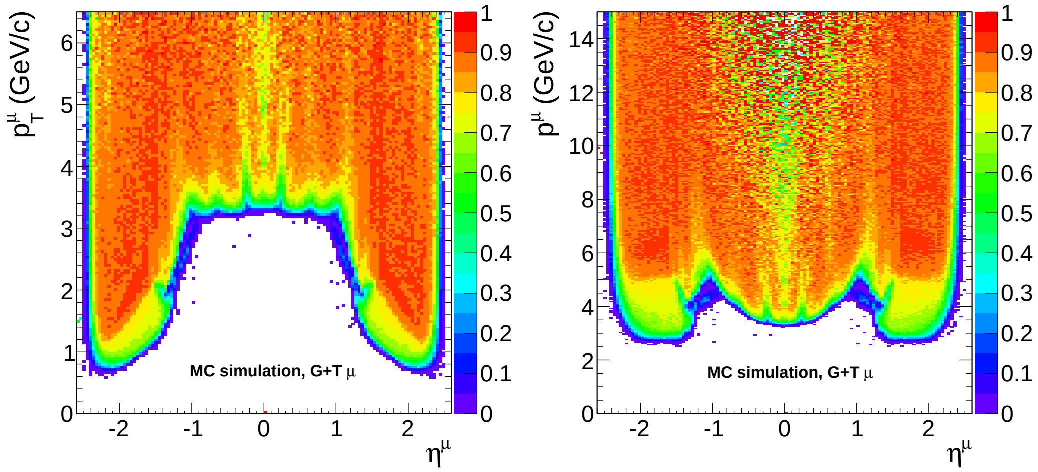

Figure 5.1: Reconstruction efficiency 2D distribution of single global plus tracker muon, as a function of p_T^{muon} (left) and p^{muon} (right) by muon pseudorapidity from MC simulated $J/\psi \to \mu^+\mu^-$ sample.

Table 5.1: The criteria of muon at the generator level, to remove muons in the muon with low identity efficiency.

$p_T^\mu > 3.3GeV/c,$	for $\|\eta^\mu\| < 1.3;$
$p^\mu > 2.9GeV/c,$	for $1.3 < \|\eta^\mu\| < 2.2;$
$p_T^\mu > 2.4GeV/c,$	for $2.2 < \|\eta^\mu\| < 2.4;$

and dimuon trigger are all based on the accepted muon, excluding the un-accepted one.

5.1.1.2 Prompt and nonprompt J/ψ acceptance

To calculate the acceptance, numerous prompt and nonprompt J/ψ events without any cuts on transverse momentum and rapidity are generated by the generator Pythia. Applying single muon selection criteria listed in Table. 5.1, the J/ψ acceptance is defined as,

$$A(p_T, y, \lambda_\eta) =< \frac{N_{det}^{J/\psi}(p_T, y, \lambda_\eta)}{N_{gen}^{J/\psi}(p_T, y, \lambda_\eta)} >_{bin}, \tag{5.1}$$

where,

- p_T and y are the J/ψ transverse momentum and rapidity at generator level;
- λ_η is one of the nine possible polarization scenarios [2];
- $N_{det}^{J/\psi}(p_T, y, \lambda_\eta)$ means the number of detectable J/ψ events that both of the two muons decayed from J/ψ passed the selection cuts in a give $p_T + \eta$ bin;
- $N_{gen}^{J/\psi}(p_T, y, \lambda_\eta)$ is the total number of generated J/ψ events in a given bin;
- $<>_{bin}$ indicates this acceptance being calculated bin by bin.

[2] The polarization scenario could be non-polarized and "transverse/longitudinal (t/l)" + "polar/azimuthal angle (θ/ϕ)" + "Helicity/Colins-Soper frame (HX/CS)".

However, transverse momentum and pseudorapidity of one single muon at MC generator level may have different values from the reconstruction level. Considering the differences, due to the resolution discussed in Section 4.1.2.2, the p_T^μ is smeared to another value from the one at generator level, based on the study of muon reconstruction. By fitting the J/ψ mass resonance and transverse momentum distribution with different p_T^μ as a function of η^μ, the muon resolution function $(\sigma(p_T^\mu)/p_T^\mu)$[59] in Fig. 5.2[3] has been parameterized as,

$$\frac{\sigma(p_T^\mu)}{p_T^\mu} = \begin{cases} c + b_1 \cdot |\eta^\mu|^2, & \text{if } |\eta^\mu| \leq b_0 \\ b_2 + b_3(|\eta^\mu| - b_4)^2, & \text{if } |\eta^\mu| > b_0 \end{cases} \tag{5.2}$$

where,

- $b_0 = 1.61$,
- $b_1 = 0.00503$,
- $b_2 = 0.0178$,
- $b_3 = 0.0122$,
- $b_4 = 1.33$,
- $c = b_2 + b_3(b_0 - b_4)^2 - b_1 \cdot b_0^2$.

Or,

$$\frac{\sigma(p_T^\mu)}{p_T^\mu} = \begin{cases} 0.00572 + 0.00503 \cdot |\eta^\mu|^2 & \text{if } |\eta^\mu| \leq 1.61 \\ 0.0178 + 0.0122 \cdot (|\eta^\mu| - 1.33)^2 & \text{if } |\eta^\mu| > 1.61 \end{cases} \tag{5.3}$$

Technically, a kinematical calibration to p_T^μ is investigated, that each muon's p_T^μ is smeared to be $p_T^{\mu\prime}$ according to its pseudorapidity value and the J/ψ acceptance is redefined to be,

$$A'(p_T, y, \lambda_\eta) =< \frac{N_{det}^{dimuon}(p_T^{dimuon\prime}, y^{dimuon}, \lambda_\eta)}{N_{gen}^{dimuon}(p_T^{dimuon}, y^{dimuon}, \lambda_\eta)} >_{bin}, \tag{5.4}$$

The acceptances of prompt and nonprompt J/ψ could be computed in this way from private MC samples, shown in Fig. 5.3. The prompt J/ψ is non-polarized and

[3]provided by Daniele TROCINO

the nonprompt J/ψ is reweighted from $\alpha = -0.333$ polarization in HX frame (the default setting in EvtGEN) to $\alpha = -0.409$ (measured from $\Upsilon(4S) \to J/\psi$ events in BaBar[60]).

5.1.1.3 Mixture of two J/ψ components

The prompt and nonprompt J/ψ should be mixed at the same integrated luminosity level. For all prompt J/ψ events generated, the cross section given by Pythia is $0.2118mb$. There are 16,921,111 J/ψ with particle ID $pid = 443$ from the total generated 61,400,000 events, i.e. the J/ψ rate is 27.56%. So the prompt $J/\psi \to \mu^+\mu^-$ cross section is,

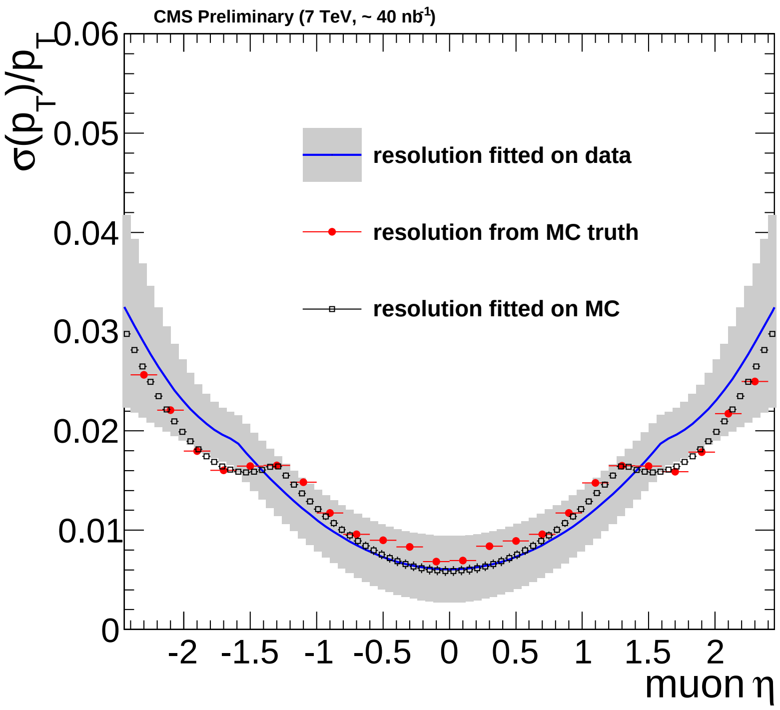

Figure 5.2: The muon reconstruction resolution as a function of η^μ.

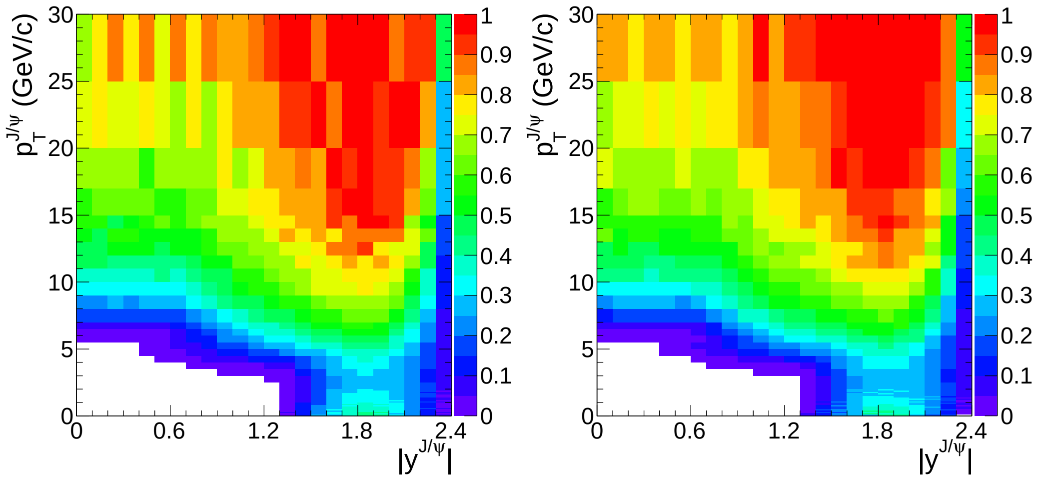

Figure 5.3: The 2D acceptance distribution of prompt (left) and nonprompt (right) J/ψ.

$$\begin{aligned}\sigma^{prompt} &= \sigma^{prompt}_{Pythia} \cdot r^{J/\psi} \cdot Br(J/\psi \to \mu^+\mu^-) \\ &= 0.2118mb \times 27.56\% \times 5.93\% \\ &= 3.43 \times 10^{-3} mb \qquad (5.5)\end{aligned}$$

where, the $Br(J/\psi \to \mu^+\mu^-) = 5.93\%$ is the branch ratio of J/ψ decaying to muon. And the nonprompt J/ψ is a little bit different,

$$\begin{aligned}\sigma^{nonprompt} &= \sigma^{nonprompt}_{Pythia} \cdot r^{J/\psi} \cdot Br(b \to J/\psi) \cdot 2 \cdot Br(J/\psi \to \mu^+\mu^-) \\ &= 48.44mb \times 0.64\% \times 2 \times 1.16\% \times 5.93\% \\ &= 4.24 \times 10^{-4} mb \qquad (5.6)\end{aligned}$$

where, $\sigma^{nonprompt}_{Pythia} = 48.44mb$ is the cross section of all B-events generated given by Pythia (EvtGEN), $r^{J/\psi} = 0.64\%$ is the J/ψ rate in all generated B-events, $Br(b \to J/\psi)$ is the branch ratio of b-hadron decaying to J/ψ and the factor 2 means there are 2 b-hadrons in one B-meson.

Then the mixed acceptance can be obtained as shown in Fig.5.4.

5.1.2 Some biases on acceptance

Some biases on the mixed acceptance, which may be influenced by some possible factors, are measured as the systematic uncertainties.

b-fraction

Considering the difference between the prompt acceptance map and the non-prompt one, both of the two are reweighted to the same integrated luminosity and mixed together. The fraction of mixture is from Pythia simulation, but the cross section of prompt J/ψ given by Pythia is not reliable, and the fraction of b-hadron is unknown in the inclusive experimental data sample. Here the b-fraction is re-estimated to $1 \pm 20\%$ to cover this unknown fraction. The difference between the two biased acceptances, between the 80% and the 120% b-fraction, is considered as one of the systematics.

b-polarization

The acceptance of nonprompt J/ψ has $\alpha = -0.409$ polarization in HX frame measured in BaBar experiment[60], which is different from $\alpha = -0.333$ predicted by EvtGEN. So the disparity of these two b-polarizations is one of the factors contributing to the systematic uncertainty.

Final state radiation

The J/ψ meson may radiate photons at the end of gluon-gluon refusion process, namely final state radiation (FSR). This may cause the variant property of J/ψ to the decayed muon pair, e.g. mean value of resonance mass, transverse momentum or rapidity value. The distinction of J/ψ and dimuon gives out another source of bias on acceptance. To avoid the double counting the varies between p_T^μ and $p_T^{\mu\prime}$, dimuon here use the p_T^μ before resolution function correction.

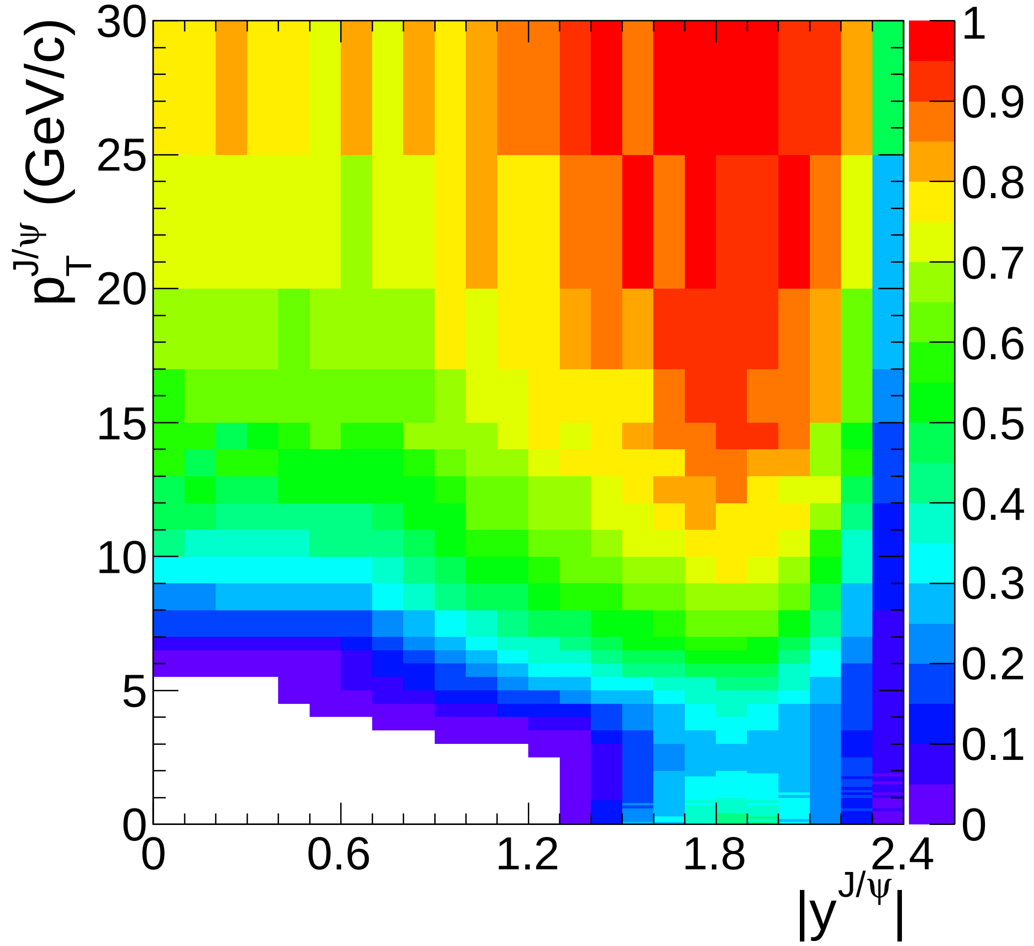

Figure 5.4: The mixed prompt and nonprompt J/ψ acceptance.

p_T^μ resolution

The p_T^μ has been smeared to $p_T^{\mu\prime}$ as described in the paragraph above. This resolution function has the maximum residual bias to be 0.05%. By over estimation this bias to be 0.1%, the $p_T^{\mu\prime}$ is further smeared to $p_T^{\mu\prime} \times (1 \pm 0.1\%)$. This difference from $p_T^{\mu\prime} \times (1 - 0.1\%)$ to $p_T^{\mu\prime} \times (1 + 0.1\%)$ is considered to be another systematic uncertainties.

p_T^μ calibration uncertainty

The calibration of p_T^μ to $p_T^{\mu\prime}$ has its immanent uncertainty. By smearing p_T^μ to be another value $p_T^{\mu\prime\prime}$, indicating the upper edge of the shadow superimposed to resolution curve in Fig. 5.2, the transformation from the acceptance based on $p_T^{\mu\prime}$ to that of $p_T^{\mu\prime\prime}$ is accepted to be one of the systematic uncertainties.

Kinematical distributions

The kinematical spectrum of J/ψ given by Pythia is different from experimental data or other simulation models, which must be count into uncertainties. The acceptance is recomputed by following the spectrum from CASCADE and CEM. Larger variances between the two new acceptances and the one from Pythia is taken into uncertainty.

Vertex position

The positions of primary and secondary vertices on the projection in z-axis influence the acceptance, since the signal points on muon chambers are quite different even the muons from different global vertices have the same local flying direction. To estimate this effect, two independent samples are selected, i.e. $|Z_0| < 0.1cm$ and $9 < |Z_0| < 11cm$, where $Z_0 = z - \sqrt{x^2 + y^2} \cdot \frac{p_z^{J/\psi}}{p_T^{J/\psi}}$ is defined in Fig. 5.5. The discrepancy on acceptances of these two samples is one of the systematic uncertainties. Their J/ψ kinematical spectrums at generator level are reweighted to the same one.

5.2 Efficiency

Firstly, the single muon identification and high level trigger efficiencies are calculated independently. The J/ψ efficiency is accessed by reweighting the J/ψ candidate kinematical spectrum.[4]

[4]The tag and probe result is calculated by Giovanni Petrucciani and the MC simulated result is summarized by me.

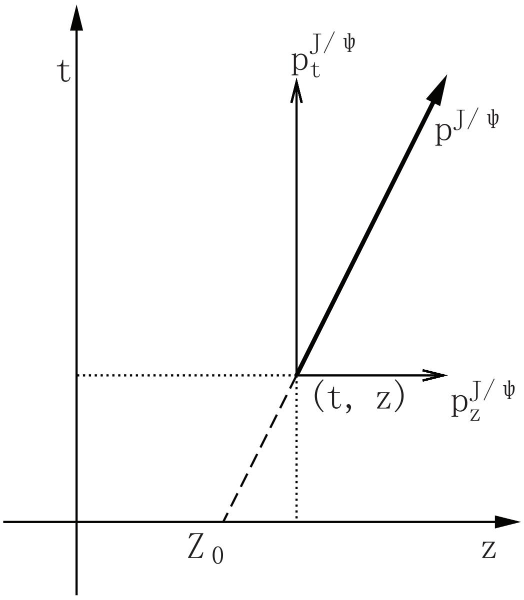

Figure 5.5: The schema of Z_0.

5.2.1 Single muon efficiency

Instead of MC simulated efficiency discussed in Section 4.2.1, the usage of Tag-and-Probe (TnP) methodology helps to calculate the single muon reconstruction and trigger efficiency from experimental data. Basic principle of TnP is explained in Section 4.1.2.1, that to define one "tag muon" with a very high reconstruction quality, to collect "probe muon" in all tracks/muons sharing the vertex of J/ψ candidate, to select the "passing probe muon" satisfying a criteria and the muon reconstruction efficiency is the ratio of "passing probe muon" over "probe muon".

In practice, the muon reconstruction efficiency is divided into three steps, that the tracking efficiency (ϵ_{track}), muon identification efficiency ($\epsilon_{off|track}$) and trigger efficiency ($\epsilon_{trig|off}$). So the finally combined offline reconstruction and trigger efficiency ($\epsilon(\mu)$) is,

$$\epsilon(\mu) = \epsilon_{track} \cdot \epsilon_{off|track} \cdot \epsilon_{trig|off} \tag{5.7}$$

The details are in references [58], [61] and [62]. And the results are shown in

Figs. 5.6, 5.7 and 5.8.

5.2.1.1 Tracking efficiency

Tracking efficiency is measured in TnP methodology. The tag particle is a well reconstructed global muon, with $p_T^\mu > 5GeV/c$, $|\eta^\mu| < 2.4$ and passed the HLT trigger. The probe particle is a stand-alone muon, with an opposite charge to the tag one, $p_T^\mu > 2.4GeV/c$ and $|\eta^\mu| < 2.4$. The tag muon and probe particle should share the same vertex, i.e. passing the vertex filter, and combined invariant mass should fall into the J/ψ resonance range. The passing probe is the stand-alone muon matches one tracker track, with $\Delta\eta < 0.4$, $\Delta R < 1.0$ and $\Delta p_T/p_T < 5.0$. The efficiencies are shown in Fig. 5.6.

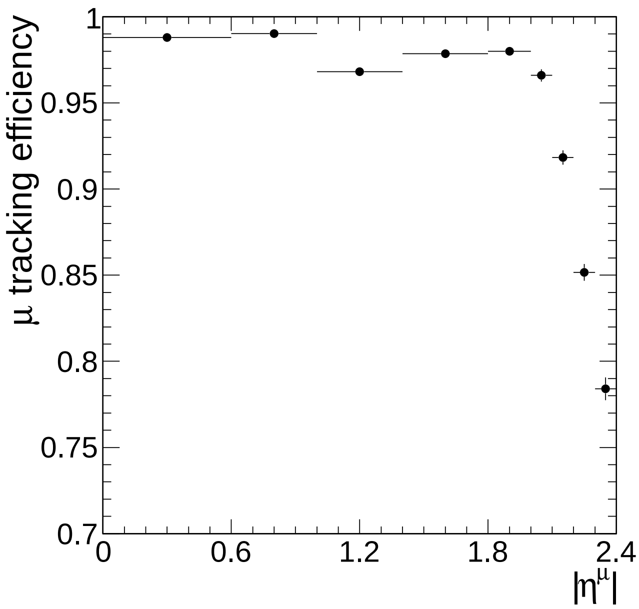

Figure 5.6: The muon tracking efficiency as a function of η^μ.

5.2.1.2 Muon identification

Similar to the tracking efficiency in Tag-and-Probe method, the tag muon is a global muon that passed HLT. The probe is a CaloMuon with $p_T^\mu > 0.7GeV/c$

and $|\eta^{\mu}| < 2.4$. The passing probe criteria is to match a global/tracker muon with the same selection cuts as the tracking efficiency. Efficiencies are shown in Fig. 5.7, where three pseudorapidity bins indicate for the barrel ($|\mu^{\eta}| < 1.0$), the overlap ($1.0 < |\mu^{\eta}| < 1.4$) and the endcap ($1.4 < |\mu^{\eta}| < 2.4$) region. The decreasing efficiency at large p_T^{μ}, as described in Chapter 4, is due to the *TMLastStationAngTight* selector, known to be inefficient at high p_T.

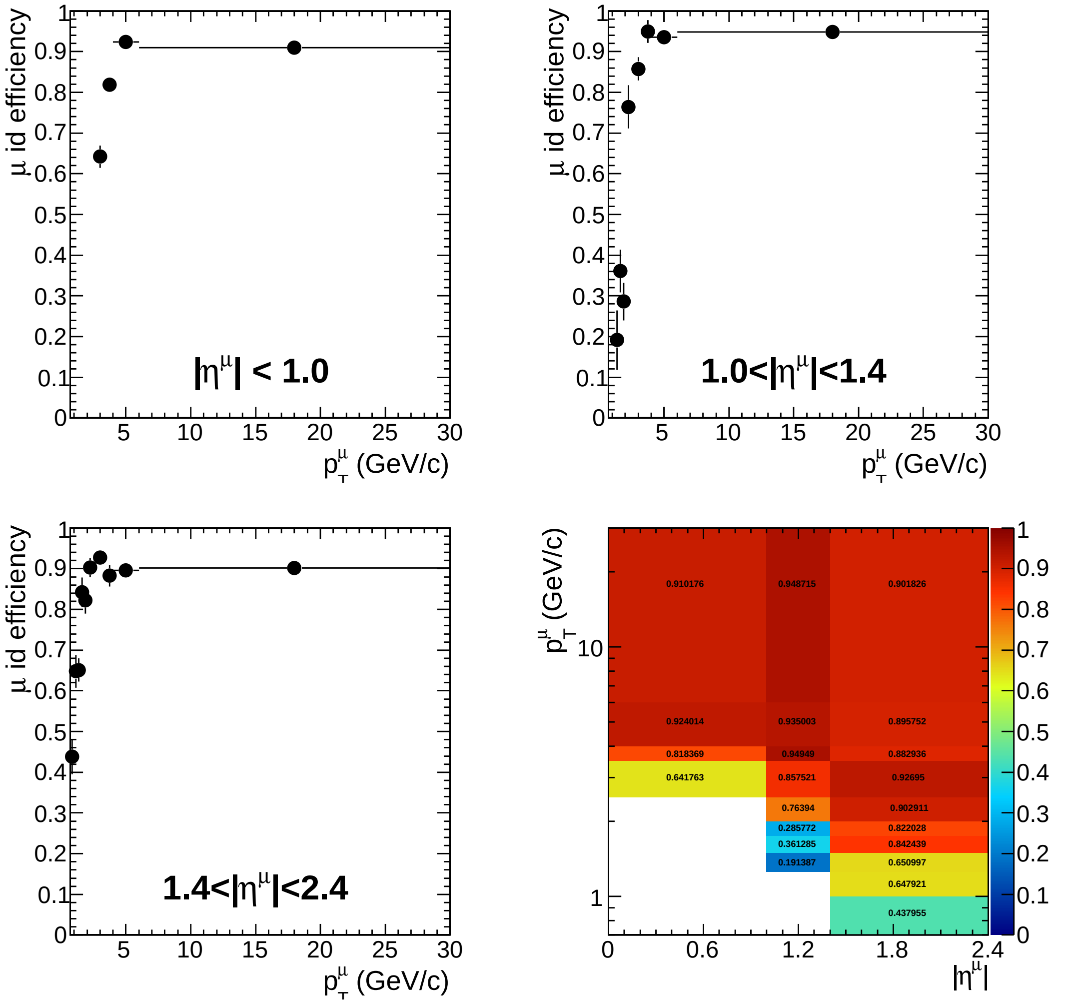

Figure 5.7: The muon identification efficiencies as a function of p_T^{μ} in regions of $|\eta^{\mu}| < 1.0$ (upper-left), $1.0 < |\eta^{\mu}| < 1.4$ (upper-right) and $1.4 < |\eta^{\mu}| < 2.4$ (bottom-left) and 2D efficiency plot (lower-right).

5.2.1.3 Trigger efficiency

Tag muon here is a global muon that passed HLT and with $p_T^\mu > 4GeV/c$ and $|\eta^\mu| < 2.1$, due to the non-existence of CSC beyond the $|\eta^\mu| = 2.1$. The probe muon is a global/tracker muon and passing probe is the one in the event passed a certain high level trigger.

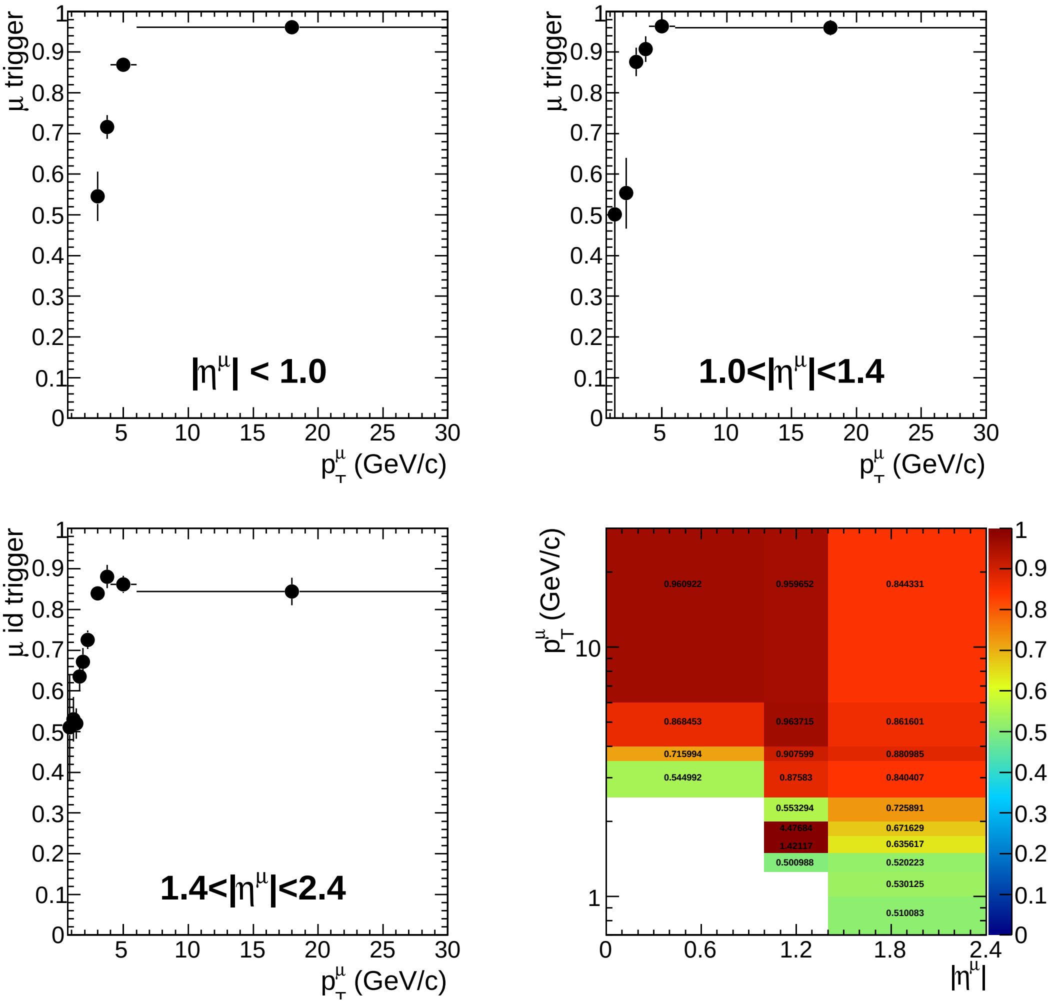

Figure 5.8: The single muon HLT_L1DoubleMuonZero trigger efficiencies as a function of p_T^μ in region of $|\eta^\mu| < 1.0$ (upper-left), $1.0 < |\eta^\mu| < 1.4$ (upper-right) and $1.4 < |\eta^\mu| < 2.4$ (bottom-left) and 2D efficiency plot (lower-right).

5.2.2 J/ψ efficiency

After the single muon efficiency is measured, the J/ψ efficiency could be calculated as,

$$\epsilon(J/\psi) = \epsilon(\mu^+) \cdot \epsilon(\mu^-) \cdot (1+\rho) \cdot \epsilon_{vertex} \tag{5.8}$$

where, $\epsilon(\mu^+)$ and $\epsilon(\mu^-)$ are single charged muon efficiencies investigated from TnP, $1+\rho$ is the correction factor between the efficiency of J/ψ and the product of two muon ones from MC simulation shown in Fig. 5.9 and ϵ_{vertex} is the probability of two muons from one common vertex. This ϵ_{vertex} is the ratio between number of global-global muon pairs with or without the common vertex filter to experimental data (see Section 4.2.1) in the region of $mass^{J/\psi} \pm 100 MeV/c^2$ where the high signal purity (95%) is measured and estimated to be $(98.35 \pm 0.16)\%$ [62] [5].

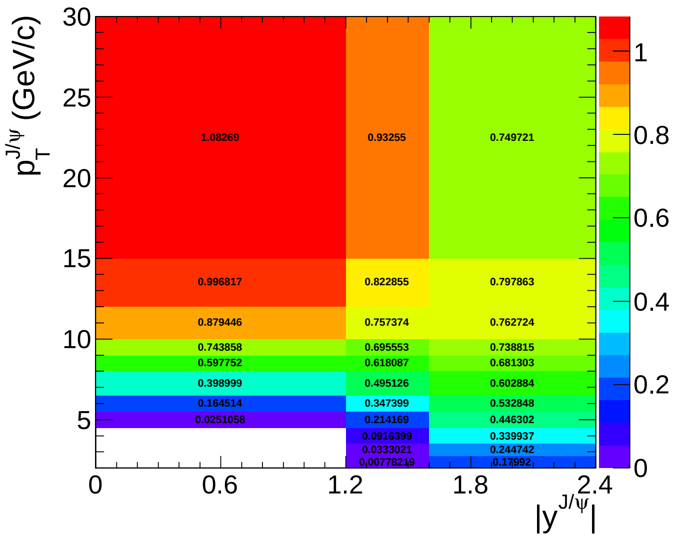

Figure 5.9: The (1+ρ) correction factor from MC simulation.

[5]The ρ and ϵ_{vertex} are measured by Luca Martini.

5.3 Corrected average value in $A \cdot \epsilon$

Actually, this J/ψ efficiency is still not very reliable yet, since the kinematic spectrum affects the efficiency distribution a lot, particularly when the bin size is very large. To avoid the efficiency position drifting, the acceptance and efficiency are reweighted to the data spectrum. The reweighted J/ψ acceptance and $< A \cdot \epsilon >_{bin}$ are shown in Fig. 5.10.

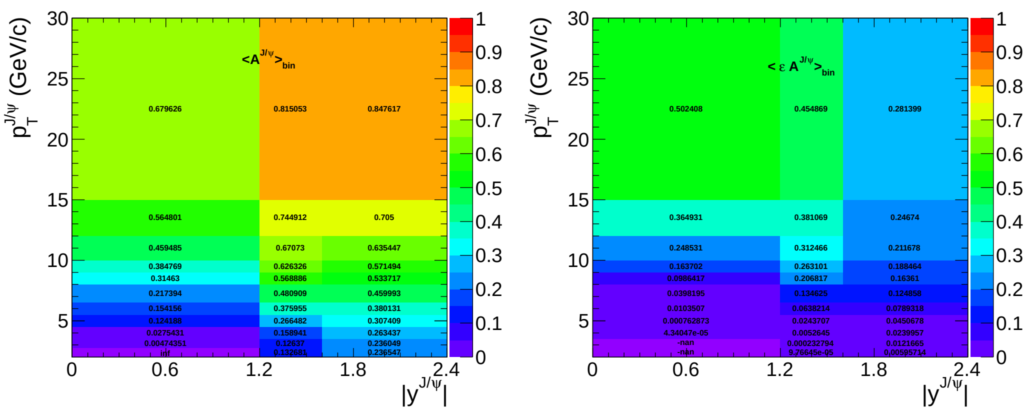

Figure 5.10: The acceptance (left) and $< A \cdot \epsilon >_{bin}$ (right) of J/ψ reweighted to experimental data kinematical spectrum.

By reading p_T and y of each J/ψ candidate, its acceptance value $A(p_T^{J/\psi}, y^{J/\psi})$ could be found in the 2D acceptance plot in Fig. 5.4. Also the efficiency $\epsilon(p_T^{\mu^+}, \eta^{\mu^+}, p_T^{\mu^-}, \eta^{\mu^-})$ is attained via checking the single muon efficiency's histogram and corrected with the ρ and ϵ_{vertex} factors. Thus, for one J/ψ candidate, the acceptance and efficiency, as well as the product $< A \cdot \epsilon >_{event}$ and $< \frac{1}{A \cdot \epsilon} >_{bin}$, could be calculated. For a bin of $(p_T^{J/\psi}, y^{J/\psi})$, these values are,

$$< A^{J/\psi} >_{bin} = < \frac{1}{N_{event}} \cdot \sum_{k=1}^{N_{event}} A_k >_{bin} \tag{5.9}$$

$$< \epsilon^{J/\psi} >_{bin} = < \frac{1}{N_{event}} \cdot \sum_{k=1}^{N_{event}} \epsilon_k >_{bin} \tag{5.10}$$

$$< A \cdot \epsilon >_{bin} = < \frac{1}{N_{event}} \cdot \sum_{k=1}^{N_{event}} (A_k \cdot \epsilon_k) >_{bin} \tag{5.11}$$

$$< \frac{1}{A \cdot \epsilon} >_{bin} = < N_{event} \cdot \sum_{k=1}^{N_{event}} \frac{1}{A_k \cdot \epsilon_k} >_{bin} \tag{5.12}$$

Chapter 6

Mass and lifetime fit

As discussed in Chapter 4, the dimuon invariant mass spectrum (including J/ψ, $\Psi(2S)$, $\Upsilon(nS)$ and Z boson peaks) is reconstructed clearly, as shown in Fig. 6.1.

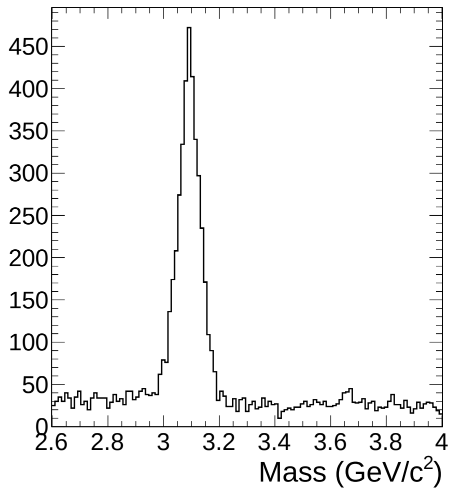

Figure 6.1: The global-global di-muon mass resonance spectrum in J/ψ mass region, reconstructed in CMS, HLT_DoubleMu0 triggered, with standard cuts.

J/ψ yields could be measured by fitting the mass spectrum in the [2.6, 3.5] (GeV/c^2) mass region. Considering the final state radiation, the dimuon candidate has a lower mass than the J/ψ truth and a tail at the low mass part of the mass peak, as shown in Fig. 6.5. Fitting the lifetime ($c\tau$) helps to count the numbers of prompt and nonprompt J/ψ events, which helps to sperate cross sections of these two components.

6.1 J/ψ mass spectrum

In each $p_T^{J/\psi}$ and $y^{J/\psi}$ bin, the signal mass peak is fitted by Crystal ball function (CB) and the QCD background by exponential function. As explained in Section 4.2, the J/ψ candidate is selected from the best combination of global and tracker muons. The three J/ψ categories (global-global, global-tracker, tracker-tracker) and the sum of the three are fitted and shown in Fig. 6.2. Approximately, 18.8% are global-global muon pairs, 45.9% are global-tracker pairs and 34.3% are tracker-tracker pairs. The following fits are all on the sum of the three, as described in Section 4.2.

Also some other functions, e.g. a double Gaussian for the signal and a polynomial function for the background, are tested. The difference is considered to be a systematic uncertainty.

6.1.1 Crystal ball function fit

The crystal ball for signal and the exponential function for background are chosen in fitting. Some examples, including the mass peak and pull value, are shown below in Figs. 6.3 and 6.4. Detailed fitting in each bin is plotted and listed in Appendix D.

6.1.2 A test on other functions

Since two muons in different p_T^{μ} and η^{μ} may have different resolutions in CMS detector, the Crystal ball plus Gaussian function performs better here than the single Gaussian in describing the mass shape, as shown in Fig. 6.5. Here the double Gaussian for the signal and polynomial function for the background are proposed, as shown in Figs. 6.6 and 6.7. Detailed fitting in each bin is plotted and listed in Appendix C.

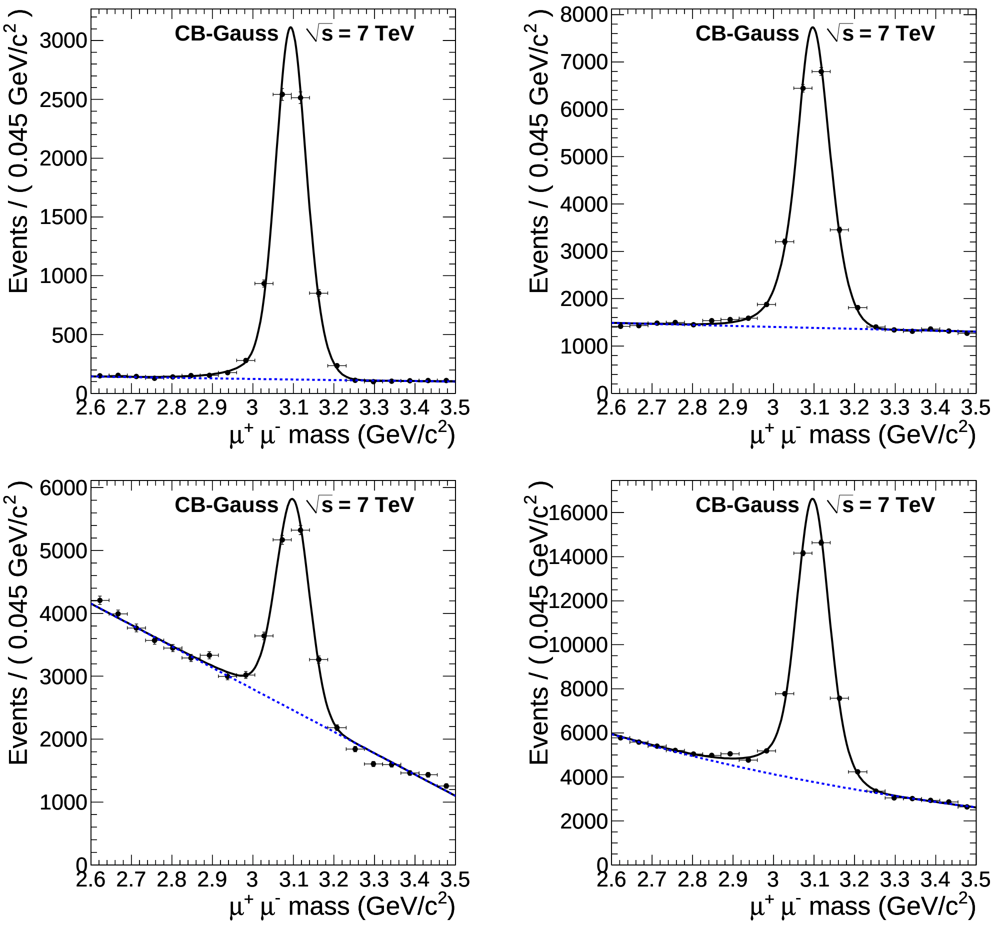

Figure 6.2: J/ψ mass fitted by Crystal ball function, for the global-global pair (upper-left), global-tracker pair (upper-right), tracker-tracker pair (bottom-left) and sum of the three (bottom-right).

6.2 J/ψ lifetime fit

J/ψ lifetime fit [1] is used to count the number of dimuon events, which could be prompt J/ψ, nonprompt one and QCD background. Here only a brief introduction to the lifetime fit in the J/ψ cross section study [61] is given. Detailed process is described in Reference [62].

[1]This part of job is done by Roberto Covarell.

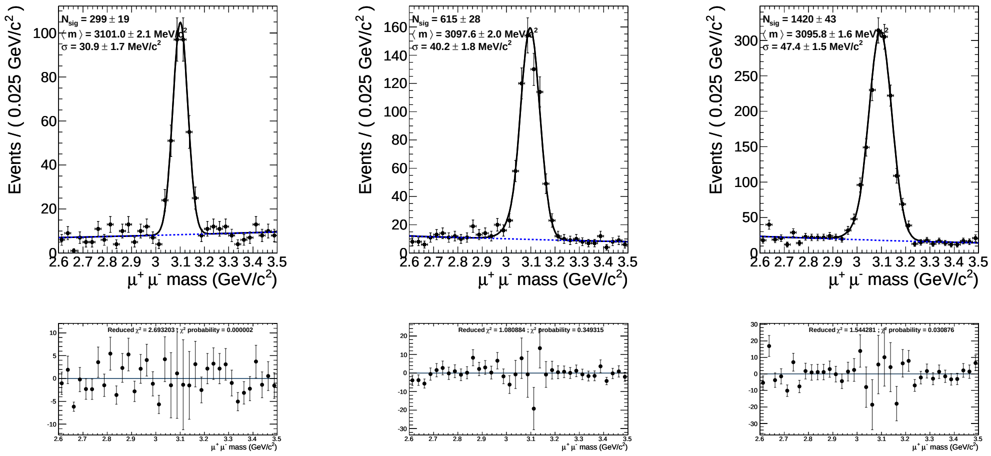

Figure 6.3: J/ψ mass fitted by crystal ball and exponential function, in transverse momentum region $4.5 < p_T^{J/\psi} < 5.5$ GeV/c and rapidity region $|y^{J/\psi}| < 1.2$ (left), $1.2 < |y^{J/\psi}| < 1.6$ (middle) and $1.6 < |y^{J/\psi}| < 2.4$ (right). Small plots at bottom are pull, i.e. the variation between data dots and fitted curve.

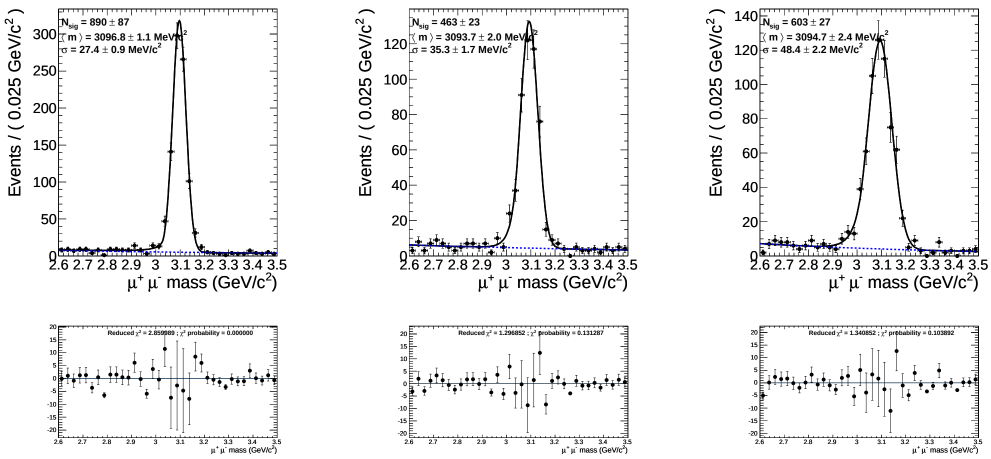

Figure 6.4: J/ψ mass fitted by Crystal ball and exponential function, in transverse momentum region $8 < p_T^{J/\psi} < 10$ GeV/c and rapidity region $|y^{J/\psi}| < 1.2$ (left), $1.2 < |y^{J/\psi}| < 1.6$ (middle) and $1.6 < |y^{J/\psi}| < 2.4$ (right).

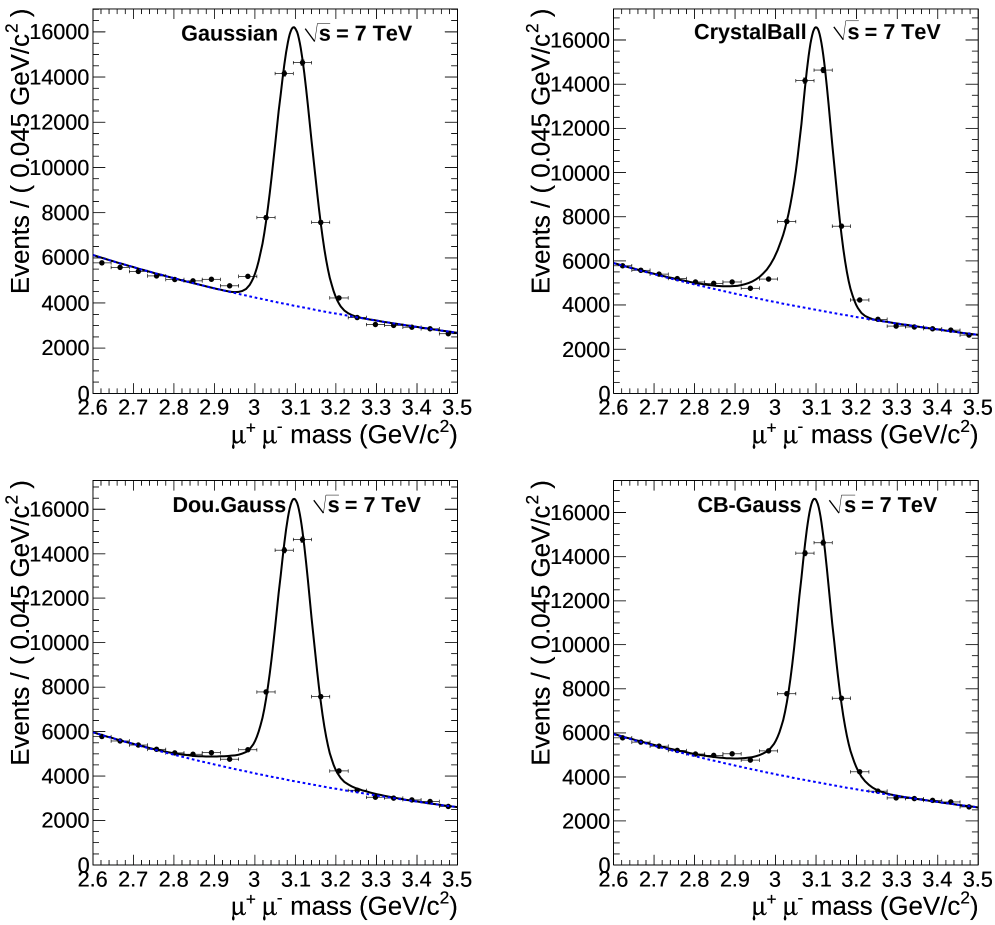

Figure 6.5: J/ψ mass fitted by the single Gaussian (upper-left), single Crystal ball (upper-right), double Gaussian (bottom-left) and Crystal ball plus Gaussian (bottom-right).

6.2.1 Determination of prompt and nonprompt fraction

In J/ψ cross section study, a two-dimension fit to invariant mass and lifetime distributions simultaneously is held. The mass component is the same as discussed in previous section. The life time is measured as below.

First of all, $c\tau$ templates of prompt J/ψ, nonprompt one and QCD background are generated from MC simulation, as shown in Fig. 6.8. The $c\tau$ of signals, i.e. prompt and nonprompt J/ψ, are described by a triple Gaussian function. The $c\tau$ of

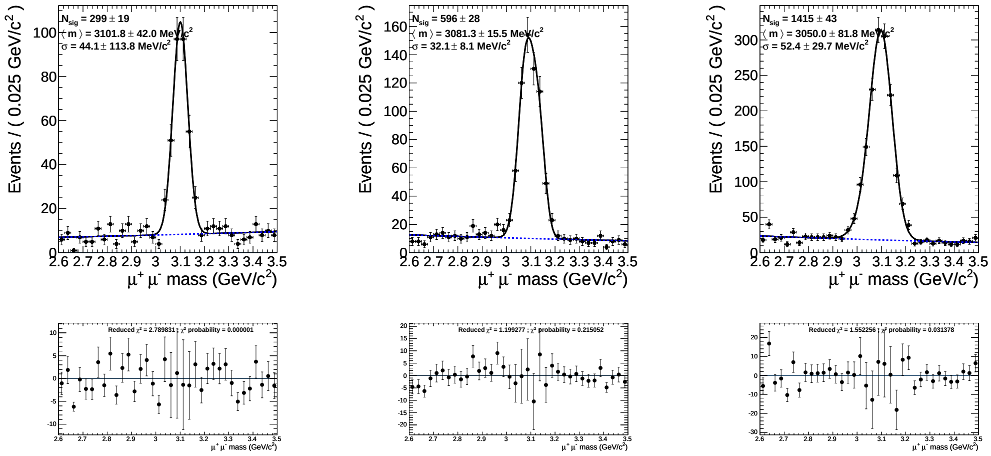

Figure 6.6: J/ψ mass fitted by double Gaussian and polynomial function, in transverse momentum region $4.5 < p_T^{J/\psi} < 5.5$ GeV/c and rapidity region $|y^{J/\psi}| < 1.2$ (left), $1.2 < |y^{J/\psi}| < 1.6$ (middle) and $1.6 < |y^{J/\psi}| < 2.4$ (right).

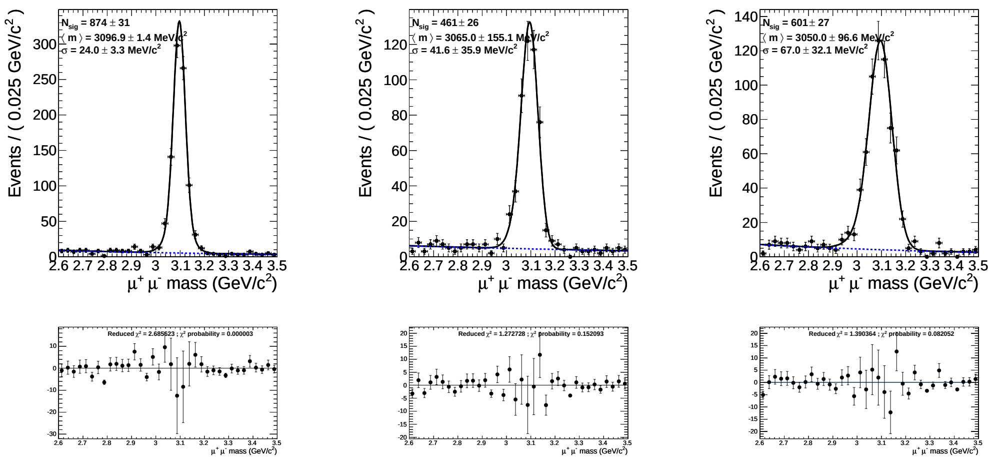

Figure 6.7: J/ψ mass fitted by double Gaussian and polynomial function, in transverse momentum region $8 < p_T^{J/\psi} < 10$ GeV/c and rapidity region $|y^{J/\psi}| < 1.2$ (left), $1.2 < |y^{J/\psi}| < 1.6$ (middle) and $1.6 < |y^{J/\psi}| < 2.4$ (right).

background is fitted by a decay function, its resolution function is exactly the same as signals double Gaussian function, which means the background has the same fraction ratio as the prompt component over nonprompt one. Output parameters in this pre-fit will be used as initial numbers in the final 2D fit, to optimized the fitting process.

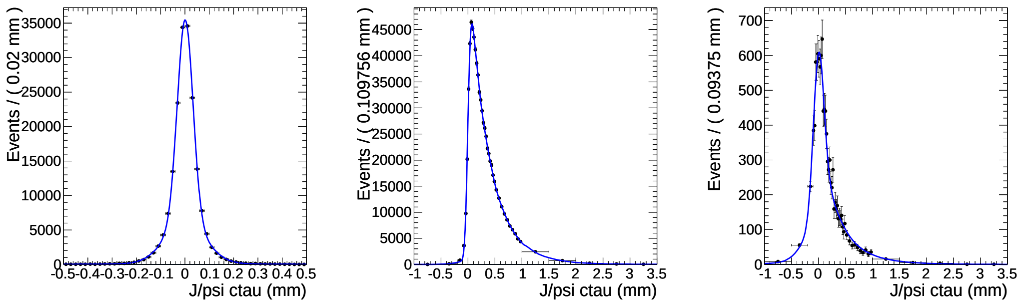

Figure 6.8: The $c\tau$ value distributions of prompt J/ψ (left), nonprompt one (middle) and QCD background (right) reconstructed by two global muons.

Secondly, the mass shape is pre-fitted for the J/ψ peak and the background sideband. Also numbers from this fit will go to next step. This is similar to the mass fit in the previous section, as shown in Fig. 6.9.

Thirdly, the $c\tau$ distribution of data in the region of J/ψ mass sideband, i.e. outside 3σ of J/ψ mass peak, will be pre-fitted to determine the $c\tau$ parameters of background. Also parameters in this step will be fixed for the final 2D fit. Some examples are shown in Fig. 6.10.

Last, but the most important, the final 2D fit is held to count the numbers of prompt and nonprompt J/ψ event. Some examples are shown in Fig. 6.11.

6.2.2 Systematic uncertainty in lifetime fit

The possible systematics in lifetime fit are listed below.

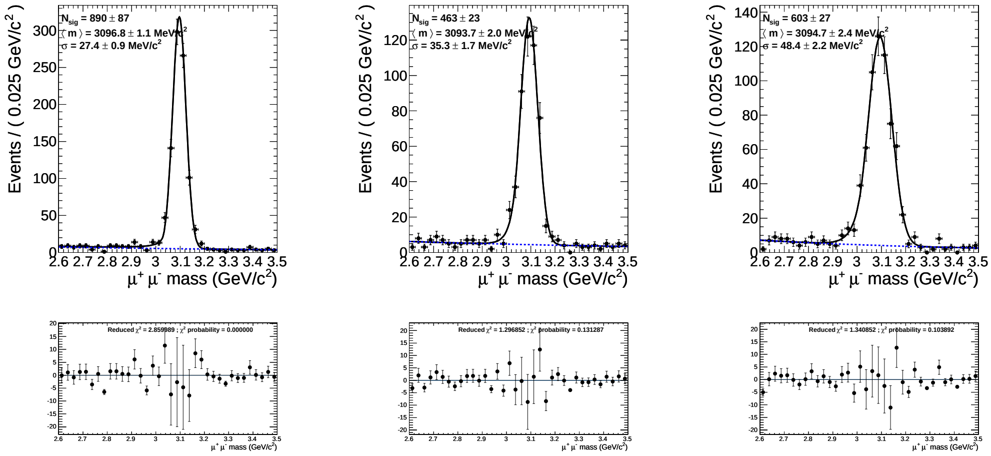

Figure 6.9: J/ψ mass fitted by Crystal ball and exponential function, in transverse momentum region $8 < p_T^{J/\psi} < 10$ GeV/c and rapidity region $|y^{J/\psi}| < 1.2$ (left), $1.2 < |y^{J/\psi}| < 1.6$ (middle) and $1.6 < |y^{J/\psi}| < 2.4$ (right).

B-hadron lifetime

In the 2D fit, the signals, for both of prompt and nonprompt J/ψ, are treated together. That is to say, the prompt and nonprompt J/ψ have the same possibility density function in $c\tau$ but different fit results. Actually, the nonprompt component has a more complex distribution and this fit is re-done with the decay function smeared from exponential function. The difference is considered to be a systematics.

$c\tau$ resolution model

In the central value measurement, a triple Gaussian is set as the resolution of a decay model. Alternatively, this fit is re-done by using a double Gaussian instead. The variation of these two is a systematic error.

Misalignments in Tracker

At different periods of data collecting, the misalignment is updating from time to time. Data will be re-reconstructed with new misalignment constants. The

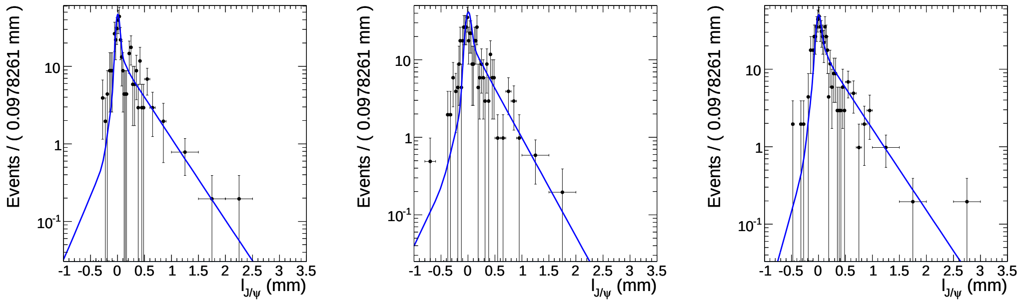

Figure 6.10: Sideband $c\tau$ value distribution fit of J/ψ candidate in region of $6.5 < p_T^{J/\psi} < 8.5$ GeV/c and $|y^{J/\psi}| < 1.2$ (left), $1.2 < |y^{J/\psi}| < 1.6$ (middle) and $1.6 < |y^{J/\psi}| < 2.4$ (right).

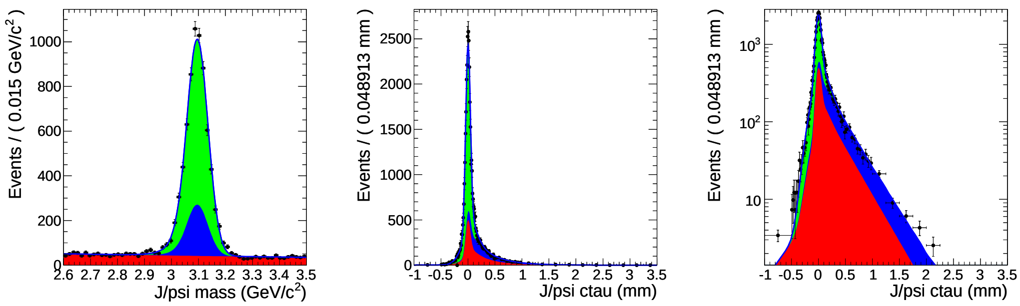

Figure 6.11: The 2D fit of mass spectrum (left), $c\tau$ value distribution in linear coordinate (middle) and life time in logarithmic coordinate (right) reconstructed from two global muons. Totally, 5072.39 ± 78.25 prompt J/ψ plus 1572.78 ± 52.63 nonprompt one are extracted, i.e. $23.67 \pm 0.66\%$ b-fraction.

change of the 2D fit from two data samples is taken as a source of uncertainties.

Primary vertex

In $c\tau$ calculation, the distance is based on the primary vertex of the whole event, which could be biased. $c\tau$ is recalculated from the beam spot and the 2D fit is re-done. The difference is a systematic.

Background pre-fit

Before the final 2D fit, the parameters of background component is pre-fit in the sideband of J/ψ mass region. This sideband is chosen from $\pm 3\sigma$ to $\pm 5\sigma$ and the difference of these two pre-fits gives a piece of contribution to systematics.

J/ψ efficiencies

The prompt and nonprompt J/ψ efficiencies could be different, due to their different kinematical distributions. The variation of these two efficiencies from MC simulation is accepted to be a systematic uncertainties.

In the end of this chapter, some comparisons of b-fraction in different experiments are shown in Fig. 6.12. The b-fraction is approximately constant in a certain p_T, no matter how large the center-mass-energy is.

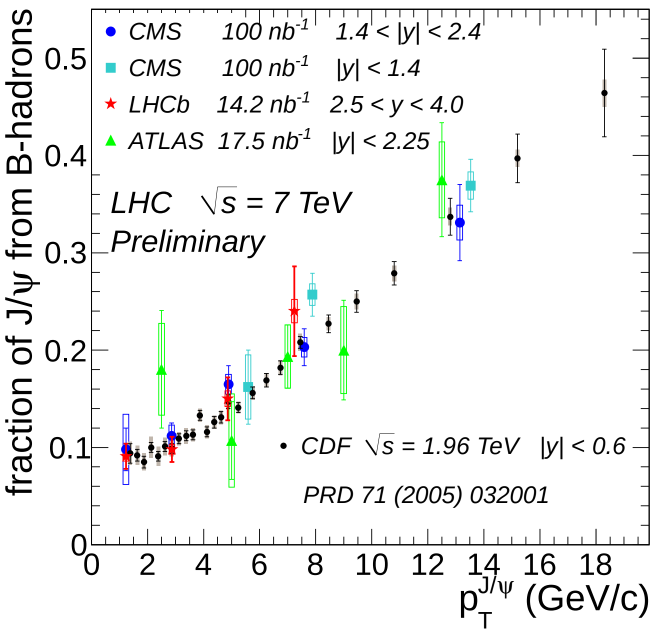

Figure 6.12: b-fraction distributions in different experiments as a function of $p_T^{J/\psi}$, summarized by Hermine Woehri.

Chapter 7

J/ψ cross section measurement

The J/ψ cross section is calculated as a double differential one,

$$\frac{d^2\sigma_{J/\psi}}{dp_T dy} \cdot Br(J/\psi \to \mu^+\mu^-) = \frac{N^{J/\psi}_{\text{corrected}}}{\Delta p_T \Delta y \mathcal{L}} \tag{7.1}$$

where $\mathcal{L}$ is the integrated luminosity, $N_{\text{corrected}}$ is the corrected J/ψ yields in a given transverse momentum and rapidity bin, Δp_T (Δy) is the size of transverse momentum (rapidity) bin and $Br(J/\psi \to \mu^+\mu^-)$ is the branch ratio of the J/ψ decaying into two muons.

7.1 Inclusive J/ψ cross section

Based on the $314nb^{-1}$ data collected by CMS up to September 2010, the inclusive J/ψ cross section is calculated to be,

$$251.4 \pm 3.6(stat) \pm 29.9(syst) \pm 27.6(lumi) \text{ nb}$$

For the J/ψ meson in region of $4.5 < p_T^{J/\psi} < 30GeV/c$ and $|y^{J/\psi}| < 2.4$, where the systematic uncertainty is mainly from statistical precision of TnP in the muon efficiency measurement from experimental data. The systematic uncertainty from luminosity is the standard number (11%) in the early CMS analysis.

For each transverse momentum and rapidity bin, the cross section is measured and shown in Fig. 7.1. And the value of each point shown in Table. 8.4 in Appendix E.

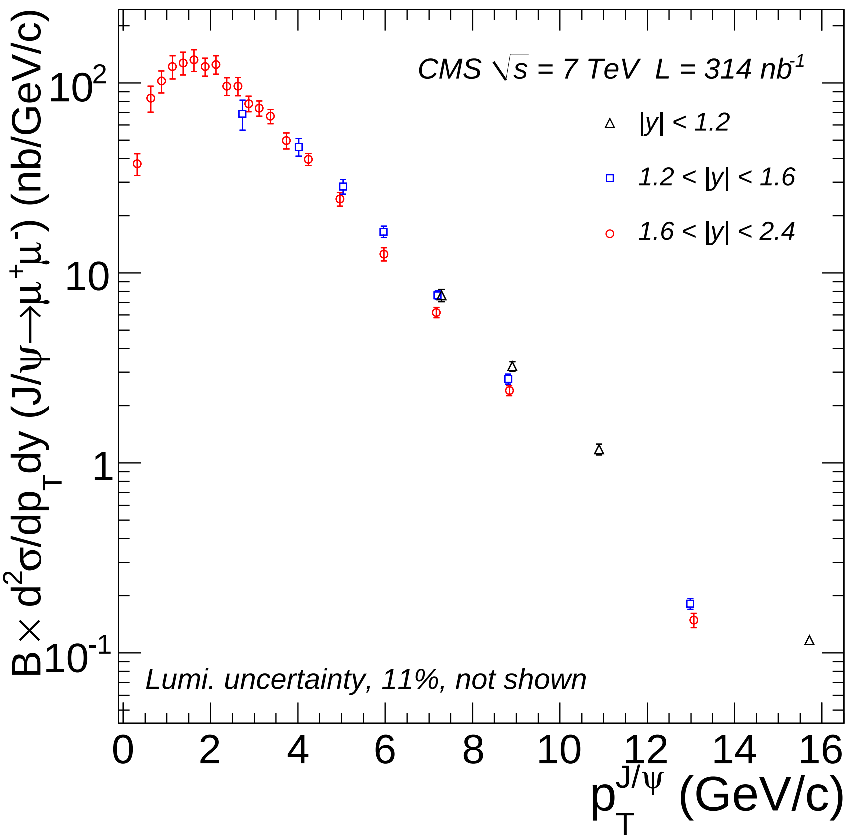

Figure 7.1: The inclusive J/ψ cross section as a function of $p_T^{J/\psi}$ in three rapidity bins.

7.2 Prompt and nonprompt J/ψ cross sections

After the mass-lifetime 2D fit, the number of prompt and nonprompt J/ψ events could be calculated and their cross sections are shown in Figs. 7.2 and 7.3. These two plots are approved by CMS collaboration and published in Ref. [61].

Here, some theoretical predictions are also plotted on the same plots, e.g. the Pythia[63] generator and CASCADE[64] one. Also the CEM (Color Evaporation

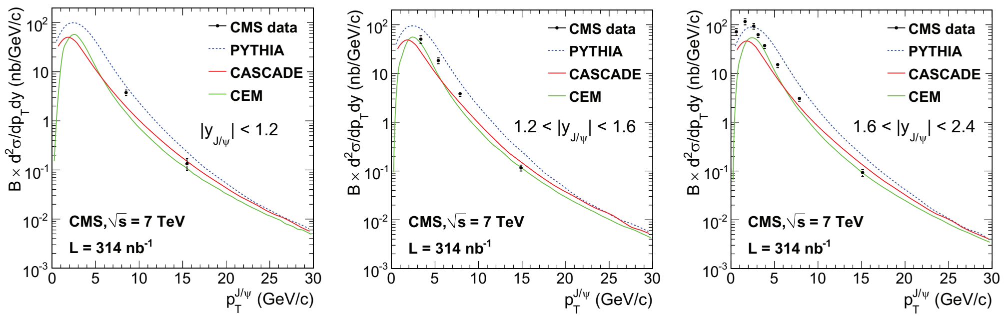

Figure 7.2: The prompt J/ψ cross section as a function of $p_T^{J/\psi}$ in three rapidity bins, compared with some theoretical models.

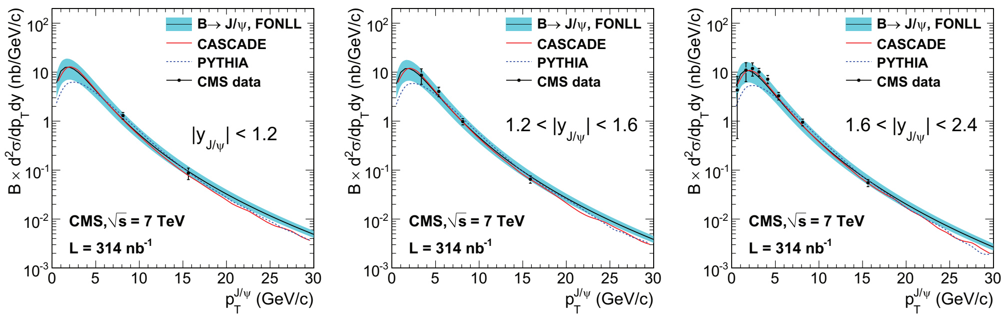

Figure 7.3: The nonprompt J/ψ cross section as a function of $p_T^{J/\psi}$ in three rapidity bins, compared with some theoretical models.

Model) prediction for the prompt J/ψ and the FNOLL [65] framework for non-prompt. The agreement of theoretical model and experimental data is found, except Pythia is two times higher.

Chapter 8

Conclusion and forecast

In this thesis, the J/ψ cross section in CMS is measured to be $251.4 \pm 3.6(stat) \pm 29.9(syst) \pm 27.6(lumi)$ nb, with good agreement to the theoretical model predictions. The systematic uncertainty is also controlled at a relatively low level.

With the increasing of LHC luminosity, about $40pb^{-1}$ data is now available till the end of 2010. Further measurements on both of J/ψ and $\psi(2S)$ cross sections are carried with the p_T extending to 70 GeV/c. This will report in another paper. As well as the polarization study is on going by other groups. Measurements on cross section and polarization will help to understand the production mechanism of the heavy quarkonia in hadronic collision.

Appendix

A Acronyms and abbreviations

ALICE	A Large Ion Collider Experiment
AOD	Analysis Object Data
APE	Alignment Position Error
ATLAS	A Toroidal LHC ApparatuS
BES	BEijing Spectrometer
BPH	B-PHysics group
CSC	Cathode Strip Chamber
CDF	Collider Detector at Fermilab
CERN	Conseil Européen pour la Recherche Nucléaire
c.m.	center-of-mass frame
CMS	Compact Muon Solenoid
CMSSW	CMS SoftWare
CEM	Color Evaporation Model
CLEO	Cornell's Largest Experimental
COM	Color Octet Mechanism
CRAB	CMS Remote Analysis Builder
CSM	Color Singlet Model
CS	Collins-Soper frame

CTF	Combinatorial Track Finder
DT	Drift Tube
EB	ECAL Barrel
EDM	Event Data Model
EE	ECAL Endcap
EGEE	Enabling Grids for E-sciencE
ES	PrEShower detector
ECAL	Electromagnetic CALorimeter
FNAL	Fermi National Accelerator Laboratory (Fermilab)
GT	Global Trigger
HCAL	Hadron CALorimeter
HB	HCAL Barrel
HE	HCAL Endcaps
HF	HCAL Forward
HLT	Higher Level Trigger
HO	Outer barrel Hadron calorimeter
HX	Helicity frame
LAS	Laser Alignment System
LCG	LHC Computing Grid
LDME	Lang Distance Matrix Element
LEP	Large Electron - Positron (collider)
LHC	Large Hadron Collider
LHCb	LHC-beauty
LHCf	LHC-forward
LINAC	LINear ACcelerator at CERN

LO	Leading Order
MB	Muon Barrel
MC	Monte Carlo
ME	Muon Endcaps
MTCC	Magnet Test and Cosmic Challenge
NLO	Next-to-Leading Order
NNLO	Next-to-Next-to-Leading-Order
NRQCD	Non Relativistic Quantum ChromoDynamics
NuSea	Nucleonic Sea experiment
PDF	Parton Distribution Functions
PDG	Particle Data Group
pQCD	perturbative Quantum ChromoDynamics
POG	Physics Object Groups
PS	Proton Synchrotron
PSB	Proton Synchrotron Booster
QCD	Quantum ChromoDynamics
QED	Quantum ElectroDynamics
QWG	Quarkonium Working Group
RPC	Resistive Plate Chamber
SM	Standard Model
SPS	Super Proton Synchrotron
SST	Silicon Strip Tracker
TIB	Tracker Inner Barrel
TID	Tracker Inner Disks
TOB	Tracker Outer Barrel

TEC	Tracker End Caps
TnP	Tag and Prob methodology
TOTEM	TOTal Elastic and diffractive cross section Measurement
TriDAS	CMS Trigger and Data Acquisition System
TSG	Trigger Study Group
VPT	Vacuum Photo Triodes

B J/ψ mass fit in crystal ball function

Here the J/ψ mass, fitted by the Crystal ball function for the signal (both of prompt and nonprompt J/ψ events) and exponential function for the QCD background, are plotted in each p_T and y bin. The number of fitted signal events are printed in the legend of each plot, as well as the mean value and resolution. The bin size value and number of J/ψ yields are summarized in Table 8.1.

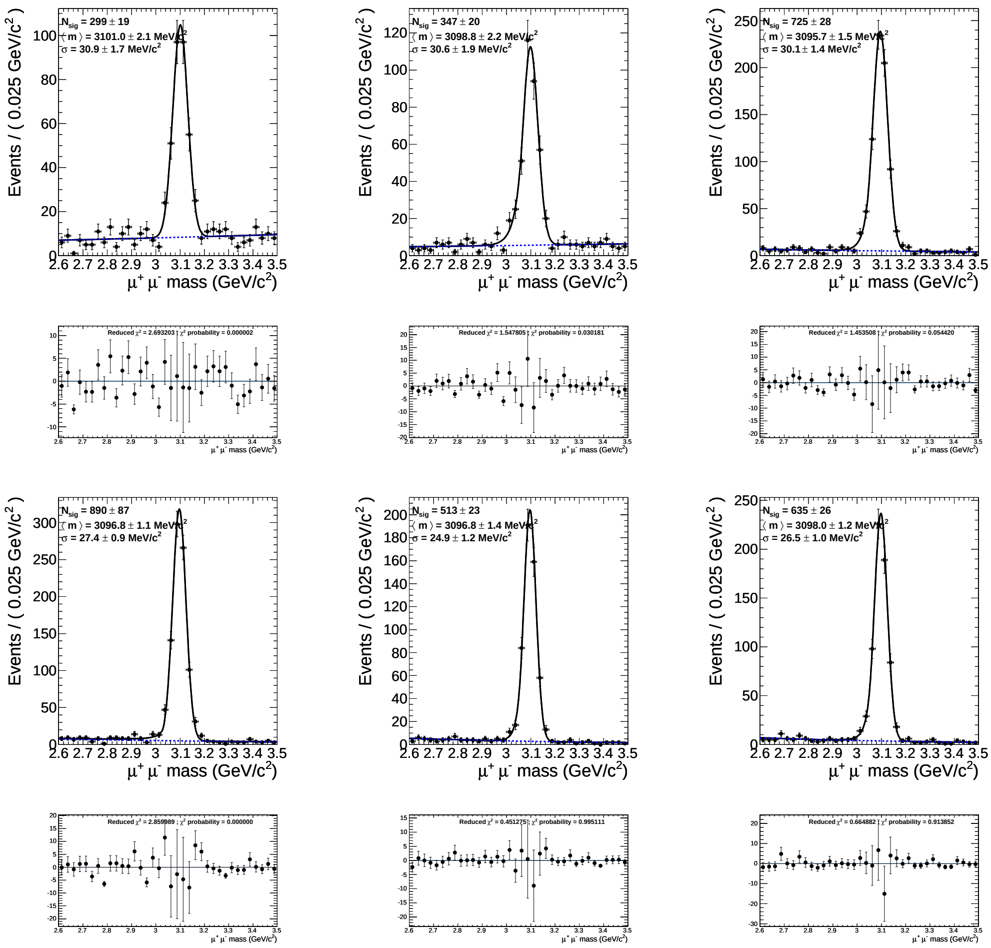

Figure 8.1: J/ψ mass fitted by the Crystal Ball plus Gaussian and exponential function, in the rapidity region $|y^{J/\psi}| < 1.2$ for all transverse momentum regions in Table 8.1. Small plots lower are pull, i.e. the variation between data dots and fitted curve.

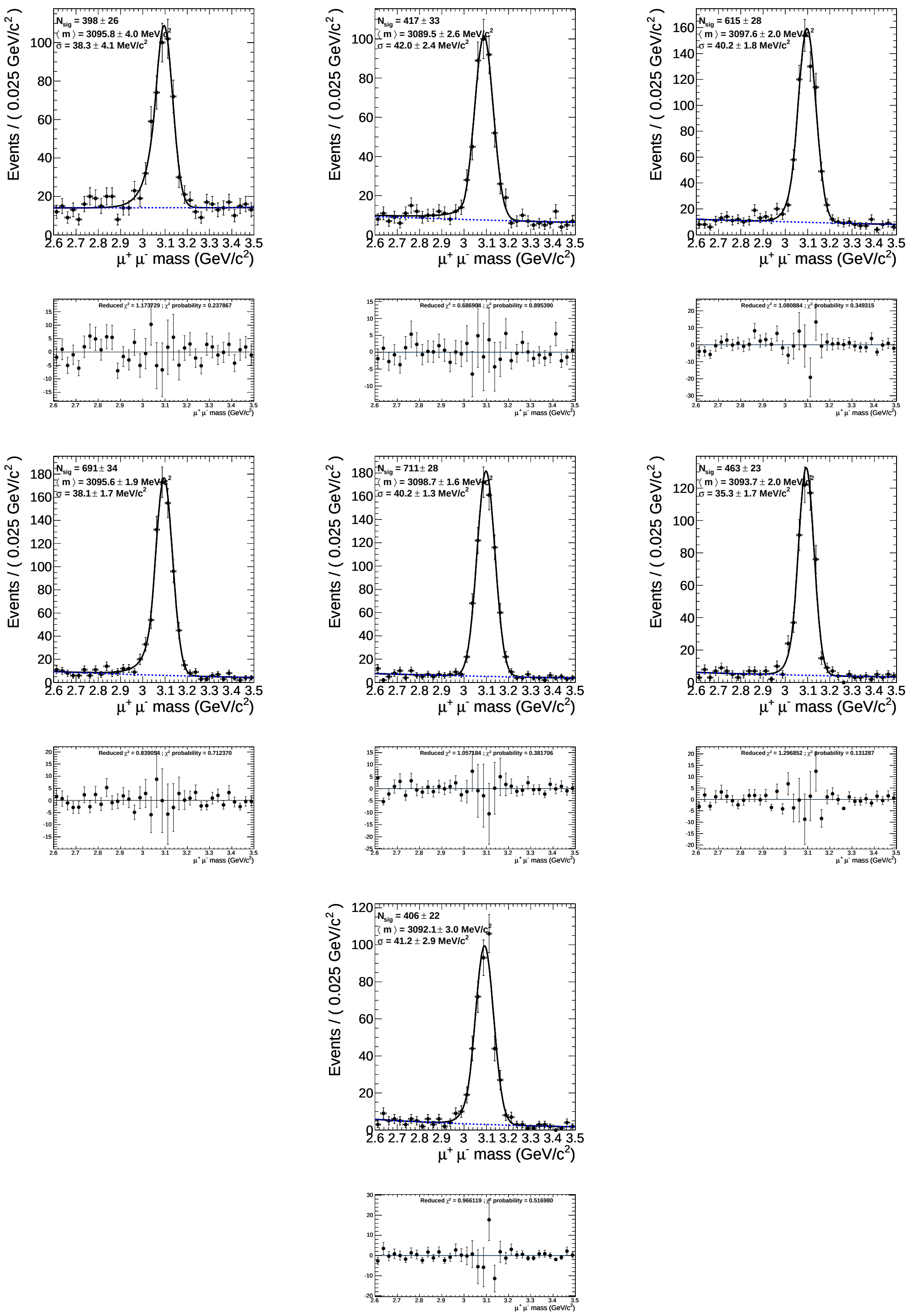

Figure 8.2: J/ψ mass fitted in the rapidity region $1.2 < |y^{J/\psi}| < 1.6$ for all transverse momentum regions in Table 8.1. Other explanations are the same as Fig. 8.1.

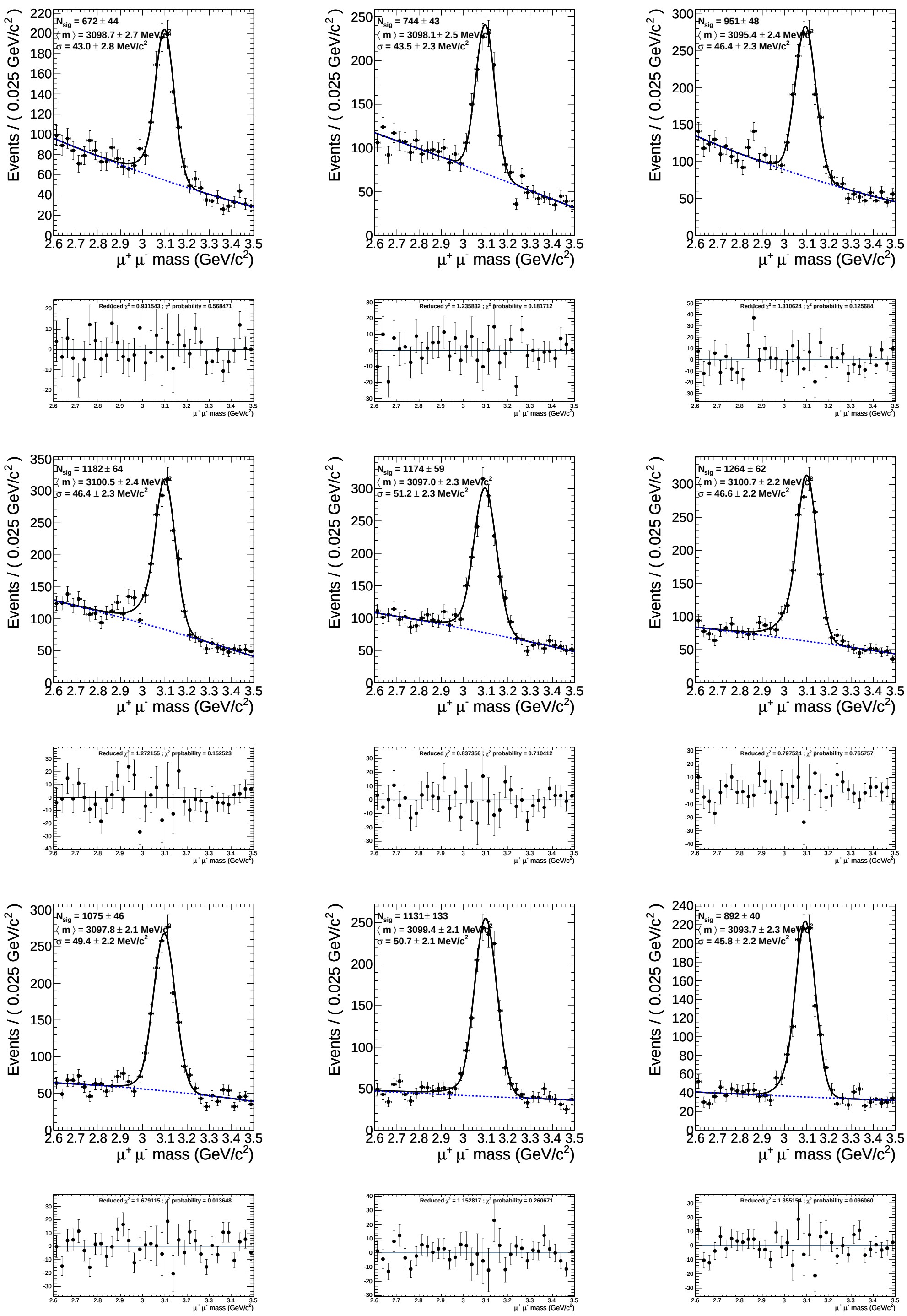

Figure 8.3: J/ψ mass fitted in the rapidity region $1.6 < |y^{J/\psi}| < 2.4$ for the first 9 transverse momentum regions in Table 8.1. Other explanations are the same as Fig. 8.1.

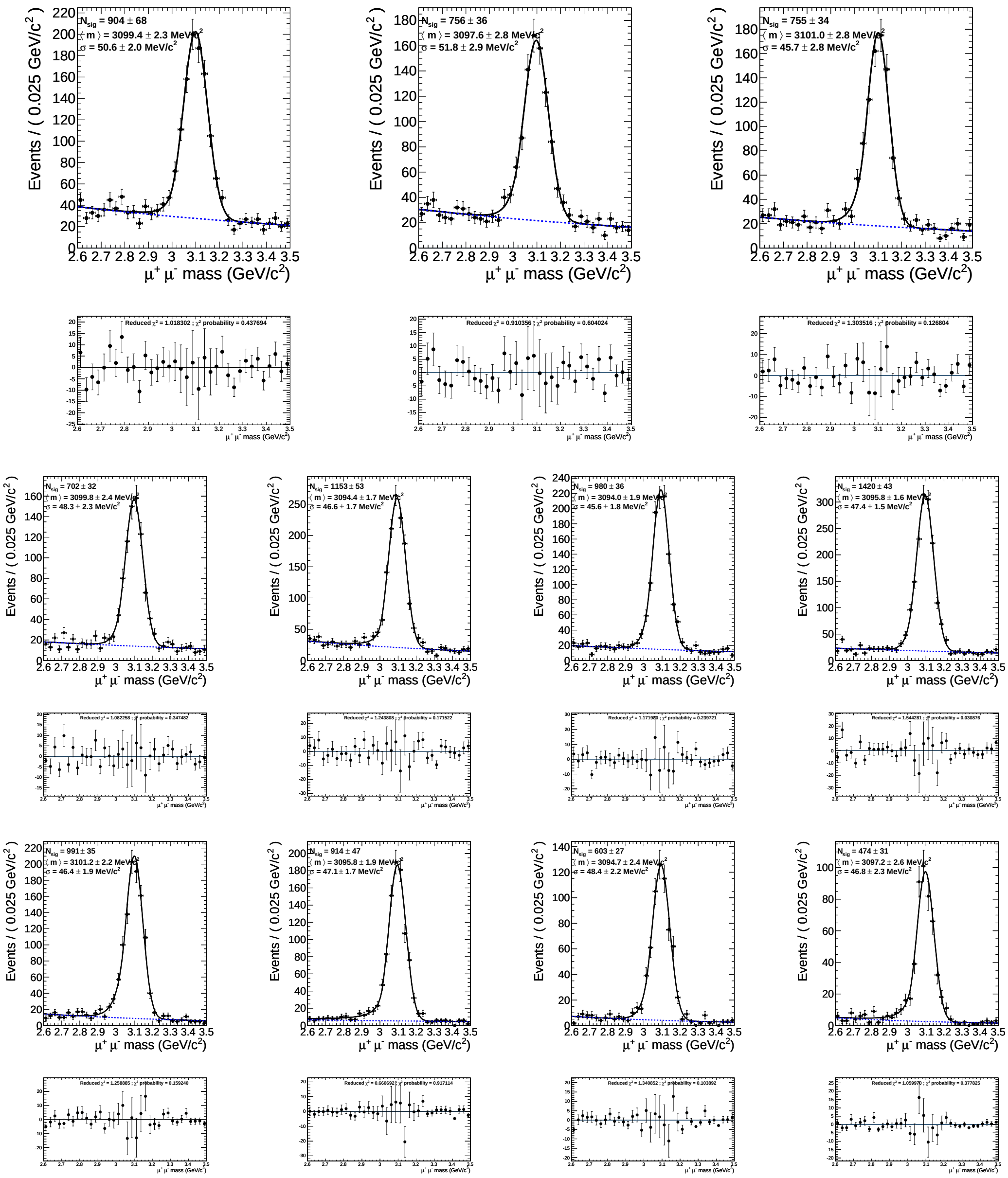

Figure 8.4: J/ψ mass fitted in the rapidity region $1.6 < |y^{J/\psi}| < 2.4$ for the last 11 transverse momentum regions in Table 8.1. Other explanations are the same as Fig. 8.1.

Table 8.1: J/ψ yield in each bin, from Ref. [61], which is approved by CMS collaboration, instead of my own analysis.

$p_T^{J/\psi}(GeV/c)$	Yield	$p_T^{J/\psi}(GeV/c)$	Yield
		$1.6 < \lvert y^{J/\psi}\rvert < 2.4$	
$\lvert y^{J/\psi}\rvert < 1.2$		0.00-0.50	675.6 ± 40.7
		0.50-0.75	829.3 ± 44.7
4.5-5.5	298.7 ± 19.3	0.75-1.00	1006.0 ± 48.8
5.5-6.5	348.7 ± 20.7	1.00-1.25	1216.8 ± 52.8
6.5-8.0	726.5 ± 28.3	1.25-1.50	1232.9 ± 53.7
8.0-10.0	868.1 ± 30.7	1.50-1.75	1252.9 ± 50.3
10.0-12.0	513.2 ± 23.5	1.75-2.00	1132.7 ± 57.5
12.0-30.0	636.0 ± 26.1	2.00-2.25	1122.7 ± 55.0
$1.2 < \lvert y^{J/\psi}\rvert < 1.6$		2.25-2.50	899.9 ± 39.4
		2.50-2.75	903.3 ± 72.4
2.0-3.5	414.9 ± 38.0	2.75-3.00	757.6 ± 36.2
3.5-4.5	401.7 ± 23.2	3.00-3.25	756.1 ± 35.7
4.5-5.5	618.9 ± 28.9	3.25-3.50	703.6 ± 33.6
5.5-6.5	690.9 ± 34.0	3.50-4.00	1150.2 ± 40.0
6.5-8.0	712.0 ± 28.0	4.00-4.50	991.8 ± 35.8
8.0-10.0	463.7 ± 23.3	4.50-5.50	1441.4 ± 42.6
10.0-30.0	406.2 ± 22.4	5.50-6.50	993.0 ± 34.7
		6.50-8.00	900.6 ± 35.1
		8.00-10.00	604.3 ± 26.8
		10.00-30.00	462.6 ± 23.6

C J/ψ mass fit in double Gaussian

The J/ψ mass is re-fitted by the double Gaussian as a signal PDF and polynomial function for the background. The difference between these two parts of fit are systematic uncertainties.

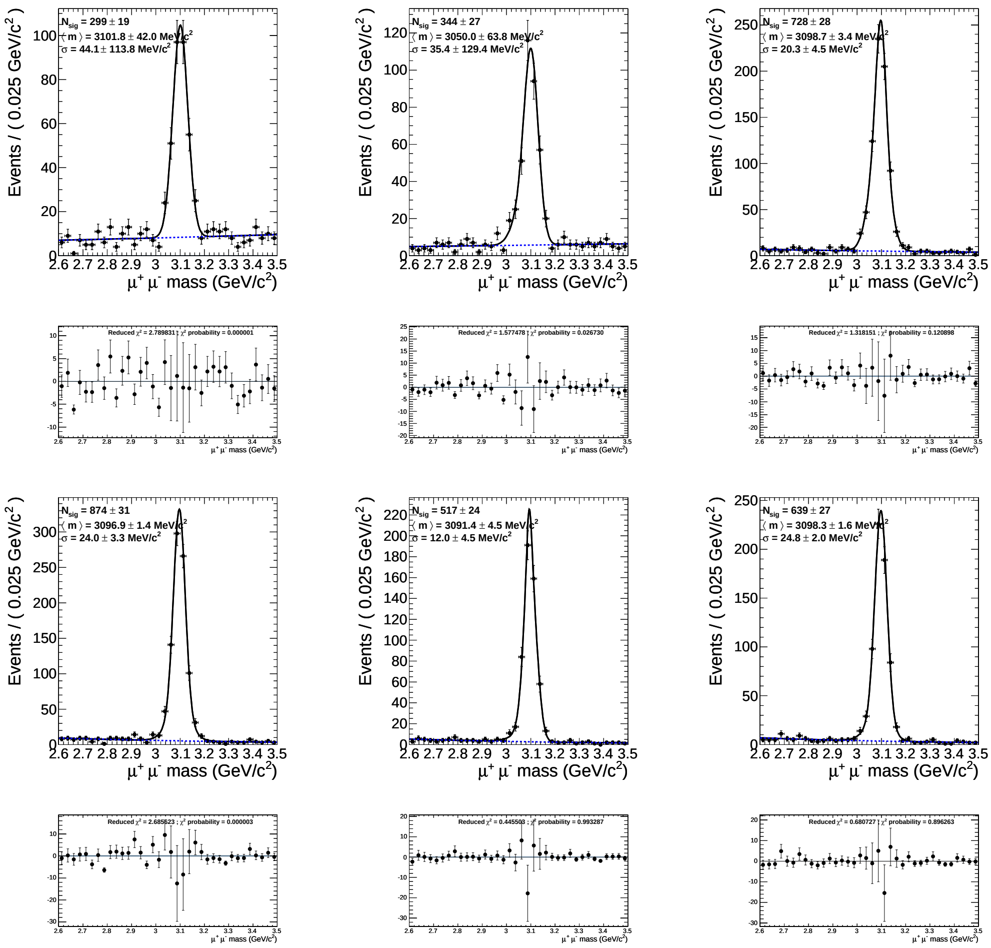

Figure 8.5: J/ψ mass fitted by the double Gaussian and exponential function, in the rapidity region $|y^{J/\psi}| < 1.2$ for all transverse momentum regions. Other explanations are the same as Fig. 8.1.

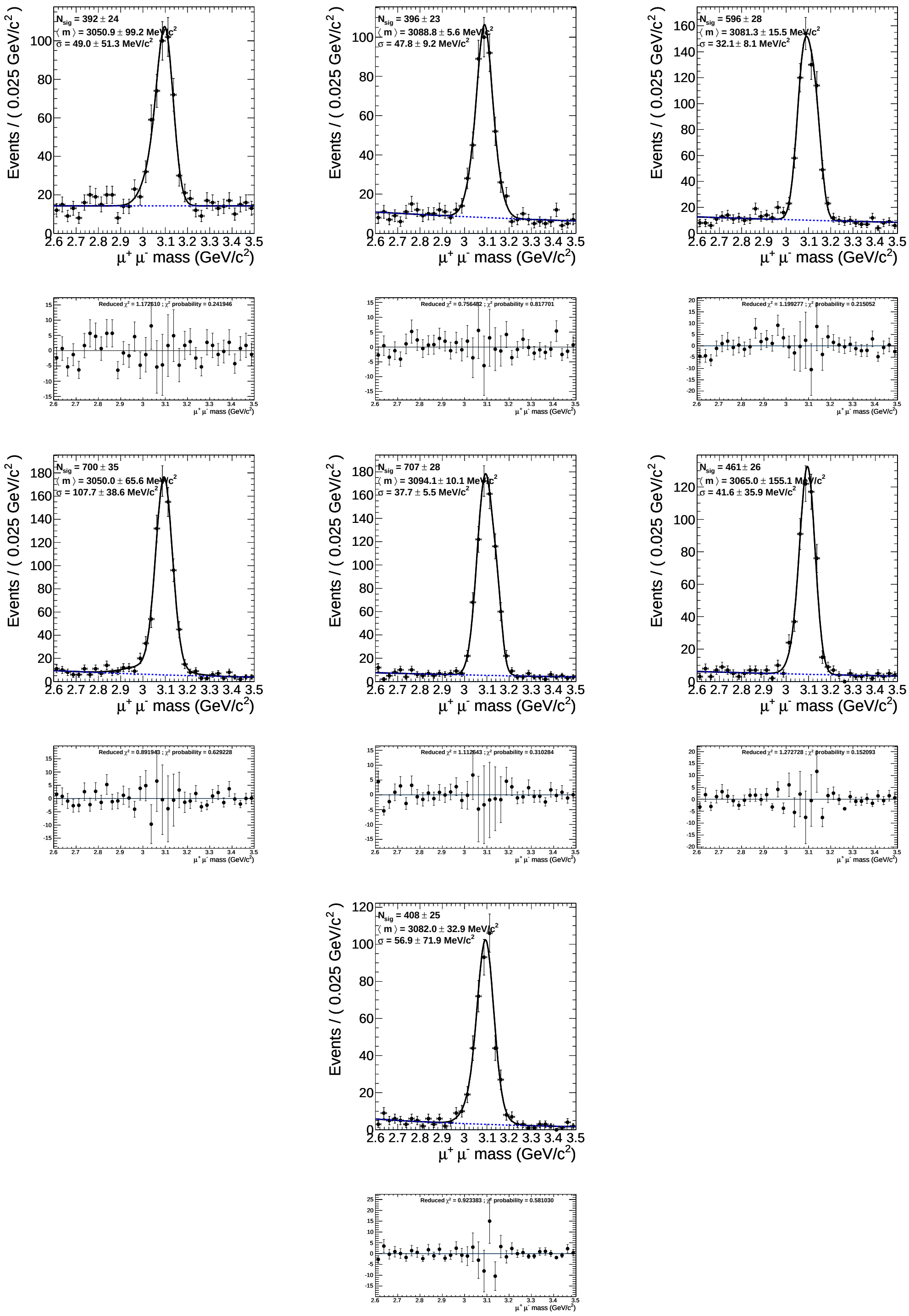

Figure 8.6: J/ψ mass fitted in the rapidity region $1.2 < |y^{J/\psi}| < 1.6$ for all transverse momentum regions. Other explanations are the same as Fig. 8.1.

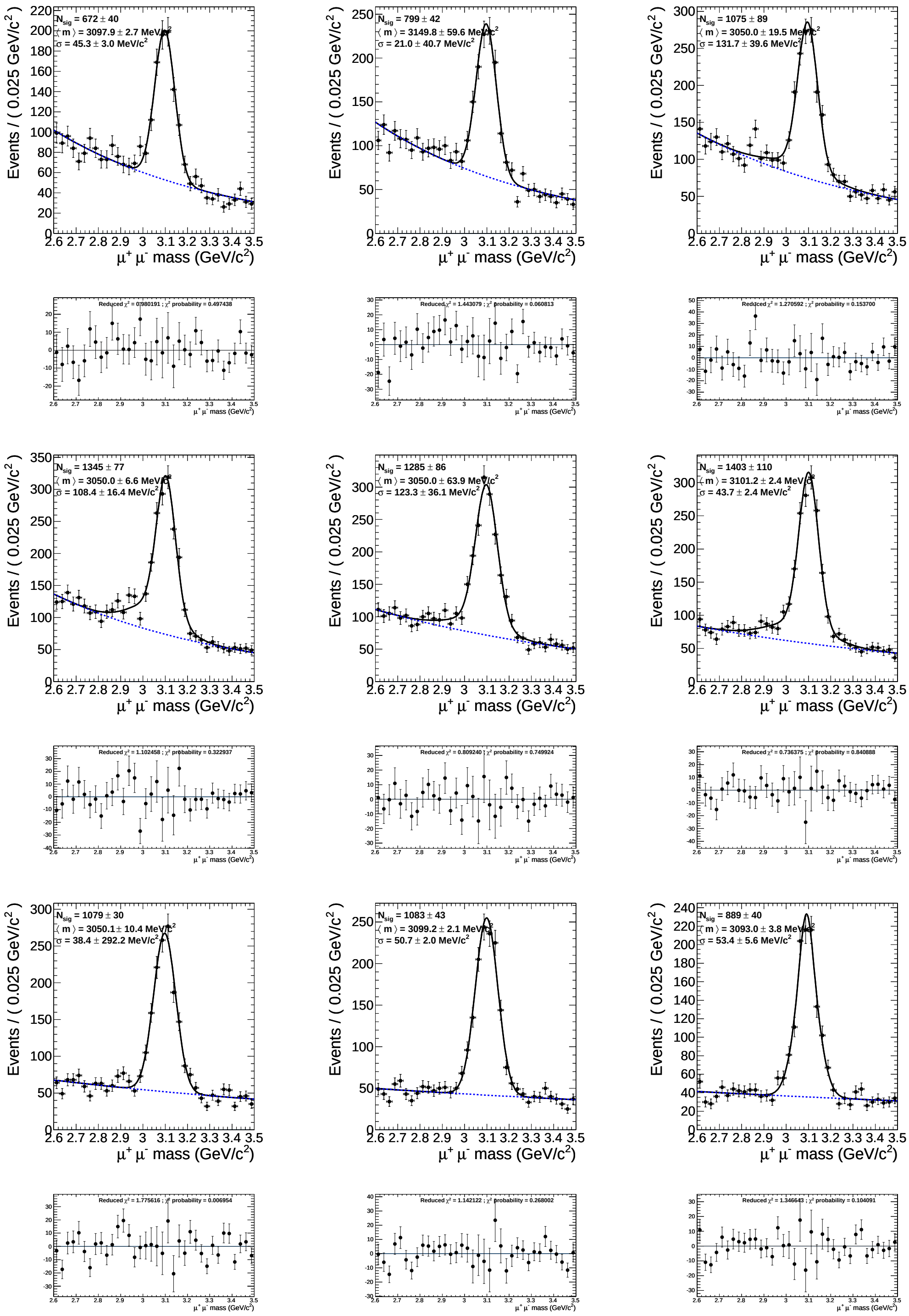

Figure 8.7: J/ψ mass fitted in the rapidity region $1.6 < |y^{J/\psi}| < 2.4$ for the first 9 transverse momentum regions. Other explanations are the same as Fig. 8.1.

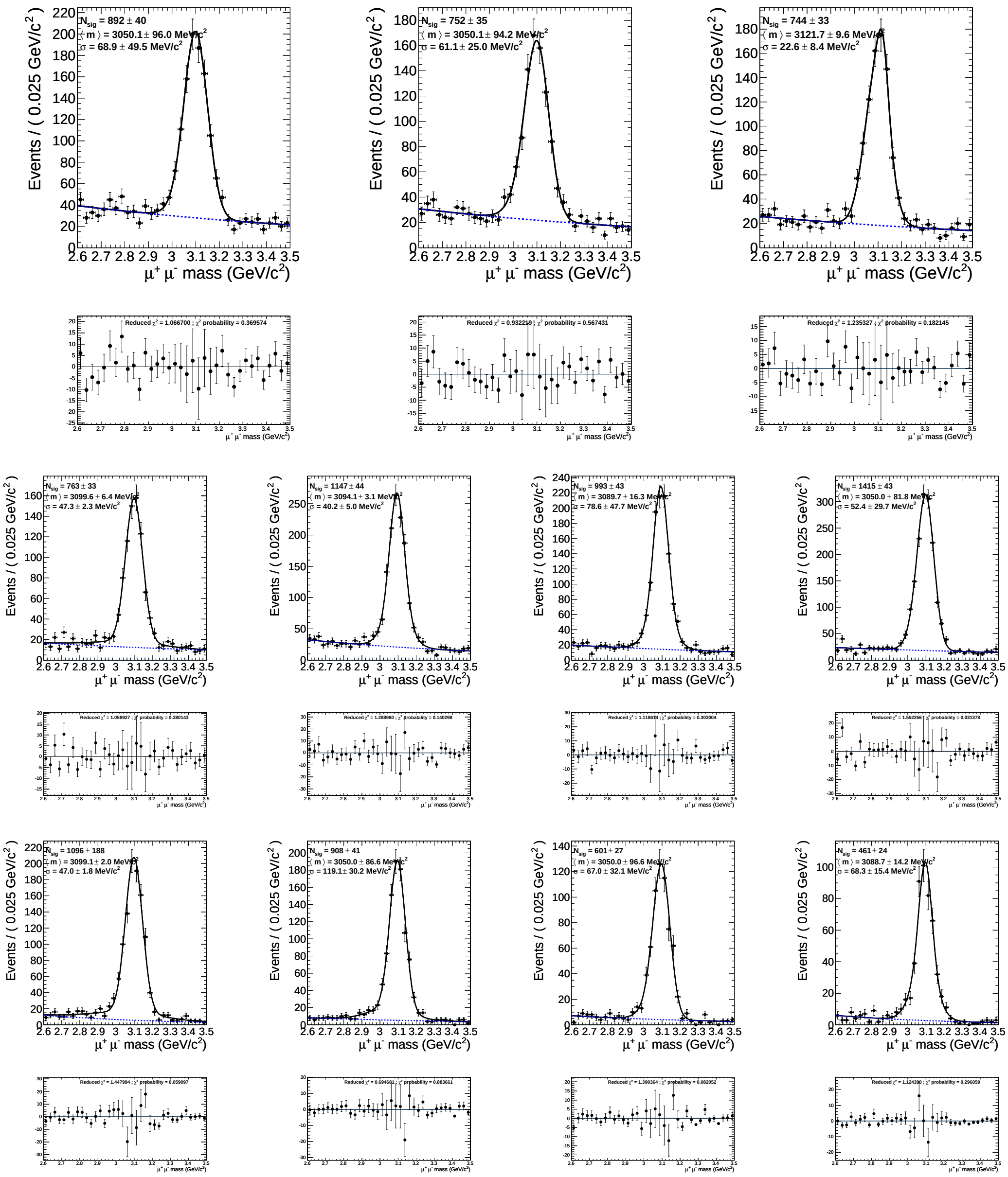

Figure 8.8: J/ψ mass fitted in the rapidity region $1.6 < |y^{J/\psi}| < 2.4$ for the last 11 transverse momentum regions. Other explanations are the same as Fig. 8.1.

D J/ψ lifetime fit

Here the J/ψ lifetime in each p_T and y bin is fitted. The plots at left are the mass components of the 2D mass-lifetime fit, middle ones are the lifetime of the 2D mass-lifetime fit in linear scale and the right plots are the lifetime of the 2D mass-lifetime fit in logarithmic scale.

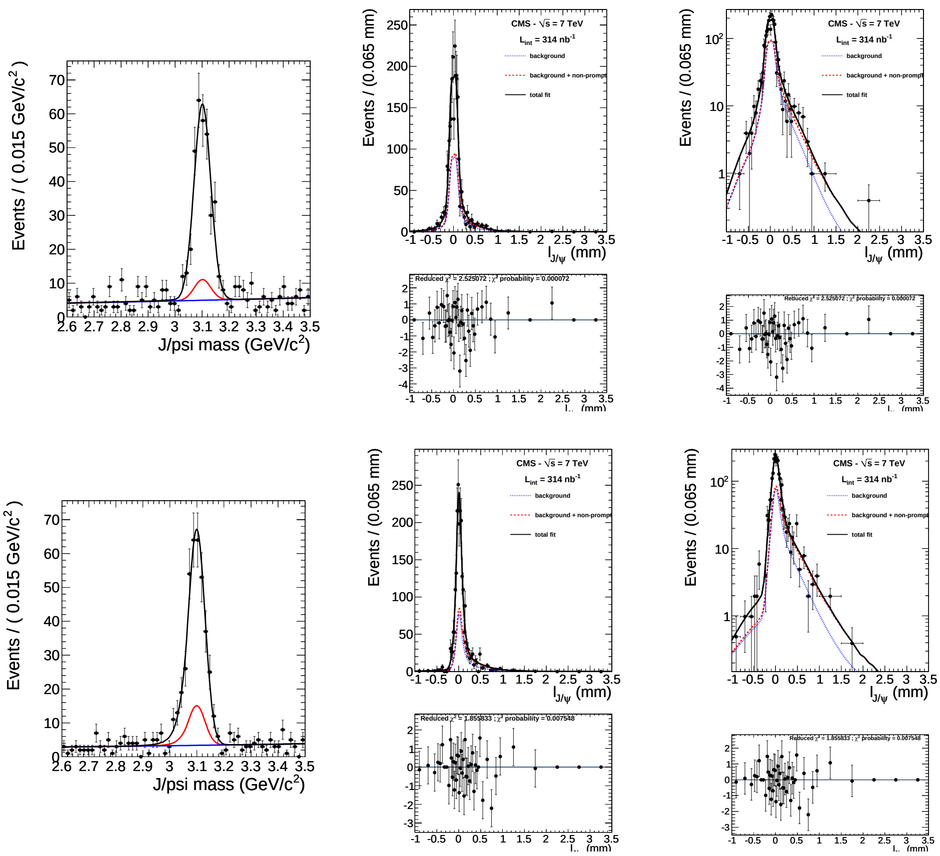

Figure 8.9: J/ψ mass-lifetime 2D fitted in transverse momentum of $4.5 < p_T^{J/\psi} < 5.5$ GeV/c (upper) and $5.5 < p_T^{J/\psi} < 6.5$ GeV/c (bottom), both are in rapidity of $|y^{J/\psi}| < 1.2$.

Table 8.2: The b-fraction in each bin.

$p_T^{J/\psi}(GeV/c)$	B-fraction	$p_T^{J/\psi}(GeV/c)$	b-fraction
		$1.6 < \|y^{J/\psi}\| < 2.4$	
$\|y^{J/\psi}\| < 1.2$		0.00-0.50	$13.7 \pm 3.5\%$
		0.50-0.75	$1.1 \pm 3.1\%$
4.5-5.5	$10.6 \pm 3.0\%$	0.75-1.00	$1.2 \pm 5.4\%$
5.5-6.5	$18.4 \pm 2.8\%$	1.00-1.25	$9.6 \pm 2.1\%$
6.5-8.0	$20.7 \pm 1.8\%$	1.25-1.50	$9.5 \pm 2.0\%$
8.0-10.0	$29.8 \pm 1.7\%$	1.50-1.75	$8.1 \pm 1.8\%$
10.0-12.0	$36.0 \pm 2.3\%$	1.75-2.00	$8.7 \pm 1.7\%$
12.0-30.0	$43.2 \pm 2.0\%$	2.00-2.25	$6.1 \pm 1.7\%$
$1.2 < \|y^{J/\psi}\| < 1.6$		2.25-2.50	$3.7 \pm 1.8\%$
		2.50-2.75	$11.3 \pm 1.9\%$
2.0-3.5	$9.3 \pm 2.7\%$	2.75-3.00	$11.2 \pm 2.0\%$
3.5-4.5	$2.4 \pm 9.4\%$	3.00-3.25	$9.3 \pm 1.8\%$
4.5-5.5	$13.5 \pm 2.0\%$	3.25-3.50	$14.7 \pm 2.1\%$
5.5-6.5	$17.4 \pm 2.0\%$	3.50-4.00	$10.0 \pm 1.5\%$
6.5-8.0	$18.7 \pm 1.9\%$	4.00-4.50	$16.3 \pm 1.7\%$
8.0-10.0	$18.0 \pm 2.3\%$	4.50-5.50	$17.6 \pm 1.4\%$
10.0-30.0	$34.4 \pm 2.7\%$	5.50-6.50	$16.0 \pm 1.5\%$
		6.50-8.00	$22.3 \pm 1.8\%$
		8.00-10.00	$25.4 \pm 2.1\%$
		10.00-30.00	$38.0 \pm 2.6\%$

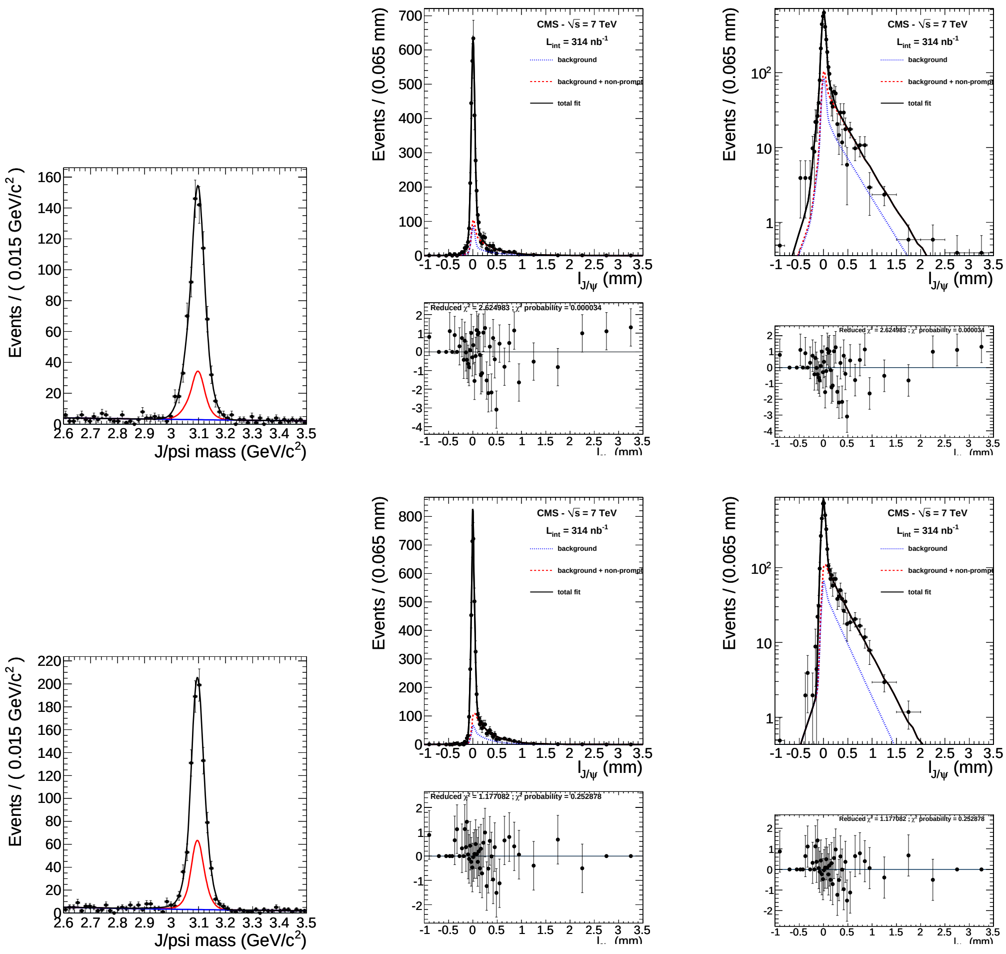

Figure 8.10: J/ψ mass-lifetime 2D fitted in $6.5 < p_T^{J/\psi} < 8.0$ GeV/c (upper) and $8.0 < p_T^{J/\psi} < 10.0$ GeV/c (bottom), and the rapidity region is $|y^{J/\psi}| < 1.2$.

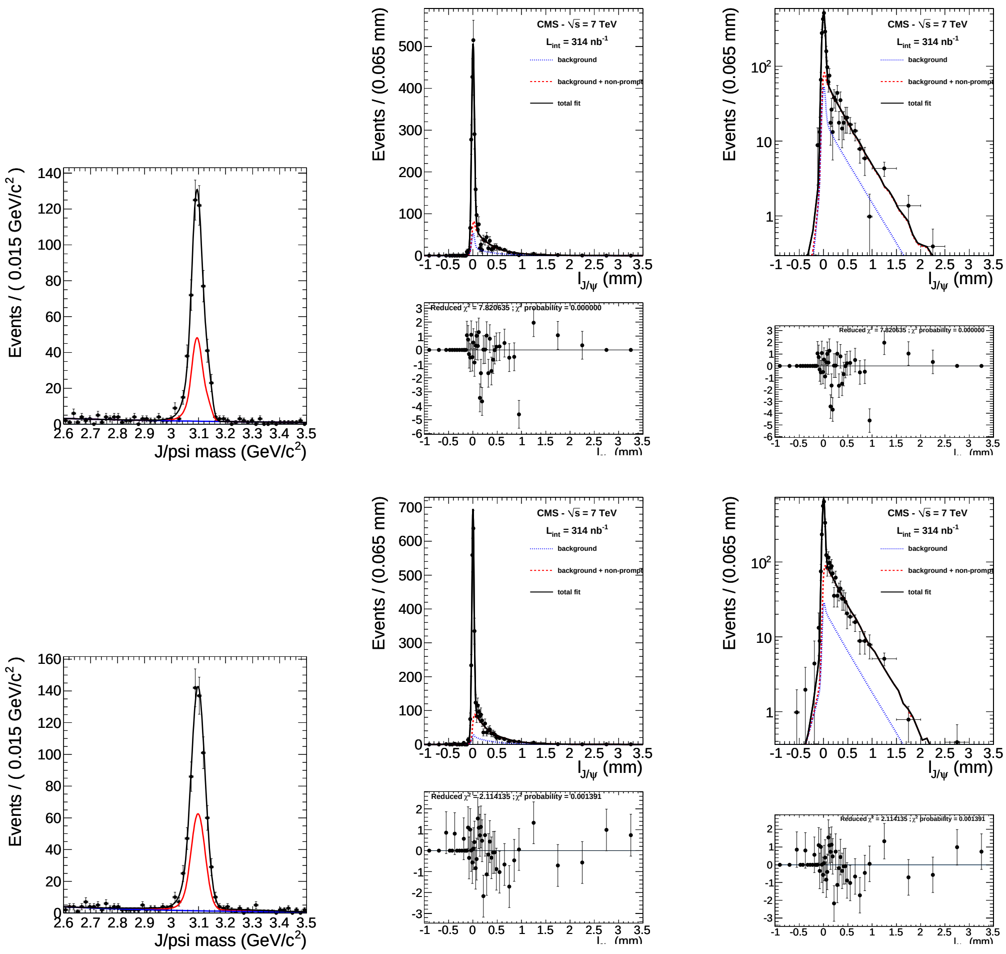

Figure 8.11: J/ψ mass-lifetime 2D fitted in $10.0 < p_T^{J/\psi} < 12.0$ GeV/c (upper) and $12.0 < p_T^{J/\psi} < 30.0$ GeV/c (bottom), and the rapidity region is $|y^{J/\psi}| < 1.2$.

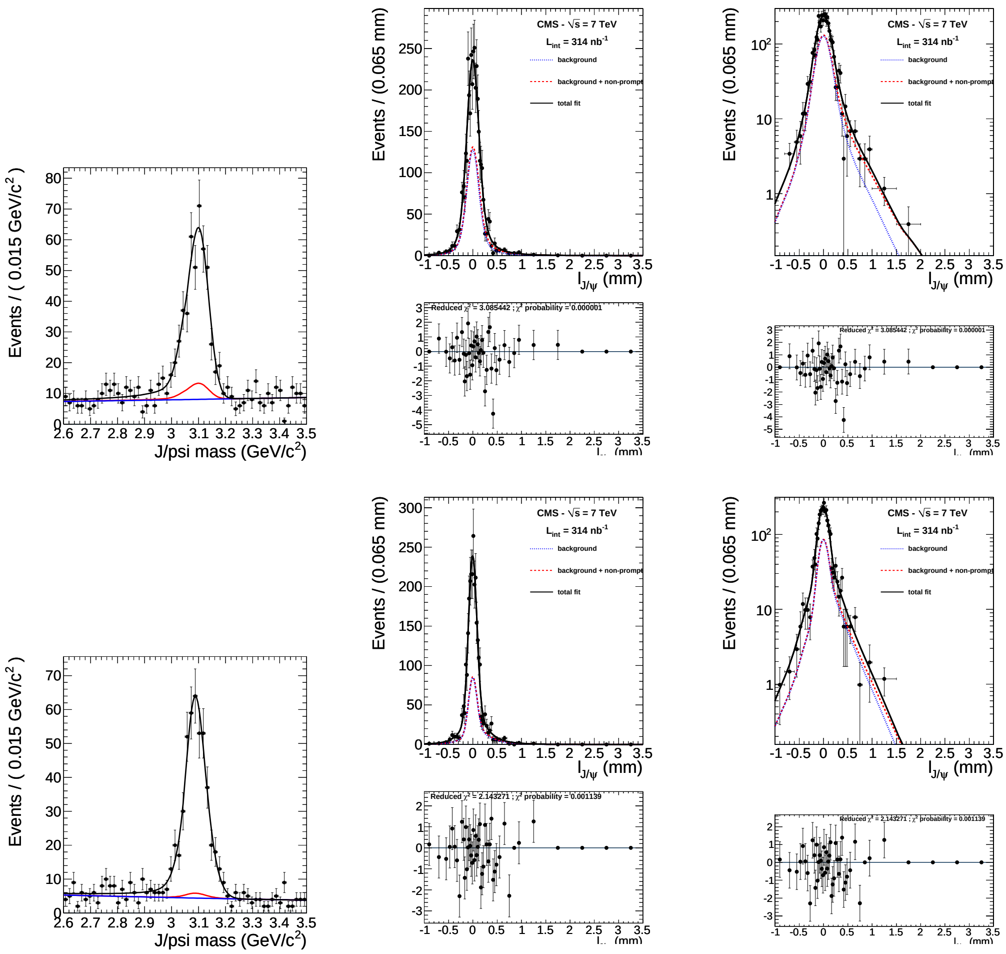

Figure 8.12: J/ψ mass-lifetime 2D fitted in $2.0 < p_T^{J/\psi} < 3.5$ GeV/c (upper) and $3.5 < p_T^{J/\psi} < 4.5$ GeV/c (bottom), and the rapidity region is $1.2 < |y^{J/\psi}| < 1.6$.

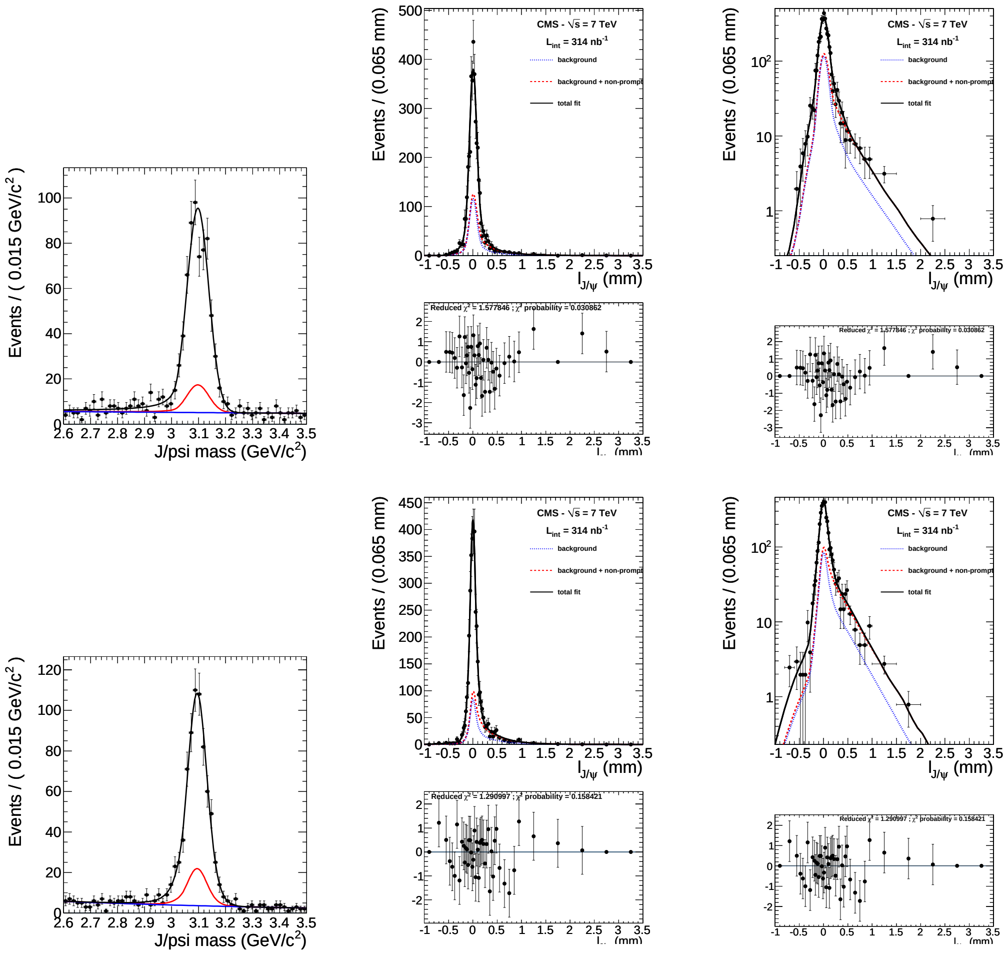

Figure 8.13: J/ψ mass-lifetime 2D fitted in $4.5 < p_T^{J/\psi} < 5.5$ GeV/c (upper) and $5.5 < p_T^{J/\psi} < 6.5$ GeV/c (bottom), and the rapidity region is $1.2 < |y^{J/\psi}| < 1.6$.

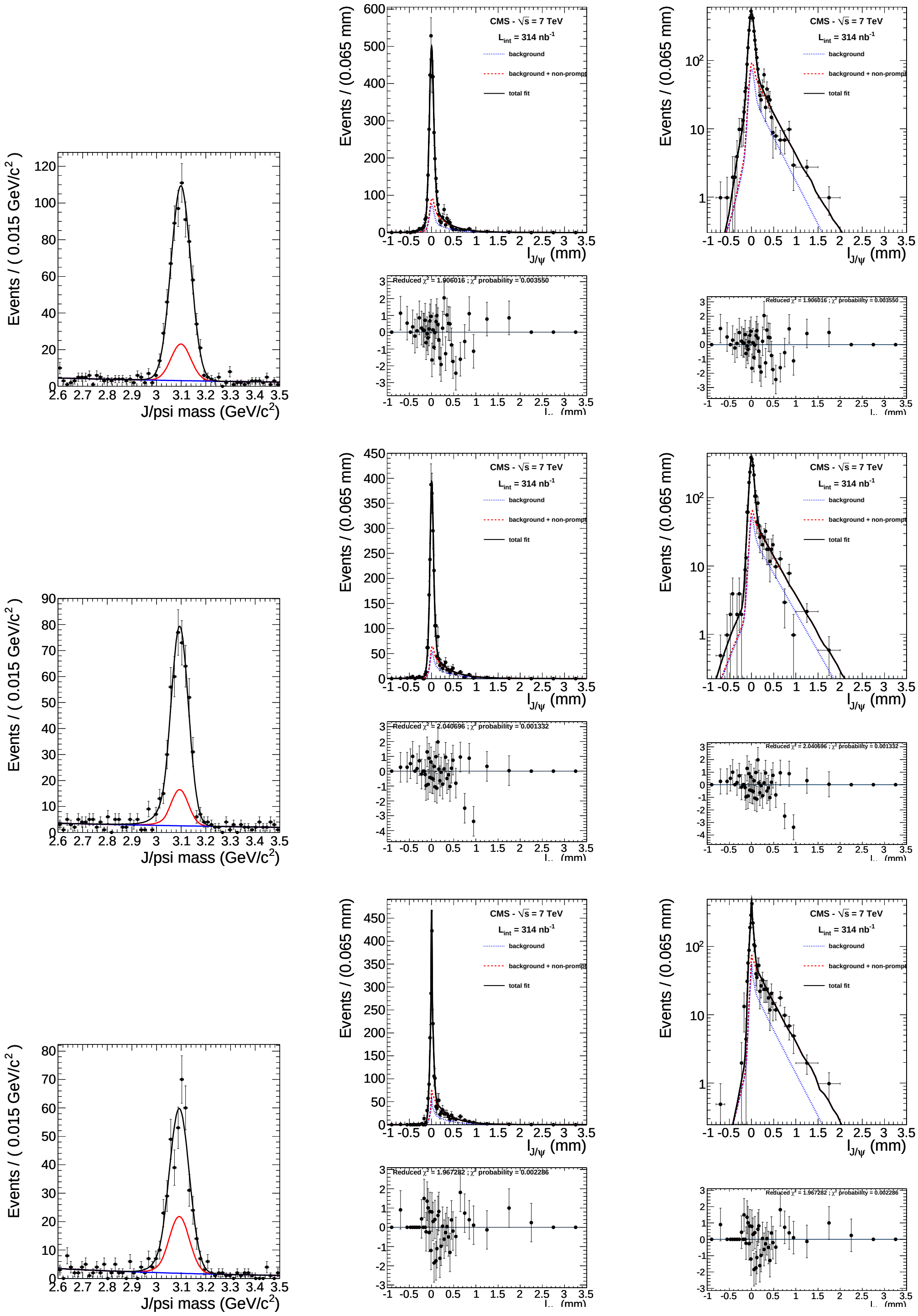

Figure 8.14: J/ψ mass-lifetime 2D fitted in $6.5 < p_T^{J/\psi} < 8.0$ GeV/c (upper), $8.0 < p_T^{J/\psi} < 10.0$ GeV/c (middle) and $10.0 < p_T^{J/\psi} < 30.0$ GeV/c (bottom), and the rapidity region is $1.2 < |y^{J/\psi}| < 1.6$.

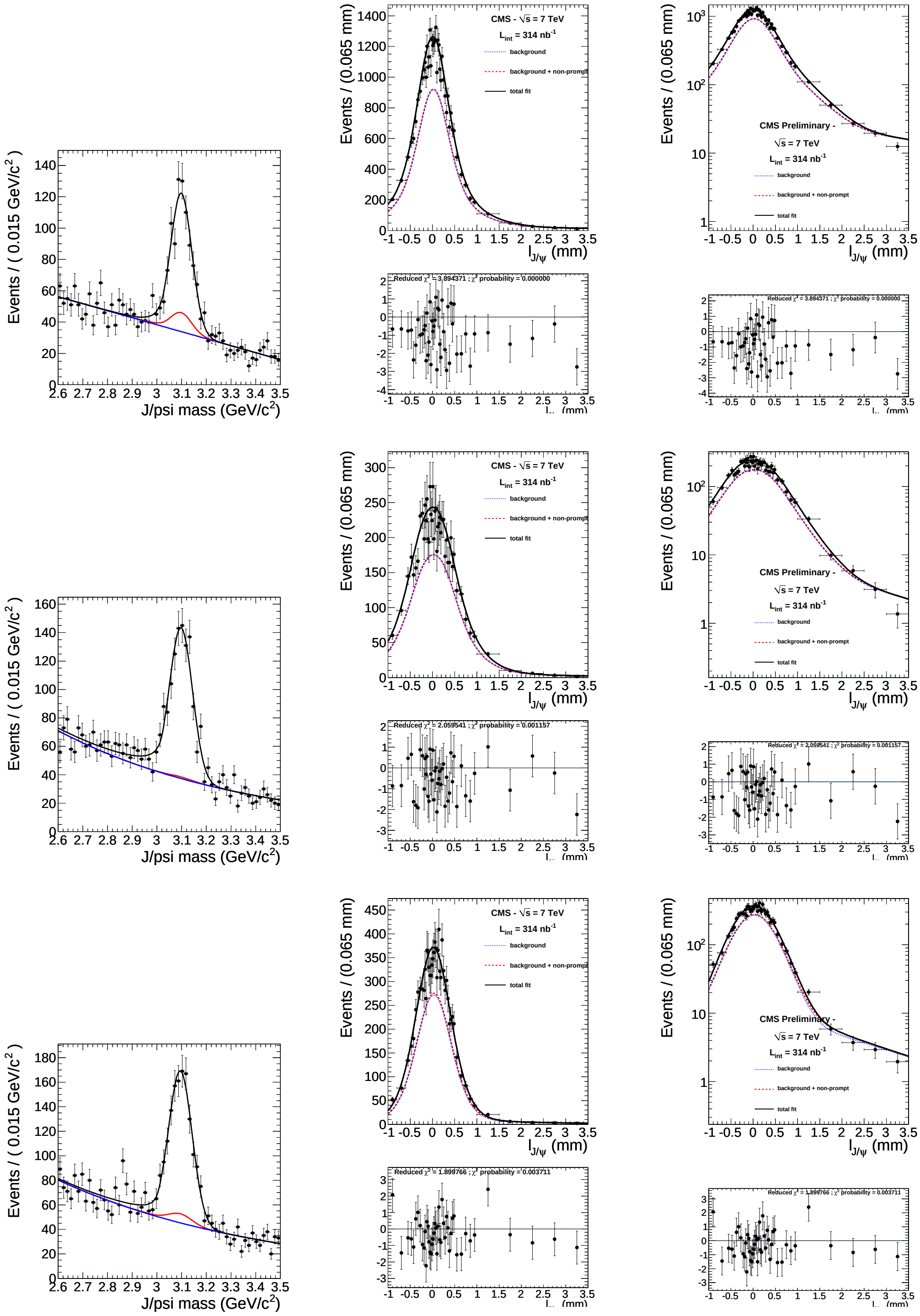

Figure 8.15: J/ψ mass-lifetime 2D fitted in $p_T^{J/\psi} < 0.50$ GeV/c (upper), $0.50 < p_T^{J/\psi} < 0.75$ GeV/c (middle) and $0.75 < p_T^{J/\psi} < 1.00$ GeV/c (bottom), and the rapidity region is $1.6 < |y^{J/\psi}| < 2.4$.

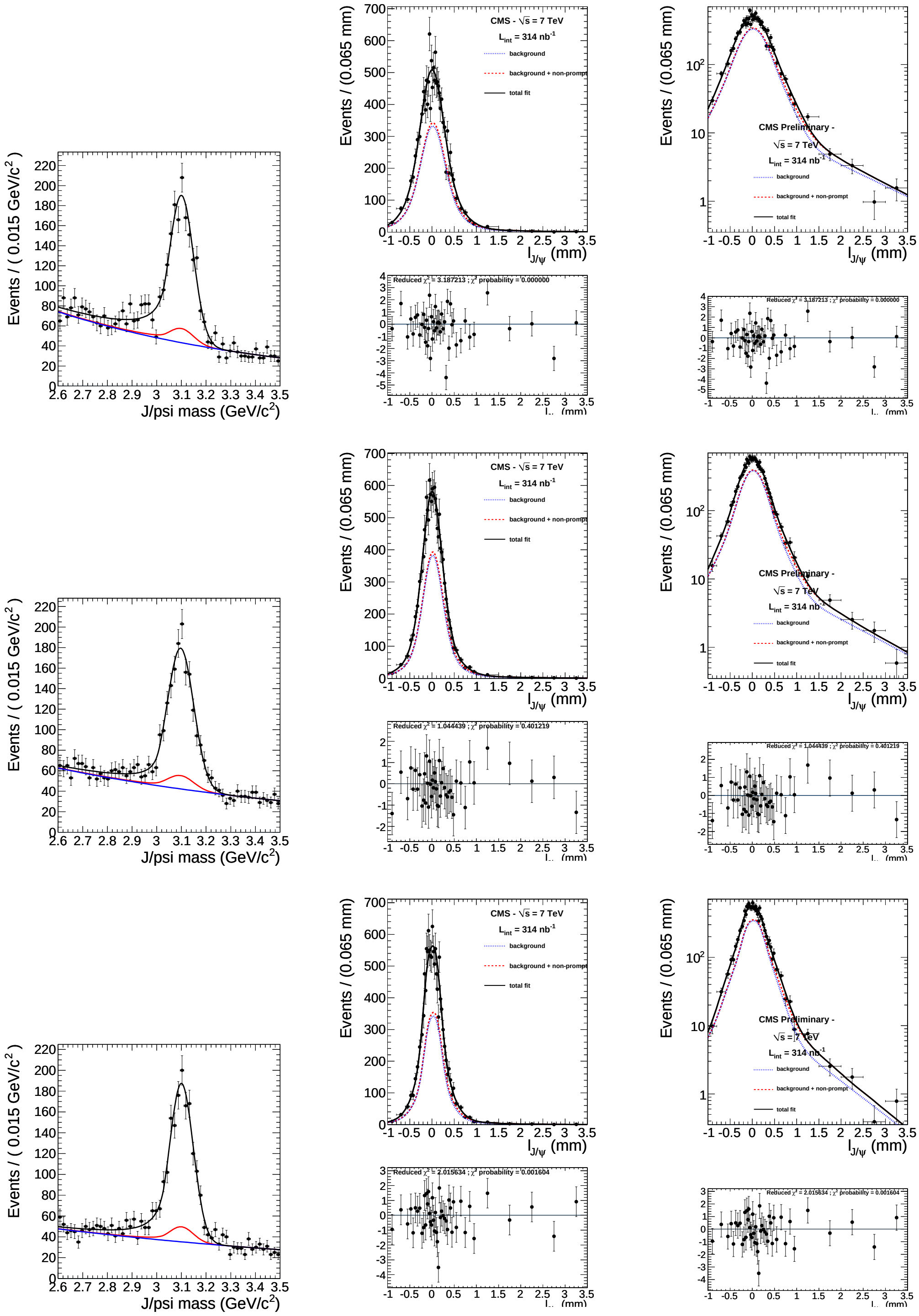

Figure 8.16: J/ψ mass-lifetime 2D fitted in $1.00 < p_T^{J/\psi} < 1.25$ GeV/c (upper), $1.25 < p_T^{J/\psi} < 1.50$ GeV/c (middle) and $1.50 < p_T^{J/\psi} < 1.75$ GeV/c (bottom), and the rapidity region is $1.6 < |y^{J/\psi}| < 2.4$.

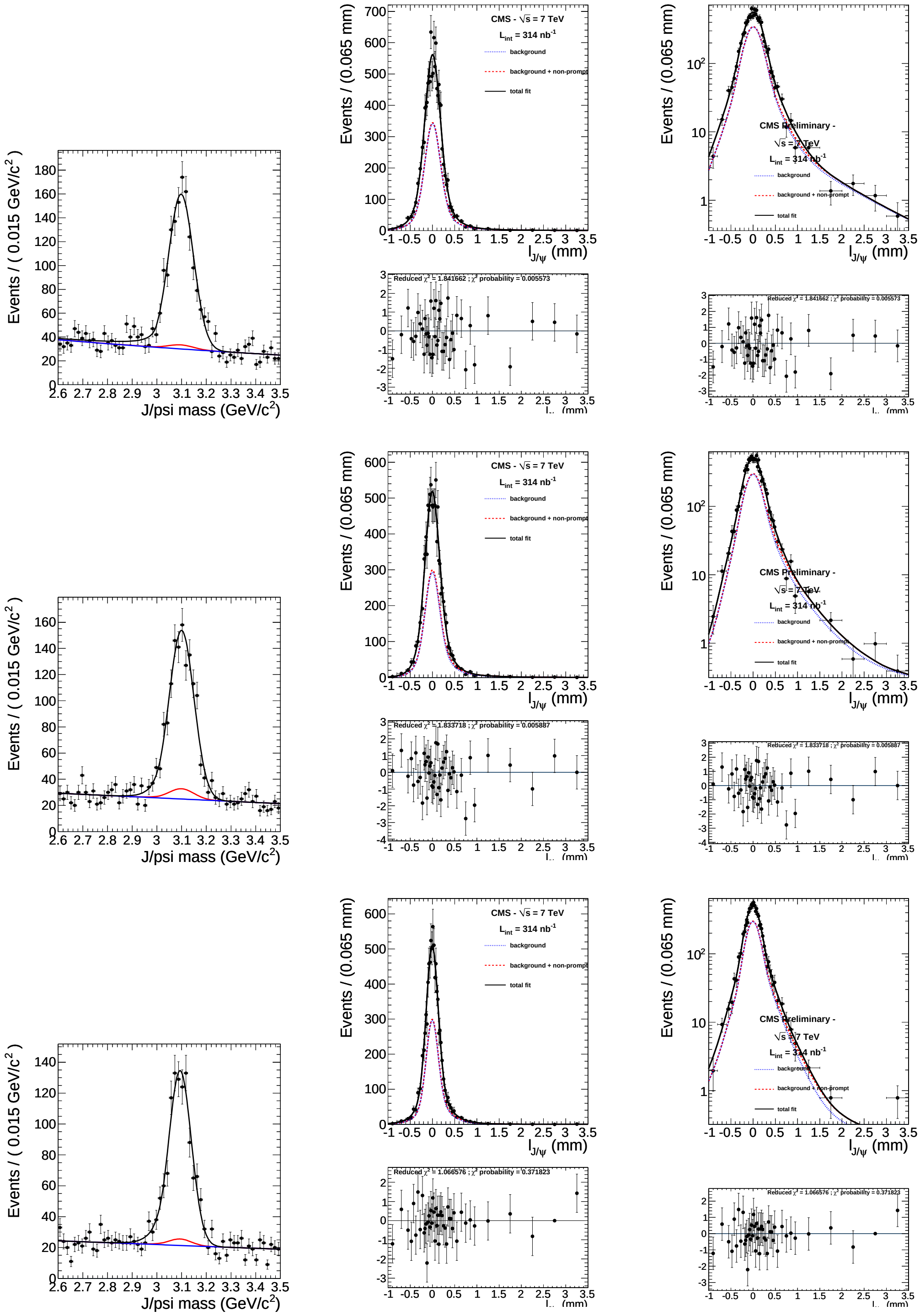

Figure 8.17: J/ψ mass-lifetime 2D fitted in $1.75 < p_T^{J/\psi} < 2.00$ GeV/c (upper), $2.00 < p_T^{J/\psi} < 2.25$ GeV/c (middle) and $2.25 < p_T^{J/\psi} < 2.50$ GeV/c (bottom), and the rapidity region is $1.6 < |y^{J/\psi}| < 2.4$.

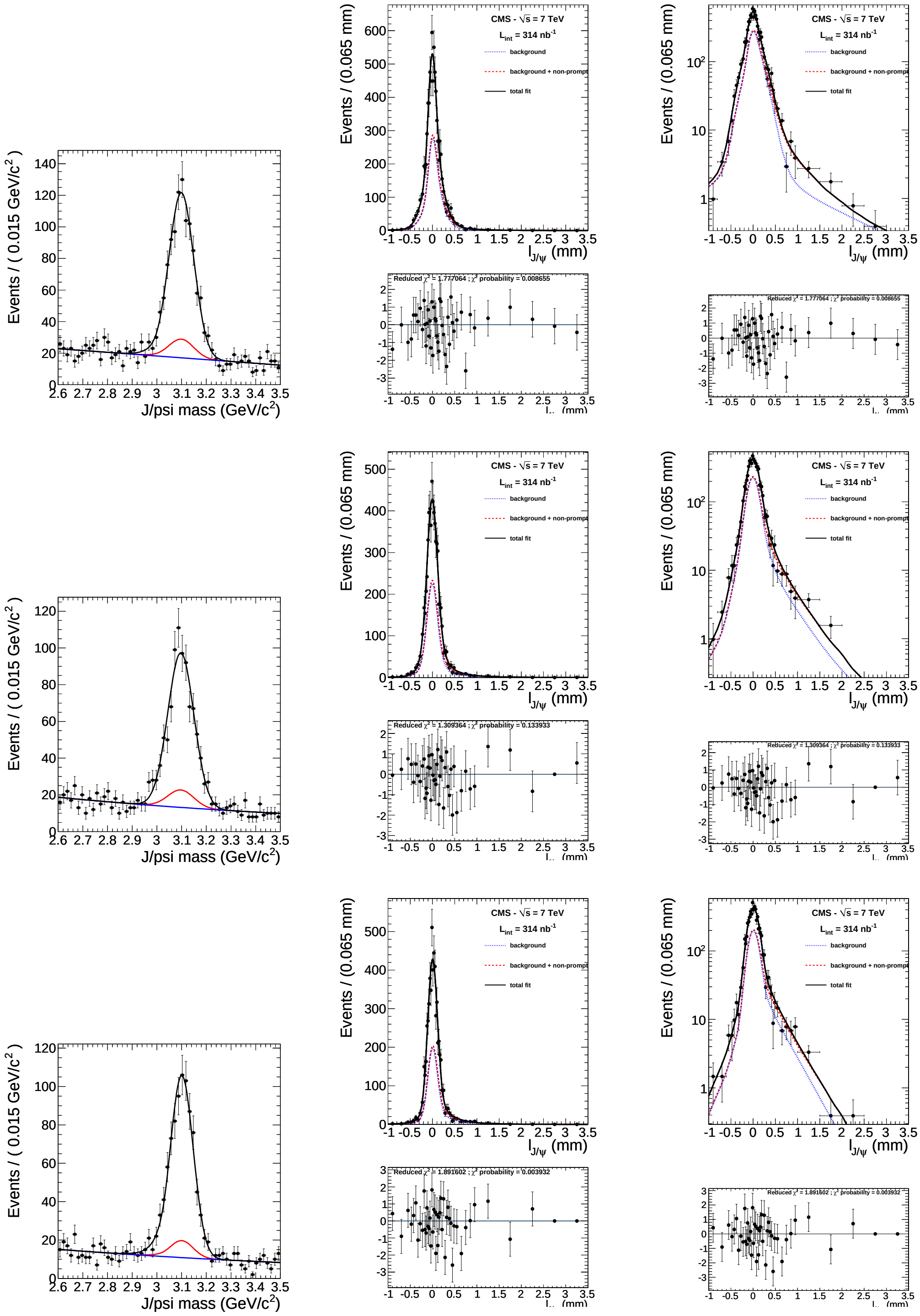

Figure 8.18: J/ψ mass-lifetime 2D fitted in $2.50 < p_T^{J/\psi} < 2.75$ GeV/c (upper), $2.75 < p_T^{J/\psi} < 3.00$ GeV/c (middle) and $3.00 < p_T^{J/\psi} < 3.25$ GeV/c (bottom), and the rapidity region is $1.6 < |y^{J/\psi}| < 2.4$.

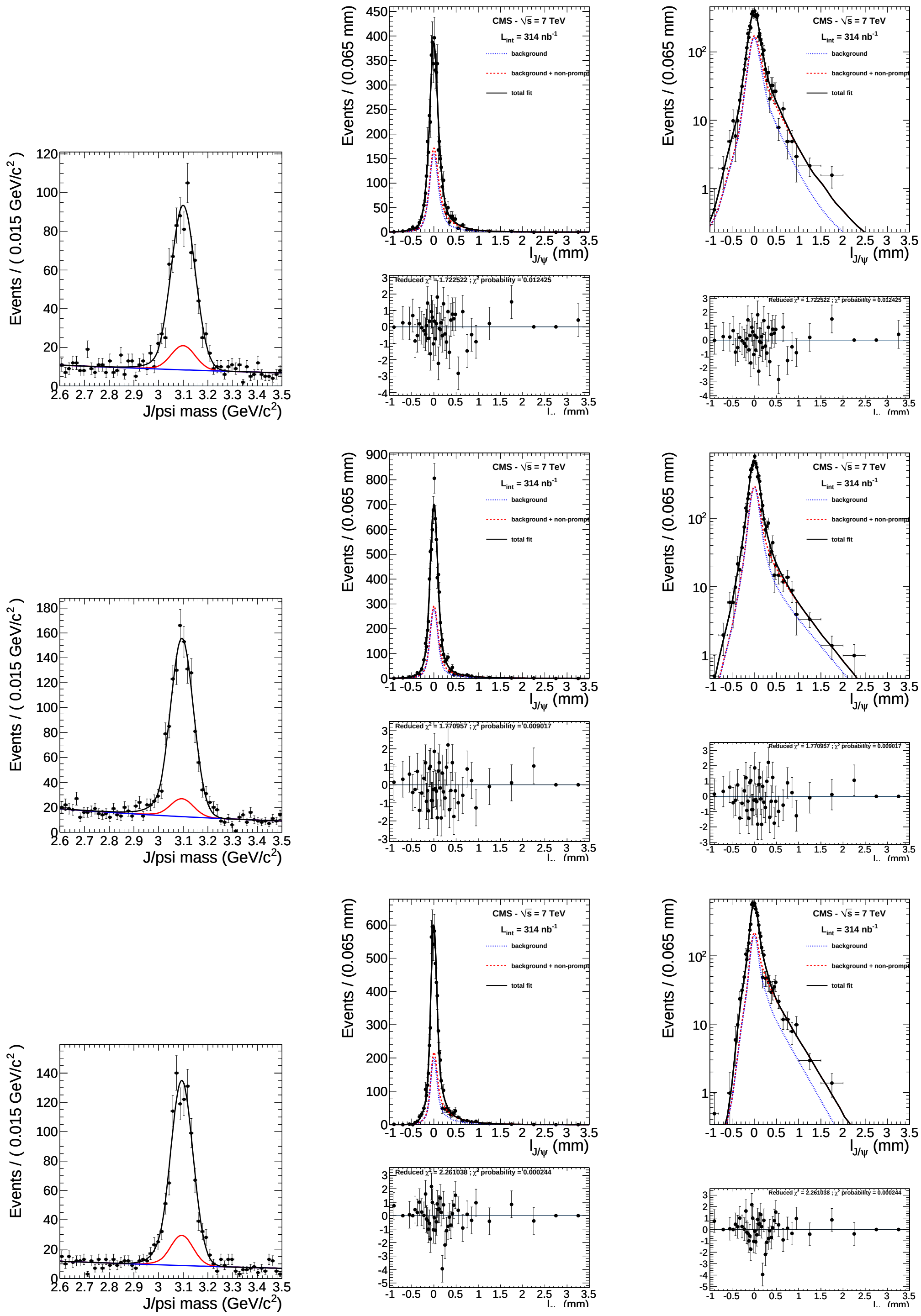

Figure 8.19: J/ψ mass-lifetime 2D fitted in $3.25 < p_T^{J/\psi} < 3.50$ GeV/c (upper), $3.50 < p_T^{J/\psi} < 4.00$ GeV/c (middle) and $4.00 < p_T^{J/\psi} < 4.50$ GeV/c (bottom), and the rapidity region is $1.6 < |y^{J/\psi}| < 2.4$.

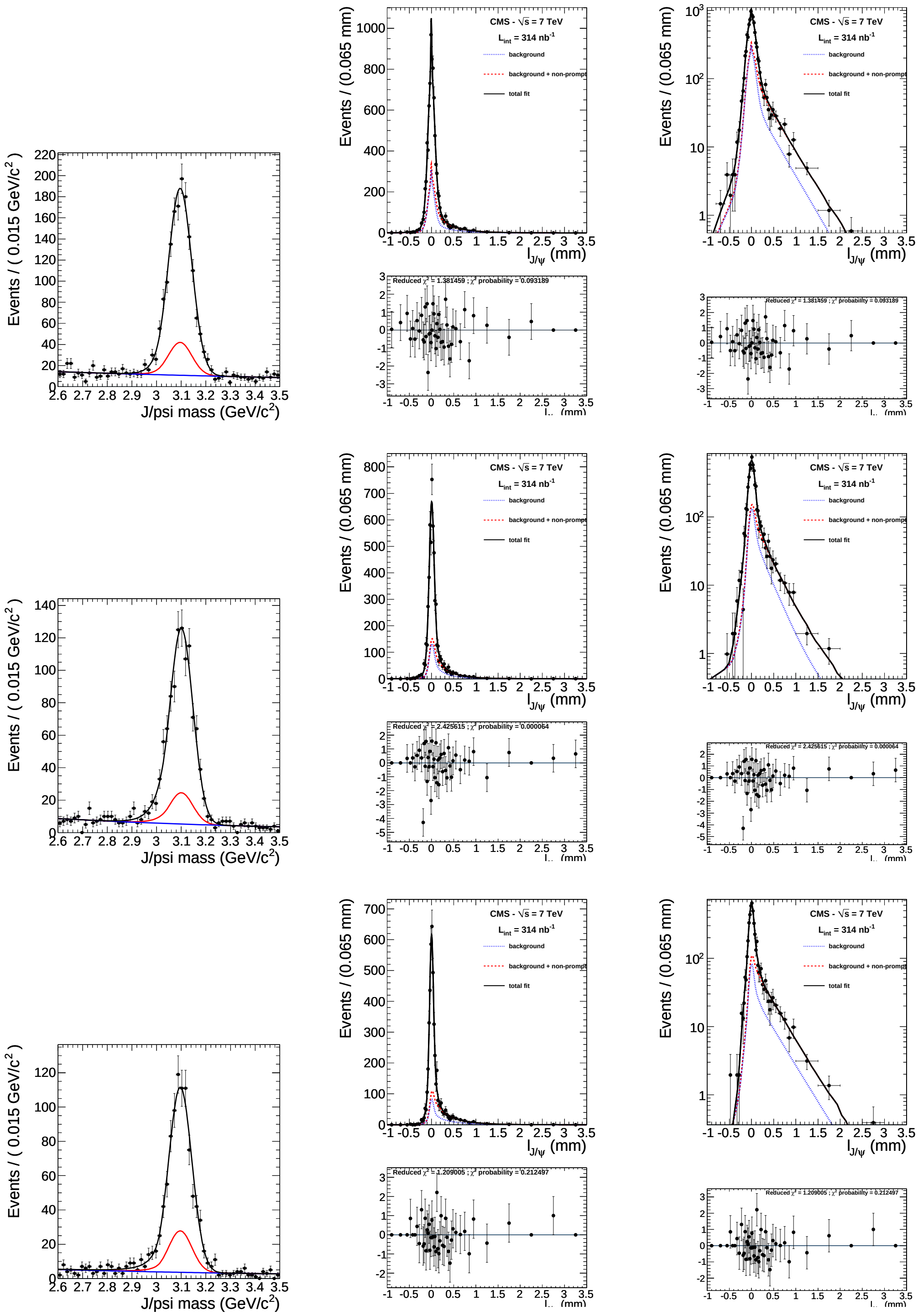

Figure 8.20: J/ψ mass-lifetime 2D fitted in $4.50 < p_T^{J/\psi} < 5.50$ GeV/c (upper), $5.50 < p_T^{J/\psi} < 6.50$ GeV/c (middle) and $6.50 < p_T^{J/\psi} < 8.00$ GeV/c (bottom), and the rapidity region is $1.6 < |y^{J/\psi}| < 2.4$.

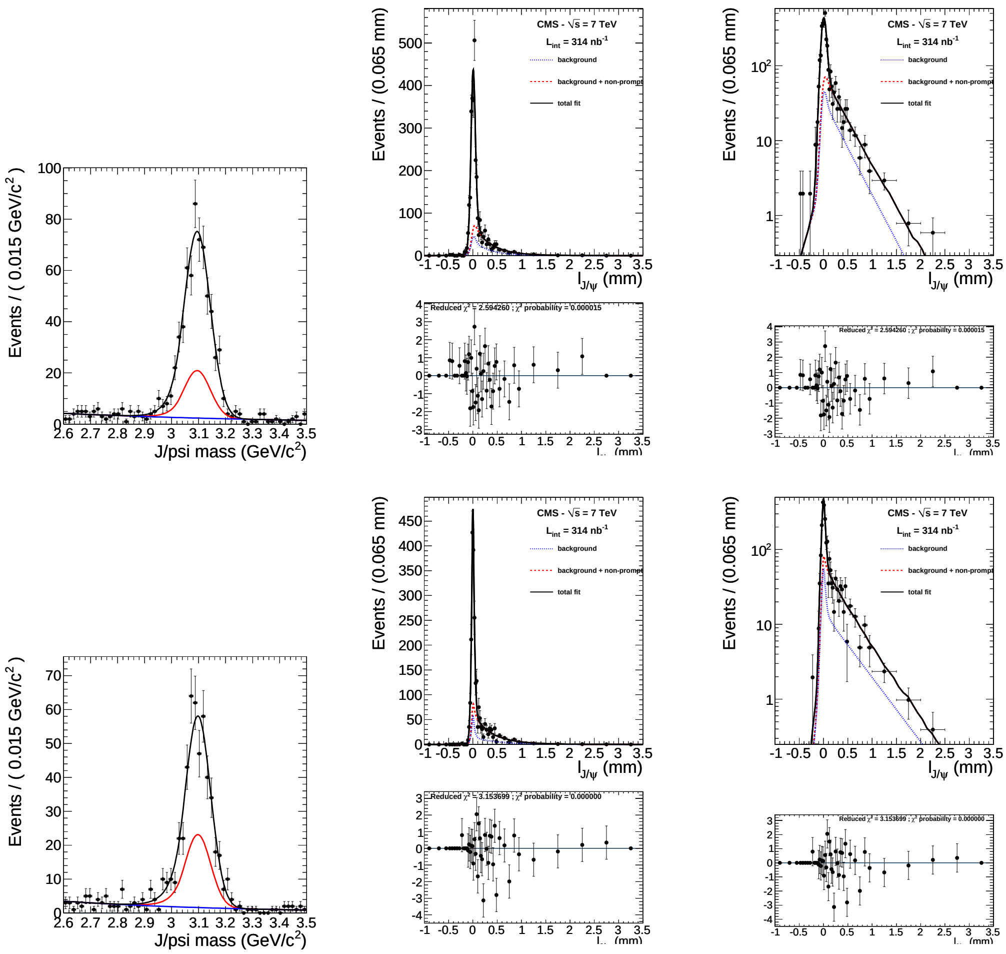

Figure 8.21: J/ψ mass-lifetime 2D fitted in $8.00 < p_T^{J/\psi} < 10.00$ GeV/c (upper) and $10.00 < p_T^{J/\psi} < 30.00$ GeV/c (bottom), and the rapidity region is $1.6 < |y^{J/\psi}| < 2.4$.

Table 8.3: The B-fraction in each bin from Ref. [61], approved by CMS collaboration. The B-fraction column shows the statistical and systematic errors.

$p_T^{J/\psi}(GeV/c)$	B-fraction	$p_T^{J/\psi}(GeV/c)$	B-fraction
$\lvert y^{J/\psi}\rvert < 1.2$		$1.6 < \lvert y^{J/\psi}\rvert < 2.4$	
4.5-6.5	$18.1 \pm 2.4 \pm 1.5\%$	0.00-1.25	$5.7 \pm 2.1 \pm 4.2\%$
6.5-10.0	$26.1 \pm 1.5 \pm 1.4\%$	1.25-2.00	$8.7 \pm 1.4 \pm 2.2\%$
10.0-30.0	$40.5 \pm 1.8 \pm 0.5\%$	2.00-2.75	$11.3 \pm 1.3 \pm 2.0\%$
$1.2 < \lvert y^{J/\psi}\rvert < 1.6$		2.75-3.50	$13.8 \pm 1.4 \pm 0.9\%$
2.0-4.5	$14.7 \pm 2.1 \pm 2.8\%$	3.50-4.50	$16.0 \pm 1.4 \pm 1.3\%$
4.5-6.5	$17.8 \pm 1.7 \pm 1.9\%$	4.50-6.50	$17.3 \pm 1.2 \pm 1.2\%$
6.5-10.0	$20.4 \pm 1.7 \pm 0.4\%$	6.50-10.00	$23.3 \pm 1.6 \pm 1.2\%$
10.0-30.0	$36.3 \pm 3.1 \pm 1.6\%$	10.00-30.00	$37.7 \pm 3.1 \pm 0.8\%$

E J/ψ cross section parameters

Each factor in J/ψ cross section measurement is listed in Table. 8.4.

Table 8.4: The J/ψ cross section parameters and the final inclusive cross section in each bin.

$p_T^{J/\psi}(GeV/c)$	Yield	$< 1/(A\epsilon) >^{-1}$	$\frac{d^2\sigma}{dp_T dy}[nb/(GeV \cdot c^{-1})]$
	$\|y^{J/\psi}\| < 1.2$		
4.5-5.5	299 ± 19	0.027 ± 0.003	14.7 ± 2.11
5.5-6.5	347 ± 20	0.048 ± 0.003	9.56 ± 1.38
6.5-8.0	725 ± 28	0.084 ± 0.004	7.63 ± 0.57
8.0-10.0	890 ± 87	0.178 ± 0.005	3.23 ± 0.19
10.0-12.0	513 ± 23	0.288 ± 0.008	1.186 ± 0.077
12.0-30.0	635 ± 26	0.405 ± 0.008	0.1157 ± 0.0062
	$1.2 < \|y^{J/\psi}\| < 1.6$		
2.0-3.5	398 ± 26	0.016 ± 0.002	68.8 ± 12.9
3.5-4.5	417 ± 33	0.035 ± 0.004	46.1 ± 4.87
4.5-5.5	615 ± 28	0.086 ± 0.004	28.6 ± 2.61
5.5-6.5	691 ± 34	0.167 ± 0.005	16.5 ± 1.10
6.5-8.0	711 ± 28	0.247 ± 0.006	7.64 ± 0.38
8.0-10.0	463 ± 23	0.334 ± 0.009	2.76 ± 0.17
10.0-30.0	406 ± 22	0.445 ± 0.013	0.181 ± 0.012

Table 8.5: Refer to Table 8.4, continued.

$p_T^{J/\psi}(GeV/c)$	Yield	$< 1/(A\epsilon) >^{-1}$	$\frac{d^2\sigma}{dp_T dy}[nb/(GeV \cdot c^{-1})]$
	$1.2 < \lvert y^{J/\psi} \rvert < 1.6$		
0.00-0.50	672 ± 44	0.075 ± 0.006	36.8 ± 4.9
0.50-0.75	744 ± 43	0.079 ± 0.007	83.2 ± 13.0
0.75-1.00	951 ± 48	0.078 ± 0.007	102.2 ± 13.6
1.00-1.25	1182 ± 46	0.079 ± 0.007	121.9 ± 17.1
1.25-1.50	1174 ± 59	0.077 ± 0.006	127.6 ± 17.2
1.50-1.75	1264 ± 62	0.075 ± 0.007	132.5 ± 17.1
1.75-2.00	1075 ± 46	0.074 ± 0.007	121.9 ± 13.3
2.00-2.25	1131 ± 133	0.071 ± 0.009	125.1 ± 14.0
2.25-2.50	892 ± 40	0.074 ± 0.008	96.3 ± 10.1
2.50-2.75	904 ± 68	0.075 ± 0.007	96.4 ± 10.7
2.75-3.00	756 ± 36	0.077 ± 0.007	77.9 ± 7.47
3.00-3.25	755 ± 34	0.082 ± 0.009	73.7 ± 6.86
3.25-3.50	702 ± 32	0.084 ± 0.007	66.7 ± 5.84
3.50-4.00	1152 ± 53	0.092 ± 0.007	49.6 ± 4.80
4.00-4.50	980 ± 36	0.100 ± 0.007	39.7 ± 2.91
4.50-5.50	1420 ± 43	0.117 ± 0.007	24.5 ± 2.02
5.50-6.50	991 ± 35	0.157 ± 0.010	12.6 ± 1.00
6.50-8.00	914 ± 47	0.193 ± 0.009	6.195 ± 0.382
8.00-10.00	603 ± 27	0.250 ± 0.012	2.41 ± 0.148
10.00-30.00	474 ± 31	0.309 ± 0.015	0.149 ± 0.013

Reference

[1] E598 Collaboration, "Experimental. Observation of a Heavy Particle J", Phys. Rev. Lett. 33 (1974)1404.

[2] SLAC-SP-017 Collaboration, "Discovery of Narrow Resonance in e+e- Annihilation", Phys. Rev. Lett. 33 (1974) 1406.

[3] C. Bacci, *et al.*, "Preliminary Result of Frascati (ADONE) on the Nature of a New 3.1-GeV Particle Produced in e^+e^- Annihilation", Phys. Rev. Lett. 33(1974)1408.

[4] G. S. Abrams, *et al.*, "Discovery of a Second Narrow Resonance in e^+e^- Annihilation", Phys. Rev. Lett. 33 (1974)1453.

[5] E598 Collaboration, "ENonobservation of Heavier J Particles from p-N Reactions", Phys. Rev. Lett. 33 (1974)1624.

[6] M. L. Perl, *et al.*, "Evidence for Anomalous Lepton Production in e^+e^- Annihilation", Phys. Rev. Lett. 35 (1975)1489.

[7] Particle Data Group, "Review of Particle Phyiscs", chapter IX, P.114, 2010.

[8] G. Dissertori and G. P. Salam, "Quantum Chromodynamic and its coupling", PDF book, chapter IX, October 2009.

[9] K. Ellis, "Quantum Chromodynamic", Fermilab internal lecture material, February 2005.

[10] J. P. Lansberg, "J/ψ, $\psi(2S)$ and Υ production at hadron colliders: a review", arXiv:hep-ph/0602091v2, 20 August 2006.

[11] E. L. Berger, *et al*, "Inelastic photoproduction of J/ψ and Υ by gluons", Phys. Rev. D. 23 (1981)1521, 1981.

[12] P. Artoisenet, *et al*, "J/ψ production in association with a charm-quark pair at the Tevatron", arXiv:0804.2975v1[hep-ph], 18 April 2008.

[13] P. Artoisenet, *et al*, "Υ production at the Tevatron and the LHC", arXiv:0806.3282v2[hep-ph], 22 June 2008.

[14] E. Braaten and S. Fleming, "Color-Octet Fragmentation and the $\psi(2S)$ Surplus at the Tevatron", Phys. Rev. Lett. 74 (1995)3327, 1995.

[15] M. Beneke and M. Kraemer, "Direct J/ψ and ψ' polarization and cross sections at the Fermilab Tevatron", Phys. Rev. D. 55 (1997)5269, 1997.

[16] P. Faccioli, *et al.*, "J/ψ polarization from fixed-target to collider energies", Phys. Rev. Lett. 17;102(15):151802. 16 April 2009.

[17] http://ben.web.cern.ch/ben/TCPHIST.html

[18] http://bigscience.web.cern.ch/bigscience/en/lhc/

[19] L. Evans and P. Bryant, "The CERN Large Hadron Collider: Accelerator and Experiments. The LHC machine", Journal of Instrumentation 3,08,S08001 (2008).

[20] https://twiki.cern.ch/twiki/bin/view/CMS/LumiWikiHome

[21] https://twiki.cern.ch/twiki/bin/view/CMSPublic/LumiPublicResults2010

[22] N. Adam, *et al.*, "The CMS Luminosity System", CMS Internal Note, CMS IN-2007/030, 31 May 2007.

[23] CERN Yellow Report, "CERN Workshop on Standard Model Physics (and more) at the LHC", 2000-004.

[24] D. Denegri, "Standard Model Physics at the LHC (pp Collisions)", CERN-PPE/90.181, 3 December 1990.

[25] M. Spira and P. M. Zerwas, "Electroweak symmetry breaking and Higgs physics", CERN-TH/97-379 (1997), hep-ph/9803257.

[26] U. Egede, "Higgs physics at the LHC", Aguest 1998.

[27] http://cms.web.cern.ch/cms/Detector/index.html.

[28] CMS Collaboration, "The Tracker Project Technical Design Report", CERN/LHCC 98-6, 15 April 1998. (Last updated on 01 Decemeber 1999.)

[29] CMS Collaboration, "Addendum to the CMSTracker TDR", CERN/LHCC 2000-016, CMS TDR 5 Addendum 1, 21 February 2000.

[30] D. Abbaneo, "Layout and performance of the CMS Silicon Strip Tracker", Nuclear Instruments and Methods in Physics Research A 518 (2004) 331.

[31] M. Weber, "Alignment strategy for the CMS Tracker", Journal of Physics: Conference Series 120 (2008) 022034.

[32] Y. Musienko, "The CMS electromagnetic calorimeter", Nuclear Instruments and Methods in Physics Research A 494 (2002) 308

[33] CMS Collaboration, "CMS ECAL Techinical Design Report", CMS/LHCC 97-33, 15 December 1997.

[34] CMS Collaboration, "CMS HCAL Techinical Design Report", CMS/LHCC 97-31, 20 June 1997.

[35] CMS Collabration, "The Magnet Project Technical Design Report", CERN/LHCC 97-010, 1997.

[36] CMS Collabration, "The Compact Muon Solenoid Technical Proposal", CERN/LHCC 94-38, 1994.

[37] CMS Collabration, "The Muon Project Technical Design Report", CERN/LHCC 97-32, 1997.

[38] CMS Collabration, "CMS Physics Technical Design Report", Volume I, Detector Performance and Software, CERN/LHCC 2006-001, 2 Februarry 2006.

[39] B. Roland, "Forward Physics Capabilities of CMS with the CASTOR and ZDC detectors", arXiv:1008.0592, 3 August 2010.

[40] O. A. Grachov, *et al.*, CMS Collabration, "Status of Zero Degree Calorimeter for CMS Experiment", CERN PH/EP, CH-1211.

[41] E. Norbeck, *et al.*, "Physics at Very Small Angles with CASTOR at CMS", 22nd Winter Workshop on Nuclear Dynamics, 11 March 2006.

[42] CMS Collabration, "CMS TriDAS Project Technical Design Report, Volume 1: The Trigger Systems", CERN/LHCC 2000-38, CMS TDR 6.1, 15 December 2000.

[43] CMS Computing Project group, "CMS Computing Project Technical Design Report", CERN/LHCC-2005-023, CMS TDR 7, 20 June 2005.

[44] https://twiki.cern.ch/twiki/bin/viewauth/CMS/WorkBookComputingModel.

[45] https://twiki.cern.ch/twiki/bin/view/CMS/WorkBookCMSSWFramework.

[46] B. Povh, *et al.*, "Particles and Nuclei", ISNB:978-3-540-79367-0.

[47] S. Eidelman, *et al*, "Particle Data Group Collaboration", Phys. Lett. B 592 (2004) 1.

[48] Y. Q. Ma, K. Wang and K. T. Chao, "A complete NLO calculation of the J/ψ production at Tevatron and LHC", arXiv:1012.1030v1, 5 December 2010.

[49] J. F. Amundson, *et al*, “Quantitative Tests of Color Evaporation: Charmonium Production”, arXiv:hep-ph/9605295v1, 13 May 1996.

[50] M. Kraemer, “Quarkonium Production at High-Energy Colliders”, Prog. Part. Nucl. Phys. 47, arXiv:hep-ph/0106120v1, 12 June 2001.

[51] Y. Q. Ma, *et al*, “$J/\psi(\psi(2S))$ production at the Tevatron and LHC at $\mathcal{O}(\alpha_s^4 v^4)$ in nonrelativistic QCD”, arXiv:1009.3655v2[hep-ph], 27 January 2011.

[52] CMS Collabration, “Stand-alone Cosmic Muon Reconstruction Before Installation of the CMS Silicon Strip Tracker”, CMS Note, 12 Feb 2009.

[53] N. Neumeister, “Muon Reconstruction Software in CMS”, CMS internal material, unknown time.

[54] P. Bartalini, *et al.*, “Guidelines for the estimation of theorerical uncertainties at the LHC”, CMS Note 2005/013, 23 September 2005.

[55] Z. YANG, *et al.*, “Feasibility study of a J/ψ cross section measurement with early CMS data”, CMS AN-2007/023, 28 July 2008.

[56] N. Adm, *et al.*, “$\Upsilon(1S)$ Efficiency Measurement With Early Data”, CMS AN-2009/064, 27 April 2009.

[57] M. E. Reinhard, “Determination of Muon Reconstruction and Identification Efficiencies in the CMS Experiment”, ETHZ-IPP Internal Report 2008-12, August 2008.

[58] CMS Collabration, “Performance of muon identification in pp collisions at $\sqrt{s} = 7TeV$”, CMS PAS MUO-10-002(2010).

[59] CMS Collabration, “Measurement of Momentum Scale and Resolution using Low-mass Resonance and Cosmic Ray Muons”, CMS Physics Analysis Summary, CMS-PAS-TRK-10-004(2010).

[60] BaBar Collaboration, "Study of inclusive production of charmonium mesons in B decay", Phys. Rev. D. 67 (2003) 032002. doi:10.1103/Phys. Rev. D. 67.032002.

[61] CMS Collaboration, "Prompt and non-prompt J/ψ production in pp collisions at $\sqrt{s} = 7TeV$", CMS PAPER BPH-10-002, 29 November 2010.

[62] F. Palla and S. GUO, *et al.*, "Inclusive total and differential production cross section of J/ψ and b-hadron production in pp collisions at $\sqrt{s} = 7TeV$ with the CMS experiment", CMS AN-10-138, 08 November 2010.

[63] Pythia Group, "PYTHIA 6.4 Physics and Manual", JHEP (2006) 05 026.

[64] H. Jung, "The CCFM Monte Carlo generator CASCADE" Comp. Phys. Commun, 143 (2002) 100.

[65] M. Cacciari, *et al.*, "CASCADE workbook", JHEP 0407 (2004) 033.

List of Figures

List of Tables

List of Publications and Presentations

Publications:

1. CMS Collaboration, *Prompt and non-prompt J/ψ production in pp collisions at* $\sqrt{s} = 7TeV$,European Physical Journal C , CMS PAPER BPH-10-002, 29 November 2010.

2. Shuang GUO, Zhen HU, Zongchang YANG, Sijin QIAN and Lie LIU, *Feasibility study on cross section measurement of $\Upsilon(1S) \rightarrow \mu^+\mu^-$ by using early CMS data*, Chinese Physics C, 34(8), 2010.

3. Shuang GUO on behalf of CMS Collaboration, *Measurement of the inclusive b production cross section in pp collisions at* $\sqrt{s} = 7TeV$, proceeding of HQL2010 conference, 2010.

4. Zhen Hu and Shuang GUO, *et al.*, *Feasibility Study for Measuring J/ψ Polarization Using Early LHC Data at* $\sqrt{s} = 10TeV$, Acta Scientiarum Naturalium Universitatis Pekinensis, (in Chinese, accepted and to be published in 2011).

5. Lie LIU, Shuang GUO, Zongchang YANG and Sijin QIAN, *Study Bottomium Production and Polarization in CMS*, Acta Scientiarum Naturalium Universitatis Pekinensis, Vol.45, No.3, 2009. (in Chinese)

CMS Internal Notes:

1. F. Palla, S. GUO, *et al.*, CMS AN-2010/138, (2010).

2. S. GUO, CMS-CR-2010-283, CERN-CMS-CR-2010-283, (2010).

3. S. GUO *et al.* CMS AN-2009/066, (2009).

4. Z. HU and S. GUO, *et al.* CMS AN-2009/091, (2009).

Presentations in International Conferences:

1. *Measurement of the inclusive b production cross section in pp collisions at* $\sqrt{s} = 7TeV$, The Xth Nicola Cabibbo International Conference on Heavy Quarks and Leptons, Frascati (Rome), Italy (11-15 October 2010).

北京大学

博士研究生学位论文

题目： CMS实验上重味夸克偶素产生截面的测量

姓　　名：郭爽

学　　号：10604824

院　　系：物理学院

专　　业：粒子物理与原子核物理

研究方向：高能物理实验

导师姓名：钱思进 教授

二零一一年五月

版权声明